

WOUND HEALING ON ARTIFICIAL EXTRACELLULAR
MATRIX PROTEINS

Thesis by

Eileen Fong

In Partial Fulfillment of the Requirements

For the Degree of

Doctor of Philosophy



California Institute of Technology

Pasadena, California

2010

(Defended June 2, 2010)

© 2010

Eileen Fong

All Rights Reserved.

To my family and friends

Acknowledgements

I would like to express my greatest gratitude to my advisor, David A. Tirrell, without whom this thesis would not have been possible. Dave is one of the most brilliant scientists I have ever met, and I am honored to have worked with him. Dave constantly amazes me with his quick-wit and foresight; yet he is exceptionally humble. Dave has inspired me tremendously with his passion for science, and has made graduate school memorable (really!). He has not only taught me to be a better scientist, but also how to be a better person. I am grateful for all the guidance and support he has provided me throughout my years at Caltech. I truly enjoyed my interactions with him, and will treasure our many conversations about science and life. I will continue to hold him as my role model as, and to inspire my students the way he has inspired me. Most importantly, I am going to miss his humor.

I also had the pleasure to collaborate with Prof. Guo Chin-lin, an outstanding scientist, teacher, and friend. I am inspired by his intelligence and creativity, and have enjoyed collaborating with him and members of his lab. I enjoyed the many discussions we have had about science and life. I am grateful for his guidance and friendship, without which the last two chapters of my thesis would not have been possible.

My committee members have provided valuable advice and have helped me to become a better scientist. I would also like to thank my committee members: Prof. Marianne Bronner-Fraser has been extremely kind and she has not only introduced me to Developmental Biology, but single-handedly ignited my interest in the field of wound healing. Prof. Anand Asthagiri has taught me to connect between math and biology in his

class, as well as provided valuable critique on my research. And to Prof. Mark E. Davis who was an exemplary role model for young scientists like myself.

My graduate life has been made memorable (and fun!) by many friends and colleagues at Caltech. In particular, I thank Beverly Lu and Shelly Tzlil for their life-long friendship and contributing to fond memories of my 5 years at Caltech. I also like to thank Stacey Maskarinec, who selflessly taught me everything she knew about cloning and expressing the aECM proteins. I would also like to thank all past and present members of the Tirrell laboratory, who have contributed in one way or another to making my stay here at Caltech memorable. I would also like to thank members of the Guo and Asthagiri lab for the friendship and generous support they have given me throughout the years.

I would also like to thank my family for their love and sacrifices they have made for me to pursue my dream. I am grateful for their patience and constant support, for being with me all these years. I would also like to thank Benny Poon for the years of laughter and being part of my memories at Caltech.

Lastly, I would like to acknowledge the Nanyang Technological University, Singapore (NTU) for their generous funding for 4 years at Caltech. I am also grateful to many mentors at NTU, who have provided me with valuable advice and support in my academic career at NTU.

WOUND HEALING ON ARTIFICIAL EXTRACELLULAR MATRIX PROTEINS

June 2010

Eileen Fong, B. Mat. E., Nanyang Technological University, Singapore

Ph.D., California Institute of Technology

Supervised by David A. Tirrell

Abstract

Collective cell migration is a key process in tissue repair, and in drawing parallels from complex multi-cellular events such as tumor morphogenesis and embryogenesis. Mechanisms of wound healing have been studied extensively *in vitro*. Extracellular matrix (ECM) is required to support cell migration and ensure rapid coverage of the wound area. The main challenge in designing biomaterials for tissue repair is to provide cells with the appropriate biological and mechanical cues. Hence, understanding key cell-ECM interactions during wound healing is necessary for effective biomaterial design.

Genetic engineering provides a convenient avenue to customize materials for any given application. The artificial protein-based biomaterials discussed in this work were derived from fibronectin and elastin. These proteins have a modular design, and have

material properties that can be fine-tuned according to specific applications. The artificial extracellular matrix (aECM) proteins prepared by previous members of our laboratory have been shown to promote attachment of endothelial cells. In this work, we studied extensively epithelial and fibroblast wound healing behavior on these aECM biomaterials.

Crosslinked aECM protein films of varying RGD densities have been prepared by mixing aECM proteins with the RGD cell binding domain with aECM proteins containing the scrambled RDG sequence. Corneal epithelial wound healing was observed on aECM films with 100% RGD but not on aECM films with 2.5% RGD. Surprisingly, we found a five fold difference between the wound closure rates between these surfaces, but individual cell speeds did not increase significantly. We proposed that the five fold increase in wound closure rate was determined by the rate of crossing the boundary between the wound area and the area underneath the cell sheet. Both simulation and experimental data verified that the rate of boundary-crossing was sufficient to account for five-fold difference in wound closure rates between 100% RGD and 2.5% RGD surfaces.

Full-length fibronectin domains have also been incorporated to improve the overall cell binding properties of the aECM proteins. The aECM proteins containing full-length fibronectin domains were shown to facilitate rapid spreading of Rat-1 fibroblasts. The aECM protein containing both fibronectin domains 9 and 10 exhibited an increased binding affinity to the $\alpha_5\beta_1$ integrin. More importantly, these aECM proteins also promoted rapid wound closure, which was comparable to that on fibronectin. We showed that aECM proteins containing full-length fibronectin domains also promoted higher

phosphorylated levels of focal adhesion kinase (FAK) and extracellular signal-regulated kinase (ERK), consistent with the faster cell migration and proliferation observed.

To try to understand how cells select wound healing mechanisms, wound healing of Madin-Darby Canine Kidney (MDCK) epithelial cells were examined *in vitro*. On surfaces containing the aECM protein bearing the fibronectin domain 10, characteristic healing patterns were observed in MDCK wound healing. These patterns are defined by the formation of leader cells at regular intervals of actomyosin purse strings. The spacing between consecutive leader cell groups was also found to be independent of the wound diameter. This spacing however, was found to decrease with increasing myosin II inhibition. These observations could be explained using a simple force transmission mechanical model. Consistent with the model predictions, we demonstrated that wounds with a zigzag geometry biased the selection of the wound healing mechanism along the wound edge. These zigzag wounds also healed nearly eight fold faster than wounds with straight edges.

Table of Contents

| | |
|--|-----|
| Abstract | vi |
| List of Figures and Tables | xii |
| 1 Introduction | |
| 1.1 Wound healing | 1 |
| 1.2 Challenges in tissue regeneration | 2 |
| 1.3 Artificial proteins as biomaterials | 3 |
| 1.4 Methods for studying wound healing <i>in vitro</i> | 5 |
| 1.5 Thesis organization and description of contributions | 6 |
| 1.6 References | 9 |
| 2 The role of boundary-crossing in epithelial wound healing | |
| Abstract | 12 |
| 2.1 Introduction | 13 |
| 2.2 Materials and methods | 14 |
| 2.3 Results and discussion | 22 |
| 2.4 Conclusions | 33 |
| 2.5 Acknowledgements | 34 |
| 2.6 References | 34 |
| Additional information for Chapter 2 | 36 |

| | | |
|----------|---|-----|
| 3 | Artificial extracellular matrix proteins for rapid wound healing | |
| | Abstract | 54 |
| 3.1 | Introduction | 55 |
| 3.2 | Materials and methods | 57 |
| 3.3 | Results and discussion | 64 |
| 3.4 | Conclusions | 76 |
| 3.5 | Acknowledgements | 76 |
| 3.6 | References | 76 |
| | | |
| 4 | Early patterns in wound healing | |
| | Abstract | 79 |
| 4.1 | Introduction | 80 |
| 4.2 | Materials and methods | 81 |
| 4.3 | Results and discussion | 87 |
| 4.4 | Conclusions | 95 |
| 4.5 | Acknowledgements | 95 |
| 4.6 | References | 95 |
| | Additional information for Chapter 4 | 97 |
| | | |
| 5 | Harnessing the purse string for accelerated wound healing | |
| | Abstract | 107 |
| 5.1 | Introduction | 108 |
| 5.2 | Materials and methods | 110 |

| | | |
|----------|--|------------|
| 5.3 | Results and discussion | 112 |
| 5.4 | Conclusions | 118 |
| 5.5 | Acknowledgements | 119 |
| 5.6 | References | 119 |
| 6 | Conclusions and future work | 120 |

DNA plasmid maps

List of Figures and Tables

1 Introduction

| | | |
|-----|--|---|
| 1.1 | Amino acid sequence of aECM proteins | 4 |
|-----|--|---|

2 The Role of Boundary Crossing in Epithelial Wound Healing

| | | |
|-----|--|----|
| 2.1 | HCE cell spreading behavior on various substrates | 23 |
| 2.2 | (A) Schematic of wound healing experiment (B) Time course of wound healing on 2.5% RGD and 100% RGD substrates (C) Schematic of the Monte-Carlo simulation | 25 |
| 2.3 | Wound healing behavior observed in experiments and simulations | 28 |
| 2.4 | Image of typical substrate with an interface imaged by atomic force microscopy | 31 |
| 2.5 | Interface crossing and simulated and experimental rate constants of interface crossing | 32 |
| A1 | Amino acid sequences of aECM proteins containing (A) RGD and (B) RDG cell-binding domains | 36 |
| A2 | Rate constants of interface crossing, k_c from 100% RGD to various test surfaces | 37 |
| A3 | A schematic illustration of the cell spreading and retraction model | 38 |
| A4 | The fit of the experimental spreading data to the theoretical expression for the relative spreading rate, Equation 10 | 42 |
| A5 | An illustration of the proliferation kinetic scheme | 44 |

| | | |
|-----------------|--|-------|
| A6 | Schematic diagram of cell at an interface, showing two possible outcomes | 48 |
| A7 | The rate constants of interface crossing from FN to test surfaces obtained from simulation | 51 |
| <i>Table A1</i> | Summary of the rates for 100% and 2.5% RGD surfaces | 52 |
| 3 | Artificial Extracellular Matrix Proteins for Rapid Wound Healing | |
| 3.1 | Amino acid sequences of the aECM proteins containing full length fibronectin domains | 56 |
| 3.2 | Coomassie SDS-PAGE gel of purified aECM proteins | 65 |
| 3.3 | Time course of cell spreading of Rat-1 fibroblasts on adsorbed protein surfaces | 67 |
| 3.4 | Time course of cell spreading of Rat-1 fibroblasts on crosslinked protein surfaces | 68 |
| 3.5 | Binding of $\alpha_5\beta_1$ integrin to fibronectin and aECM proteins by ELISA | 70 |
| 3.6 | Quantification of wound healing behavior on adsorbed protein surfaces | 72 |
| 3.7 | Determination of FAK and ERK phosphorylation in Rat-1 fibroblasts on various surfaces | 74,75 |
| 4 | Early patterns in wound healing | |
| 4.1 | The amino acid sequence of aECM protein containing the fibronectin 10 domain | 81 |

| | | |
|------|--|-----|
| 4.2 | Design of micropatterned PDMS blocks for creating circular and zigzag-shaped wounds | 83 |
| 4.3 | Schematic of wound healing assay | 85 |
| 4.4 | Removal of PDMS preserved aECM protein surface underneath | 88 |
| 4.5 | Time-lapse images of MDCK wound healing behavior on both aECM and untreated glass substrates | 89 |
| 4.6 | Verification of leader cells and purse-string structures | 90 |
| 4.7 | Quantification of wound healing behavior for circular wounds of increasing diameters | 91 |
| 4.8 | Effect of myosin inhibition on leader cell formation | 92 |
| 4.9 | Schematic of proposed mechanical model | 93 |
| 4.10 | Wound curvature bias wound closure mechanisms | 94 |
| B1 | Model predictions | 103 |

5 Harnessing the purse string for accelerated wound healing

| | | |
|------------------|---|-----|
| 5.1 | Schematic of wound closure in zigzag wounds and the effect of angles on purse string contractions | 109 |
| 5.2 | Initial wound geometry determines mode of wound healing | 113 |
| 5.3 | Time course of wound healing for zigzag wounds | 115 |
| <i>Table 5.1</i> | Wound closure rates as a function of 2θ | 116 |
| 5.4 | Overall contractile speed of purse string as a function 2θ | 117 |

1 INTRODUCTION

1.1 Wound healing

The wound healing process has been studied for decades. It involves a series of intricate cellular events involving cell migration, proliferation, and remodeling (1-2). Upon the onset of the inflammatory response, fibroblasts begin to proliferate and migrate into the wound area. Collagen and fibronectin are subsequently deposited in the wound bed (3), serving as a temporary matrix on which epithelial cells can migrate (4-5). Throughout the process, cells often migrate as groups (6-7). The mechanisms by which they do so are under active investigation (8).

While understanding how cells move together in tissue repair is important, this process is also fundamentally relevant to other complex events such as morphogenesis and tumor metastasis (6, 9-10). Two mechanisms of collective migration have been identified (11). Lamellipodial crawling involves active migration of cells at the wound edge, mediated primarily through cell-ECM interactions in the wound area (12-14). This process is commonly observed in adult wound healing and is well-studied in *in vitro* wound healing models (15-17). The second mechanism is known as the “purse string” model, and is the primary mode of cell movement in fetal wound healing (18-20). Upon wounding, an actomyosin cable assembles around the periphery of the wound, and contracts to close the wound by transmitting tension through intercellular junctions (21). While the lamellipodial crawling mechanism results in rapid wound closure, the purse string mechanism leads to scarless wound healing (22). Understanding the factors

involved in both wound healing mechanisms might enable us to achieve optimal wound healing rates and to minimize scarring.

1.2 Challenges in tissue regeneration

The role of ECM in wound healing has been traditionally thought of as a passive structural support for cells. It is now clear that cell-ECM interactions, in concert with growth factors, are necessary for rapid wound healing (23-24). Hence, the main challenge in wound therapeutics is to provide an ideal microenvironment for optimal cell migration and proliferation (25).

Many strategies have been adopted for accelerating tissue repair. Exogenous growth factors (26-27), ECM molecules (28), and short peptide sequences (29) targeting specific integrin receptors have been shown to accelerate wound healing both *in vitro* and *in vivo*. However, native ECM molecules or growth factors lack structural properties, and are expensive to produce in large quantities. On the other hand, synthetic materials offer excellent physical support, but do not possess any biological activity. To circumvent these disadvantages, synthetic materials have also been functionalized with bioactive peptide sequences (30-32) and growth factors (33). However, issues arising from steric hindrance and denaturation of these molecules have yet to be resolved (34).

1.3 Artificial proteins as biomaterials

The advent of DNA recombinant technology has brought about the discovery of a novel class of protein-based biomaterials (35). Using a series of genetic manipulations, DNA sequences encoding functional moieties can be readily integrated into bacterial hosts and artificial proteins containing user-specified functionalities can be easily generated.

The genetic approach to biomaterial design allows the synthesis of complex protein macromolecules, which are otherwise difficult to fabricate by chemical means. Specific mechanical and biological functionalities can also be expressed combinatorially to direct cell behavior. Biological domains in fibronectin, laminin, and other ECM molecules have been widely incorporated into artificial proteins (35). The short Arg-Gly-Asp (RGD) sequence found in fibronectin has been shown to promote cell spreading of a multitude of cell types (36). Likewise, recombinant proteins derived from spider silk (37), collagen (38), and elastin (39) have been shown to display mechanical properties resembling their native proteins. In particular, Urry and coworkers have synthesized and characterized a series of recombinant elastin-like materials bearing repetitive motifs Val-Pro-Gly-X-Gly (VPGXG), where X can be any amino acid. These materials can be designed to yield a range of viscoelastic properties, by substituting the appropriate amino acid in the position X (40).

The artificial proteins prepared in our laboratory consist of functional domains derived from fibronectin and elastin (41-44). The artificial extracellular matrix (aECM) proteins are modular in nature, allowing simple substitution of either the biological or the

structural domains. Non-canonical amino acids have also been incorporated to introduce alternative crosslinking chemistries (45) and to create novel materials with tunable moduli (46). Figure 1.1 shows the amino acid sequences of the aECM proteins discussed in this thesis. In all constructs **1** to **5**, lysine residues were interspersed within the elastin-like sequences, and subsequently crosslinked to form viscoelastic materials (41, 47). These aECM proteins also exhibit the characteristic inverse transition temperature of elastin (48), which allows simple and effective purification via thermal cycling (49).

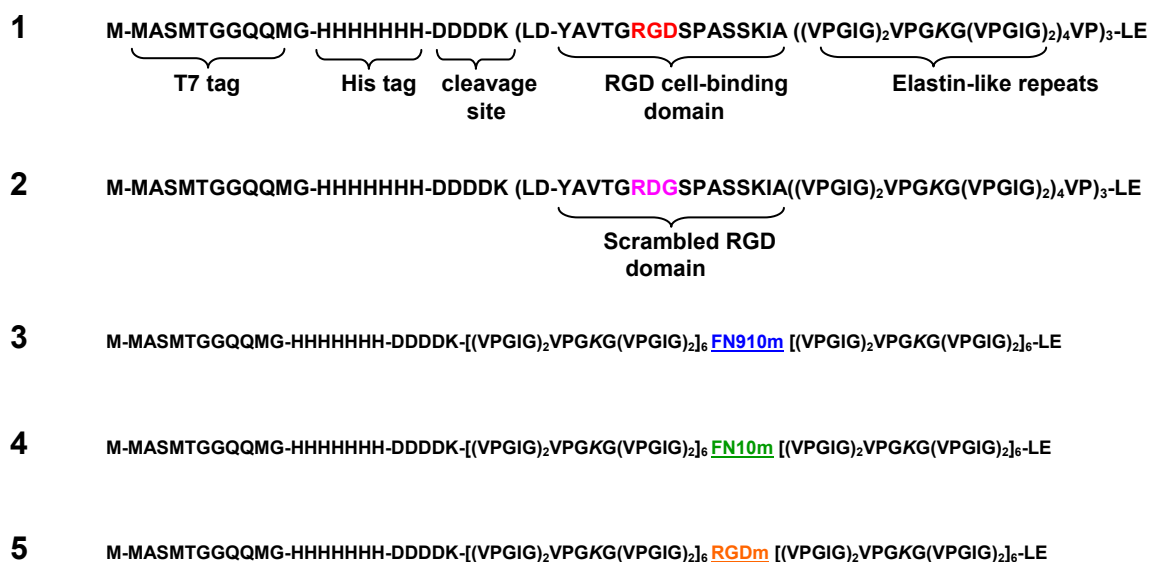


Figure 1.1 Amino acid sequences of aECM proteins. Each aECM protein contained a T7 tag, a hexahistidine tag, an enterokinase cleavage site, and elastin-like domains containing lysine residues (italicized) for crosslinking. Constructs **1** and **2** containing the short RGD sequence were developed by Julie Liu in our laboratory. Constructs **3** to **5** were designed and cloned in this work and will be discussed in greater detail in Chapter 3. The full amino acid sequences of the underlined cell binding domains in constructs **3** to **5** can be found in Figure 3.1.

In our work and that of others, cell responses on RGD surfaces were never identical to those observed on native fibronectin (50). An obvious strategy to improve biological activity of the existing aECM proteins is hence to expand the cell binding region to include full-length fibronectin domains. Efforts to expand on the biological activity of the aECM proteins are described in Chapter 3.

1.4 Methods for studying wound healing *in vitro*

In vitro wound healing assays have been used for decades to study the major signaling transduction pathways in wound healing (51-54). These assays have also been used to examine various mechanisms responsible for cell sheet movement (12-13, 15). The most commonly used setup is the “scratch” wound assay, which is performed by denuding an area of a confluent cell sheet using a small tool (e.g., pipette tip). The method is simple but often results in wounds that vary significantly between experiments. More importantly, the method is unsuitable for studying cell-material interactions. A major challenge in designing wound healing assays for studying cell-material interaction is to allow cells to form a confluent monolayer without modifying the underlying surface. A “barrier” wound healing assay not only allow precise control the surface chemistry of the wound area (54), it has also been shown to trigger wound responses similar to those observed in the scratch wound assays (16, 55). Recently, microfabrication has provided new tools for fabricating barriers (55), micropatterns (56), and microfluidic systems (57) for wound healing studies.

The *in vitro* “barrier” wound healing assay discussed in Chapter 2 was adapted from the work of Nikolić et al. (55). We used a polydimethylsiloxane (PDMS) block to protect the underlying aECM protein surface, while allowing cells to grow around it. Fibronectin was also added to allow cells to spread on surfaces that do not support cell attachment (i.e., BSA and aECM proteins containing a scrambled “RDG” sequence). When cells grow to confluence, the PDMS slab is removed, exposing the wounded cell sheet to the initial protein surface. The same assay was used again in Chapter 3 to compare different protein surfaces. The “barrier” assay provided a convenient way to examine cell-aECM interactions *in vitro*, but the wound areas were too large to allow the visualization of the entire wound periphery.

Attempts to study cell decisions along the periphery of the wound prompted further development of the wound healing assay. Using standard lithography methods, we prepared PDMS blocks bearing micron-sized barriers to replace the previous PDMS blocks. These patterns were made to create wounds of precise wound size and shape, allowing a systematic study of the role of wound geometry in wound healing.

1.5 Thesis organization and description of contributions

The thesis reports efforts towards understanding the fundamentals of cell-ECM interactions in wound healing. We studied extensively epithelial and fibroblast wound healing; both play distinct roles in the process of wound healing. The aECM proteins were used to understand and engineer specific cell-ECM interactions to accelerate wound

healing. More specifically, Chapter 2 examines corneal epithelial wound healing on crosslinked aECM protein with varying RGD densities. Crosslinked aECM films were produced by mixing aECM proteins with the RGD cell-binding domain and aECM proteins containing the RGD scrambled control (Figure 1.1; constructs **1** and **2**). I developed and performed the wound healing experiments, and analyzed the experimental data. The theoretical portion of this chapter was performed by Dr. Shelly Tzlil. Details of the simulation and data analysis were discussed jointly with Dr. Tzlil. I designed and performed all the experiments. We collaborated on writing the manuscript.

Another aspect of this work was focused on improving the design of the artificial extracellular matrix protein (aECM) materials to accelerate wound healing. In Chapter 3, I re-engineered the existing aECM protein constructs to incorporate full-length fibronectin domains 9 and 10 (Figure 1.1, constructs **3** to **5**). Rat-1 fibroblasts spread rapidly on these aECM protein surfaces. More importantly, aECM proteins containing full-length fibronectin domains 9 and 10 promoted rapid wound healing by supporting cell migration and proliferation, comparable to native fibronectin. I designed, cloned, and expressed these aECM proteins. I also performed all experiments and wrote the chapter.

Using the aECM protein containing fibronectin domain 10 (Figure 1.1; construct **4**) as described previously, we look to further understand how cells select the wound healing mechanism along the periphery of the wound. Chapters 4 and 5 resulted from collaborations with Dr. Chin-lin Guo. We used standard photolithography methods to create wound patterns with controlled wound size and geometry. I fabricated the master molds and made the PDMS micropatterned blocks. The MATLAB program used in

Chapter 4 was co-written by Jiang Bor-yuan and Dr. Guo. I acquired and analyzed all experimental data. I performed all other experiments. Dr. Guo wrote the description of the model while I wrote the experimental section. We co-wrote the rest of the chapter.

Chapter 5 describes how pre-disposing the cell sheets in a zigzag configuration allows cells to exploit the contraction of actomyosin cables and accelerate wound healing. I performed all the experiments and analyzed all the data with useful advice from Dr. Guo. I wrote the chapter.

1.6 References

1. A. J. Singer, R. A. F. Clark, *New Eng. J Med.* **341**, 738 (1999).
2. C. Steele, *Optometry Today*, 28 (1999).
3. F. Grinnell, *J. Cell Biochem.* **26**, 107 (1984).
4. R. A. F. Clark et al., *J. Invest. Dermatol.* **79**, 264 (1982).
5. R. A. F. Clark et al., *J. Invest. Dermatol.* **94**, 128S (1990).
6. P. Friedl, Y. Hegerfeldt, M. Tusch, *Int. J. Dev. Biol.* **48**, 441 (2004).
7. P. Rorth, *Trends in Cell Biol.* **17**, 575 (2007).
8. R. B. Vaughan, J. P. Trinkaus, *J. Cell Sci.* **1**, 407 (1966).
9. P. Martin, S. M. Parkhurst, *Development* **131**, 3021 (2004).
10. M. J. Redd, L. Cooper, W. Wood, B. Stramer, P. Martin, *Phil. Trans. R. Soc. Lond. B.* **359**, 777 (2004).
11. P. Martin, J. Lewis, *Science* **360**, 179 (1992).
12. R. Farooqui, G. Fenteany, *J. Cell. Sci.* **118**, 51 (2004).
13. X. Trepast et al., *Nat. Phys. Lett.* **5**, 426 (2009).
14. M. Zhao, B. Song, J. Pu, J. V. Forrester, C. D. McCaig, *FASEB J.* **17**, 397 (2003).
15. M. Bindschadler, J. L. McGrath, *J. Cell Sci.* **120**, 876 (2006).
16. E. R. Block et al., *J. Biol. Chem.* **279**, 24307 (2004).
17. K. Y. Chan, D. L. Patton, Y. T. Cosgrove, *Invest. Ophthalmol. Vis. Sci.* **30**, 2488 (1989).
18. W. M. Bement, P. Forscher, M. S. Mooseker, *J. Cell. Biol.* **121**, 565 (1993).
19. K. M. Bullard, M. T. Longaker, H. P. Lorenz, *World J. Surg.* **27**, 54 (2003).
20. Y. Danjo, I. K. Gipson, *J. Cell Sci.* **111**, 3323 (1998).
21. M. Tamada, T. D. Perez, W. J. Nelson, M. P. Sheetz, *J. Cell. Biol.* **176**, 27 (2007).
22. D. P. Kiehart, *Curr. Biol.* **9**, R602 (1999).

23. K. Watanabe, S. Nakagawa, T. Nishida, *Invest. Ophthalmol. Vis. Sci.* **28**, 205 (1987).
24. H. Brotchie, D. Wakefield, *Australas J. Dermatol.* **31**, 47 (1990).
25. R. Langer, D. A. Tirrell, *Nature* **428**, 487 (2004).
26. K. Hori et al., *J. Control. Res.* **118**, 169 (2007).
27. J. A. Hubbell, *J. Control. Res.* **39**, 305 (1996).
28. G. Maheshwari, A. Wells, L. G. Griffith, D. A. Lauffenburger, *Biophys. J* **76**, 2814 (1999).
29. D. L. Livant et al., *J. Clin. Invest.* **105**, 1537 (2000).
30. L. Aucoin, C. M. Griffith, G. Pleizier, Y. Deslandes, H. Sheardown, *J. Biomater. Sci. Polymer Edn.* **13**, 447 (2002).
31. A. Mardilovich, E. Kokkoli, *Biomacromolecules* **5**, 950 (2004).
32. U. Hersel, C. Dahman, H. Kessler, *Biomaterials* **24**, 4385 (2003).
33. J. A. Hubbell, *Swiss Med. Wkly* **136**, 387 (2006).
34. J. A. Neff, P. A. Tresco, K. D. Caldwell, *Biomaterials* **20**, 2377 (1999).
35. M. P. Lutolf, J. A. Hubbell, *Nat. Biotechnol.* **23**, 47 (2005).
36. M. D. Pierschbacher, E. Ruoslahti, *Nature* **309**, 30 (1984).
37. G. H. Altman et al., *Biomaterials* **24**, 401 (2003).
38. H. Kurihara, T. Morita, M. Shinkai, T. Nagamune, *Biotechnol. Lett.* **27**, 665 (2005).
39. S. Zhang, *Nat. Biotechnol.* **21**, 1171 (2003).
40. D. W. Urry, *J. Phys. Chem. B* **101**, 11007 (1997).
41. K. Di Zio, D. A. Tirrell, *Macromolecules* **36**, 1553 (2003).
42. S. C. Heilshorn, K. A. Di Zio, E. R. Welsh, D. A. Tirrell, *Biomaterials* **24**, 4245 (2003).
43. J. C. Liu, S. C. Heilshorn, D. A. Tirrell, *Biomacromolecules* **5**, 497 (2003).
44. J. C. Liu, D. A. Tirrell, *Biomacromolecules* **9**, 2984 (2008).

45. I. S. Carrico et al., *J. Am. Chem. Soc.* **129**, 4874 (2007).
46. P. J. Nowatzki, C. Franck, S. A. Maskarinec, G. Ravichandran, D. A. Tirrell, *Macromolecules* **41**, 1839 (2008).
47. P. J. Nowatzki, D. A. Tirrell, *Biomaterials*, 1261 (2003).
48. D. W. Urry, *Angewandte Chemie-International Edition in English* **32**, 819 (1993).
49. A. Panitch, T. Yamaoka, M. J. Fournier, T. L. Mason, D. A. Tirrell, *Macromolecules* **32**, 1701 (1999).
50. H. B. Streeter, D. A. Rees, *J Cell Biol* **105**, 507 (1987).
51. G. Fenteany, P. J. T. Stossel *Curr. Biol.* **10**, 831 (2000).
52. Y. Matsubayashi et al., *Curr. Biol.* **14**, 731 (2004).
53. P. J. Sammak, L. E. Hinman, P. O. T. Tran, M. D. Sjaastad, T. E. Machen, *J. Cell Sci.* **110**, 465 (1997).
54. R. van Horssen, N. Galjart, J. A. P. Rens, A. M. M. Eggermont, T. L. M. ten Hagen, *J. Cell. Biochem.* **99**, 1536 (2006).
55. D. L. Nikolić, A. N. Boettiger, D. Bar-Sagi, J. D. Carbeck, S. Y. Shvartsman, *Am J Physiol Cell Physiol* **291**, 68 (2006).
56. M. Poujade et al., *Proc. Natl. Am. Soc. USA* **104**, 15988 (2007).
57. A. D. van der Meer, K. Vermeul, A. A. Poot, J. Feijen, I. Vermes, *Am. J. Physio. Heart Circ. Physiol.* **298**, H719 (2010).

2 THE ROLE OF BOUNDARY-CROSSING IN EPITHELIAL WOUND HEALING

Abstract

The processes of wound healing and collective cell migration have been studied for decades. Intensive research has been devoted to understanding the mechanisms involved in wound healing, but the role of cell-substrate interactions is still not thoroughly understood. Here we probe the role of cell-substrate interactions by examining *in vitro* the healing of monolayers of human corneal epithelial (HCE) cells cultured on artificial extracellular matrix (aECM) proteins. We find that the rate of wound healing is dependent on the concentration of fibronectin-derived (RGD) cell-adhesion ligands in the aECM substrate. The wound closure rate varies nearly six fold on the substrates examined, despite the fact that the rate of migration of individual cells shows little sensitivity to the RGD concentration (which varies 40-fold). To explain this apparent contradiction, we study collective migration by means of a dynamic Monte-Carlo simulation. The cells in the simulation spread, retract, and proliferate with probabilities obtained from a simple phenomenological model. Results of the simulation reveal that the overall wound closure rate is determined by the probability of crossing the boundary between the matrix deposited underneath the cell sheet and the aECM protein.

Manuscript prepared for submission by Eileen Fong¹, Shelly Tzlil,² and David A. Tirrell^{1,2}

(1) Department of Bioengineering, California Institute of Technology

(2) Division of Chemistry and Chemical Engineering, California Institute of Technology

2.1 Introduction

The collective migration of cells is fundamental to wound healing, morphogenesis and many bioengineering applications. Wound healing in particular involves the migration of cell sheets over adhesive surfaces. Two mechanisms of migration have been identified in wound healing (1). First is the “purse string” mechanism where a marginal actomyosin cable develops along the wound edge, and wound closure proceeds with contraction of the actin belt (2). The second mechanism involves active spreading and migration of cells at the wound edge, known commonly as “lamellipodial crawling”. The latter mechanism is more commonly observed *in vitro* and has been characterized by using scratch-wound models. In these models, cells experience an injury, which triggers cell migration through various biochemical signaling events (3). It has also been argued that the availability of free space is sufficient to initiate cell migration in the absence of mechanical injury (4-6). Upon wounding, proliferation is up-regulated (7).

Adhesive cell-substratum interactions are required for sustained migration into the wound area (8, 9). The rates of migration of individual cells are governed by surface adhesivity in a biphasic fashion, at least under certain conditions (10). Surfaces modified with adhesion ligands such as fibronectin (FN) (11, 12) and Arg-Gly-Asp (RGD) peptides have been shown to facilitate wound healing, and it is reasonable to infer that the observed increases in healing rates arise primarily from faster migration of individual cells. We show here that other factors are more important.

The substrates used in this work were prepared from artificial extracellular matrix (aECM) proteins that combine domains derived from fibronectin and elastin (15) (Figure A1). We and others have shown that such aECM proteins can be crosslinked to yield materials with elastic moduli similar to those of natural elastins (13-15), and that presentation of the fibronectin-derived RGD sequence promotes cell spreading and adhesion (16-18).

Wound healing was examined in monolayers of human corneal epithelial cells (HCE) cultured on aECM protein substrates that present controlled, varying densities of the RGD sequence. HCE cells undergo rapid re-epithelization *in vivo* (19). Both the $\alpha_5\beta_1$ and $\alpha_v\beta_3$ integrins, which bind RGD, are up-regulated by wounding (20). Crosslinked films with varying RGD densities were prepared by mixing aECM proteins containing RGD and “scrambled” (RDG) domains. Substrates are identified by specifying the percentage of the RGD protein in the film (e.g., 100% RGD).

2.2 Materials and methods

Protein expression and purification

Standard methods for cloning, bacterial growth, protein expression, sodium dodecyl sulfate-polyacrylamide gel electrophoresis (SDS-PAGE), and Western blotting were used to prepare and characterize aE-RGD and aE-RDG (16). Typical yields of protein obtained from 10 L fermentation cultures were approximately 500 mg. The molar masses of aE-RGD and aE-RDG were 34.8 kDa.

Preparation of spin-coated aECM Films

Round glass coverslips (12 mm diameter; No. 1, Deckgläser, Germany) were sonicated in a mixture of ethanol and KOH for 15 min and rinsed several times with distilled H₂O. aECM protein solutions were prepared by dissolving mixtures of aE-RGD and aE-RDG (100 mg/ml in ddH₂O) for 3 – 4 h at 4 °C. Protein solutions containing 2.5%, 5%, 20%, 35%, 50%, 70%, 75%, 80%, 90%, and 100% aE-RGD were prepared. Bis[sulfosuccinimidyl] suberate (BS³) was used to crosslink the aECM protein substrates. BS³ (2.0 mg; Pierce, Rockford, IL) was dissolved in 17 µl of sterile distilled H₂O and added to 150 µl of protein solution, mixed, and centrifuged to remove bubbles. The stoichiometric ratio of activated esters in BS³ to primary amines in the aECM proteins was roughly 1:1. A 17 µl volume of BS³-protein solution was then spin-coated on a 12 mm diameter round glass cover slip at 7000 rpm for 30 sec at 4 °C. Each protein film was stored overnight at 4 °C before use.

Generation of aECM films containing boundaries

We prepared 100 µl of aECM protein solutions (25 mg/ml in distilled H₂O) containing 0%, 2.5%, 20%, 50%, and 100% aE-RGD and BS³ (0.29 mg in 2.5 µl ddH₂O) as previously described. The protein solution (17 µl) was spin-coated onto a 12 mm diameter round glass coverslip at 5000 rpm 30 sec at 4 °C. Protein films were allowed to dry overnight at 4 °C. Subsequently, 600 µl of aECM protein solution (15 mg/ml) was mixed with 1.725 mg of BS³ dissolved in 12.75 µl distilled H₂O. A small volume (2 µl) of the second aECM protein solution was pipetted across the middle of the film and spin-

coated at 5000 rpm for 30 sec at 4 °C. Under these conditions, an interface was generated between two distinct surface chemistries.

Characterization of substrates by atomic force microscopy (AFM)

Images and force curves were collected on an Asylum MFP-3D-BIO atomic force microscope, with accompanying IGOR Pro v.5.05 software. Pyramidal-tipped silicon nitride cantilevers (Veeco DNP-S) with nominal spring constant 0.58 N/m were used for imaging. The tip of a pair of fine forceps was drawn lightly across the surface of the protein film, prepared as described above, tearing away the protein along the scratch and exposing the underlying glass substrate. The edge of the scratch was imaged by AFM both dry and in water, and the thickness of the film was determined. Scans were made at various positions along the scratch to obtain an average measurement. The average film thickness was calculated by averaging the height measurements obtained from 5 positions, using the revealed glass as a baseline. Thicknesses measured on three separate films were averaged.

For nanoindentation studies, tips with 600 nm SiO₂ microspheres attached at the tip end (Novascan Technologies, IA) were used (14). Protein films with pre-determined thicknesses were immersed in water for at least 1 h at room temperature to allow equilibrium water uptake. Both the films and the cantilever assembly were submerged in water under ambient conditions during nanoindentation. Force curves were collected; the instrument records z (piezo) displacement and force, the product of measured tip deflection and cantilever spring constant. The maximum indentation force was set to 50

nN relative to the contact point. The tip speed was 1 $\mu\text{m}/\text{sec}$, and data were collected at 0.5 Hz.

The spring constants of the tips used for nanoindentation were determined to be about 0.3 N/m using thermal calibration in water. The Dimitriadis model (21) for indentation of linear-elastic soft material films of finite height with a spherical indenter was applied to the loading force data. Only force-indentation points between 20 nm and 10% maximum indentation were used to constrain the data to the near-linear response range. The elastic modulus was obtained by averaging the calculated moduli at multiple points in three separate films.

Human corneal epithelial (HCE) cell culture

Primary human corneal epithelial cells were obtained from ScienCell Research Laboratories (San Diego, CA, #6510) and Cascade Biologics (Portland, OR, #C-019-5C). All cells were maintained in serum-free EpiLife culture medium (with 60 μM CaCl_2 , Cascade Biologics) supplemented with Human Corneal Growth Supplement (HCGS containing bovine pituitary extract, bovine insulin, hydrocortisone, bovine transferrin, and mouse epidermal growth factor, Cascade Biologics). Gentamicin (10 $\mu\text{g}/\text{ml}$) and amphotericin (0.25 $\mu\text{g}/\text{ml}$) were also added to culture media. Serum-free EpiLife medium was used in all experiments to exclude extracellular matrix proteins (i.e., fibronectin, laminin) present in serum. Cells between passages 2 to 7 were used.

Cell spreading

Aliquots (500 μ l) of FN and BSA solutions were added to the wells of a transparent 24-well plate (Falcon BD, VWR, Batavia, IL) and allowed to adsorb overnight at 4 °C. In these experiments, fibronectin (FN, 10 μ g/ml in PBS, Chemicon, MA) was used as a positive control and bovine serum albumin (BSA, 2 mg/ml in PBS, Sigma) was used as a negative control. Subsequently, wells were rinsed twice with pre-warmed PBS solution and blocked with 500 μ l of 0.2 wt% heat-inactivated BSA solution at room temperature for 30 min. At the same time, coverslips containing spin-coated aECM protein films were mounted in empty wells by dotting sterile grease around the circumference of the coverslips. Gentle pressure was applied to ensure firm adhesion to the well. Finally, all wells were rinsed twice with pre-warmed PBS solution.

HCE cells were enzymatically passaged using 0.05 % Trypsin-0.25 % EDTA (Cascade Biologics). To each well, 4.8×10^4 cells were added together with 1 ml of fresh EpiLife medium. The plates were swirled gently to prevent clustering of cells and placed in an incubator at 37 °C under 5% CO₂/95 % air. Images of five random positions in each well were acquired after 4 hours. 200 cells were traced for each surface using ImageJ and their areas were recorded. Cells with projected areas above 300 μ m² (based on the average cell areas on BSA) were considered spread and the percentage of spread cells was plotted for each surface.

Wound healing

The experimental setup was adapted from Nikolić et al. with modifications (6). Slabs of polydimethylsiloxane (PDMS; Dow Corning, Midland, MI) were cast to 0.3 mm thickness according to the manufacturer's instructions. Briefly, PDMS was mixed at 10:1 PDMS base/curing agent ratio, poured into a 100 mm petri dish to 0.3 mm height, degassed in a desiccator for at least 1 h and baked for at least 2 h at 65 °C. Blocks of PDMS with lateral dimensions roughly 2 mm x 2 mm were cut with a sterile scalpel, sterilized with ethanol and air-dried. Use of thin (0.3 mm) blocks of PDMS allowed cells to maintain confluence across the edge of the block and prevented contact between cells and the underlying substrate surface.

The PDMS blocks were placed at the center of the coverslips containing spin-coated aECM films. These coverslips were then subsequently mounted in 24-well tissue culture plates by using sterile vacuum grease (Dow Corning, Midland, MI). To all wells, 500 µl of FN was added overnight at 4 °C to cover the entire surface to aid cell adhesion. The next day, 2×10^5 primary HCE cells were seeded into each well and allowed to grow to confluence in 3 – 5 days. The medium was changed every two days. Once a confluent monolayer formed, the PDMS blocks were lifted with sterile tweezers, creating a wounded cell sheet. A schematic drawing of the experimental set up is shown in Figure 2.2A.

Each well was rinsed twice with fresh medium before the start of each experiment to remove any cell debris. Meanwhile, a chamber was set up around the microscope to maintain the microscope stage and chamber interior at 37 °C with 5% CO₂/95% air to

sustain cells. A hole was made in the cover of one of the empty wells in the 24-well plate and the air supply was attached to ensure that cells were maintained under the CO₂/air mixture. Water was also added to surrounding empty wells to prevent excessive evaporation of the medium. Wound closure was followed for 30 h by time-lapse phase contrast microscopy on a Nikon Eclipse TE300 microscope at 10 x magnification. Digital images of at least 5 different spots of the wound edge for each substrate were acquired every 15 min using MetaMorph v6.3.2 (Molecular Devices, Sunnyvale, CA).

The wound areas immediately after wounding ($t = 0$ h) and after 30 h ($t = 30$ h) were traced manually using ImageJ v1.37 (NIH, USA, <http://rsb.info.nih.gov/ij/>). The difference in the two areas was then divided by the length of the wound edge to yield the distance traveled by the cell sheet. This distance was then divided by the total time (30 h) to give the wound closure rate. The overall wound closure rates were obtained by averaging the wound closure rates calculated from all the videos obtained from more than three independent experiments.

Cell tracking was performed to explain the differences in overall wound closure behaviors observed on surfaces with different RGD densities. Individual cells within the cell sheet were also tracked manually using ImageJ, with MTrackJ, a plug-in created by Meijering and colleagues at the University Medical Center Rotterdam, Netherlands (<http://www.bigr.nl/>). Trajectories of individual cells were tracked frame by frame for the last 10 h for each video. The average cell speed ($\mu\text{m}/\text{min}$) of an individual cell was

determined by averaging the speeds calculated in each 15 min interval. Only the cells that migrated on the test surface were included in the analysis.

The calculated cell speeds were slightly below the reported range of 60 – 80 $\mu\text{m/h}$ (19, 22). However, these differences could be characteristic of tissue culture monolayers and the use of serum-free media.

Interface-crossing experiments

aECM surfaces containing substrate interfaces were mounted into the wells of a 24-well tissue culture plate. HCE cells (1×10^4) were added to each well and allowed to attach for 2 h at 37 °C at 5% CO_2 / 95% air. Images of the interface at several positions on the aECM film were acquired every 15 min for 24 h using phase contrast microscopy at 37 °C at 5% CO_2 / 95% air.

Time-lapse videos were analyzed using ImageJ. We tracked cells that contacted the interface and recorded the time spent at the interface before a “decision” was made (i.e., the cell crossed the interface or moved away). We considered each encounter a separate “event” (i.e., once the cell leaves the interface and re-contacts the interface again, the timing restarts). The total amount of time spent at the interface and the subsequent decision (i.e., to cross the interface or not) were recorded for at least 150 events for each condition.

Statistical analysis

For all experimental data, the statistical significance of differences was estimated by analysis of variance followed by the Tukey test. Differences were taken to be significant at $P \leq 0.05$.

2.3 Results and discussion

Dehydrated films were determined to be in the range of 192.64 ± 19.27 nm ($n = 70$) in thickness; hydrated films were 349.15 ± 26.27 nm ($n = 36$) thick. Based on measured height differences, water content in hydrated films was estimated to be approximately 45%. The elastic modulus of a hydrated film was determined to be 0.24 ± 0.06 MPa ($n = 21$), which falls within the range previously determined for films of similar aECM proteins (14). There were no discernible physical differences between aE-RDG and aE-RGD films with varying RGD concentrations.

HCE cells were allowed to spread on spin-coated aECM films containing varying RGD densities. After 4 h, HCE cells were well-spread on crosslinked 100% RGD and on adsorbed FN, but remained rounded on the scrambled control (0% RGD) and on adsorbed BSA surfaces (Figures 2.1A – D). To quantify these differences, projected areas of 250 cells were measured at each of several time points over a 4 h period. Cells with projected areas larger than $300 \mu\text{m}^2$ were considered well-spread. The percentage of well-spread cells on aECM films increased with RGD density (Figure 2.1E). Although some cells eventually spread on the scrambled control substrate, spreading on the control surface was likely a consequence of cellular secretion of ECM proteins (23, 24).

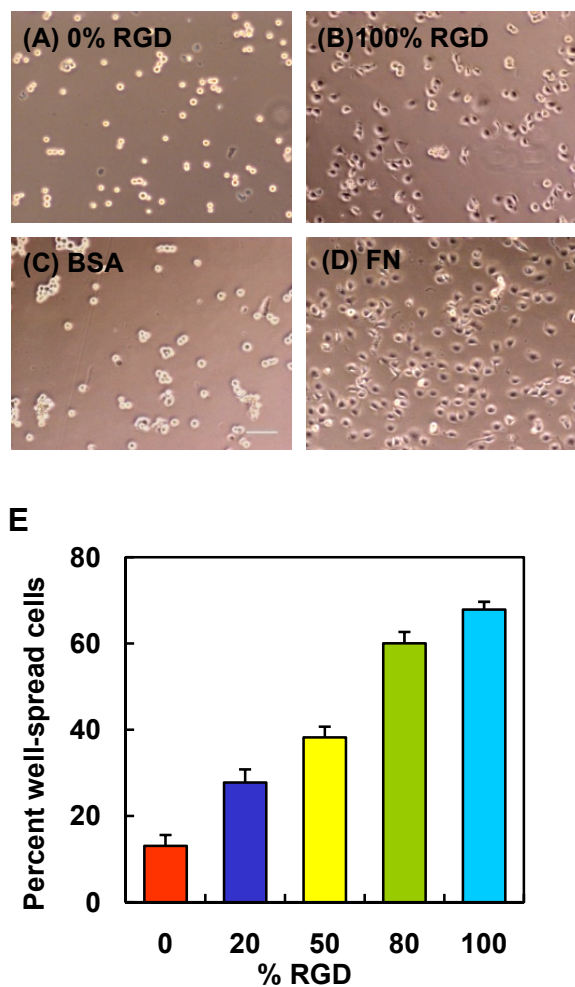


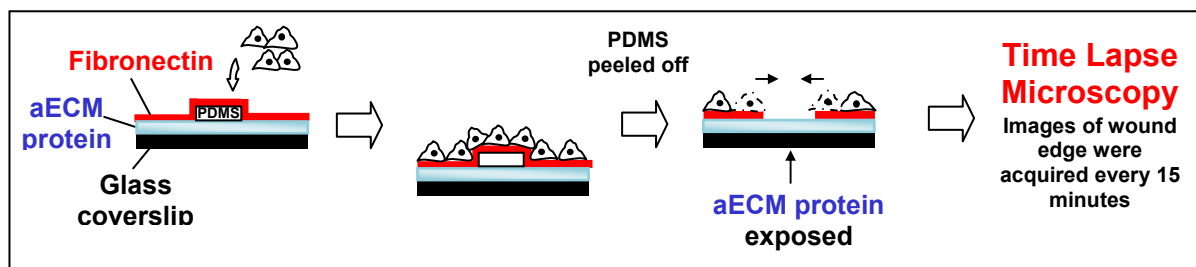
Figure 2.1 HCE cell spreading behavior on various substrates. Phase contrast images of HCE cells after 4 h on crosslinked spin-coated aECM films prepared from 0% RGD (**A**) or 100% RGD (**B**), adsorbed bovine serum albumin (BSA, **C**) and adsorbed fibronectin (FN, **D**). Scale bar = 100 μm . (**E**) Percent well-spread cells after 4 h on spin-coated aECM films with varying RGD densities. Error bars represent SEM.

Conventional scratch wound assays are limited by interference from proteins deposited by cells removed from the wound. Recent work of Nikolić et al. (6) and others (25) showed that removal of a PDMS barrier triggered cell responses similar to those

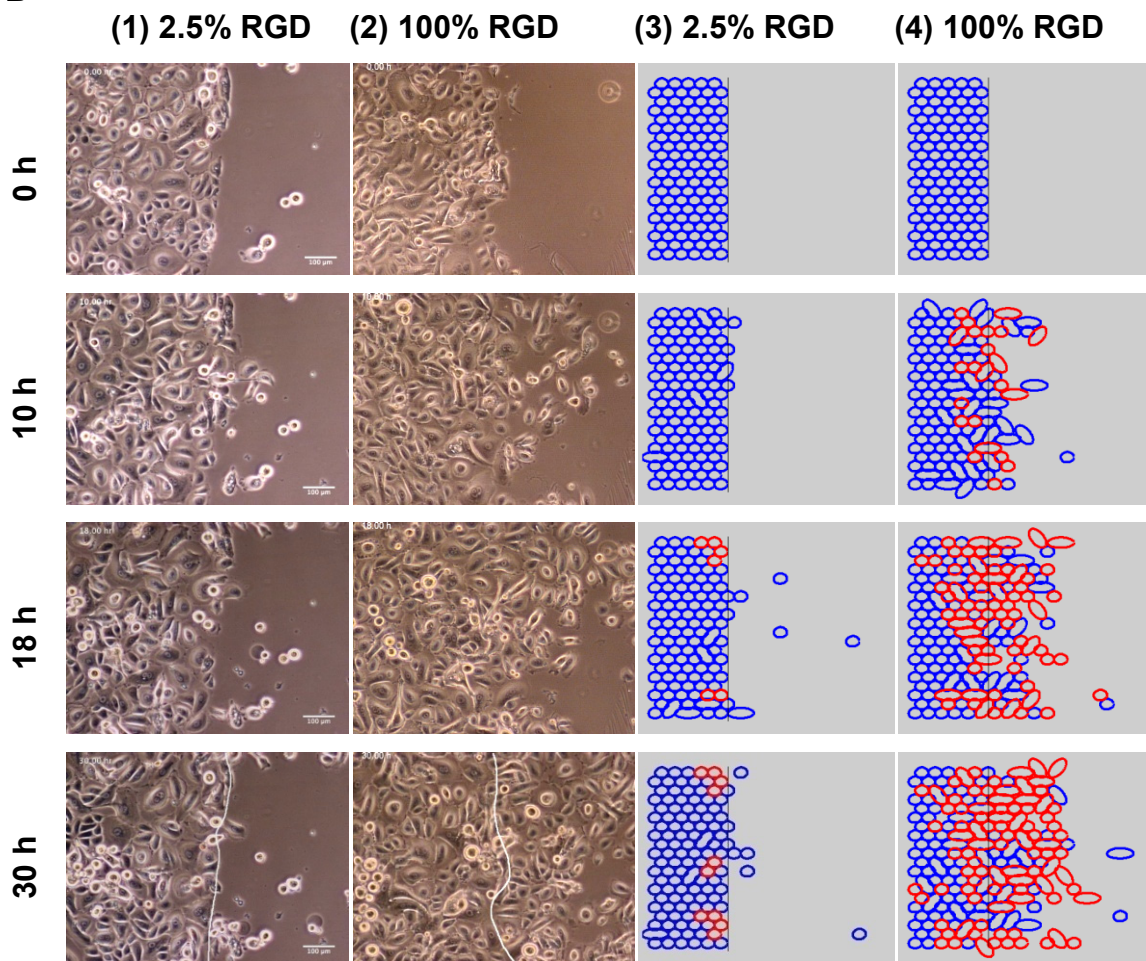
observed in scratch wound assays. Using a similar approach, we pre-coated glass coverslips with the protein of interest and laid down a short PDMS slab to provide a temporary platform for cell attachment. To facilitate cell attachment, fibronectin was incubated in each well overnight prior to plating of HCE cells (Figure 2.2A). Removal of the PDMS slab placed the edge of the wounded cell sheet in contact with the test surface.

HCE cells migrated collectively in the direction of the wound by lamellipodial crawling on 100% RGD, consistent with previous reports (5, 26). On 2.5% RGD, however, minimal advance of the cell sheet was observed, even though cells at the wound edge were constantly extending protrusions (Figure 2.2B). Figure 2.3A shows the average displacement of the cell sheet on various surfaces as a function of time. The overall wound closure rate increases approximately 5.6-fold as the RGD density increases (Figure 2.3B and Table A1). Individual cells within the cell sheet were also tracked for the last 10 h of each video (Figure 2.3C). Cells were selected at random and only cells that migrated on the test surface were included in the analysis. Surprisingly, the cells did not migrate significantly faster on 100% RGD than on 2.5% RGD.

A



B



C

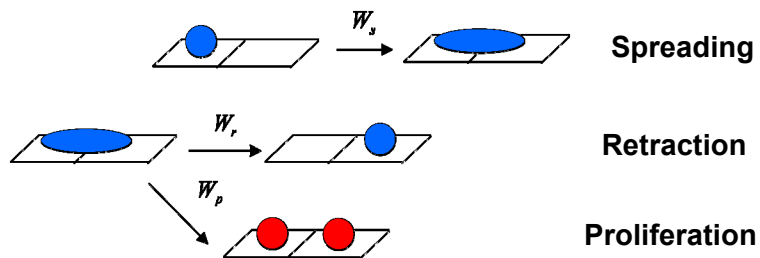


Figure 2.2 (A) Schematic of wound healing experiment. Cross-linked aECM proteins were spin-coated onto glass coverslips and mounted in tissue culture multi-well plates. A slab of PDMS was laid on top of the protein film and fibronectin solution was allowed to adsorb overnight at 4 °C to aid cell attachment. HCE cells were grown to confluence and the PDMS was peeled off. The protein film was rinsed twice with serum-free media and the wounded cell sheets were allowed to migrate over the aECM protein. This process was monitored by time lapse microscopy. **(B)** Time course wound healing on 2.5% RGD and 100% RGD substrates. (Panels **1** and **2**) Experimental images showing the progression of the wound edge on 2.5% and 100% RGD, respectively, at various time intervals. (Panels **3** and **4**) Comparative snapshots of wound edges for 2.5% RGD and 100% RGD substrates. Cells that have divided are represented as red cells. The initial positions of the wound edge (i.e., the position of the interface) are indicated by white lines in the images at 30 h. **(C)** Schematic of the Monte-Carlo simulation. In the model, cells can either spread with W_s to take up two lattice sites; retract to either one of the sites with W_r , or undergo proliferation with W_p .

This result was puzzling — we expected the increase in wound closure rate with RGD concentration to be a consequence of an increase in cell speed. How can the rate of wound closure increase when cell speed does not? We imagined that the critical event might be the “decision” made by each cell as it comes in contact with the test surface. Does the cell cross to the test surface or retreat to the matrix deposited beneath the confluent cell monolayer? If the rate of crossing depends on the adhesivity of the test surface, it seemed likely that wound healing should occur more rapidly on surfaces bearing higher RGD densities. In order to test this hypothesis, we performed computer simulations of the healing process.

The surface was modeled as a 2D hexagonal lattice in which each lattice site was either occupied by a cell or empty. Cell migration in the simulation proceeds via a two-step mechanism; first, the cell spreads onto an adjacent lattice site, and then it retracts to a single lattice site (Figure 2.2C). If retraction vacates the site occupied by the cell before it spread, migration has occurred.

We define the x -axis as the axis perpendicular to the wound edge, and the initial position of the wound edge (the boundary) as $x = 0$. Thus, in the initial configuration of the simulation, cells occupy all the lattice sites whose x positions are smaller than zero, and the rest of the sites are empty. As the simulation progresses, cells cross the boundary into the wound area and the value of x at the wound edge position increases.

We denote the transition probabilities for spreading, retraction, and proliferation by W_s , W_r , and W_p respectively. We use a simple model for spreading and retraction behavior to estimate the values of W_s and W_r for the different surfaces, based on experimental data (see supporting information for model details). Since FN is a major component of the matrix deposited beneath the confluent monolayer, the probabilities for spreading and retraction for lattice sites with $x < 0$ were taken to be those for FN. We estimated the proliferation rate (W_p) by constructing rate equations according to the simulation rules and solving them in the low cell concentration limit. The doubling time was then compared to experimental data. Details of the simulation scheme can be found in the supporting information of this chapter.

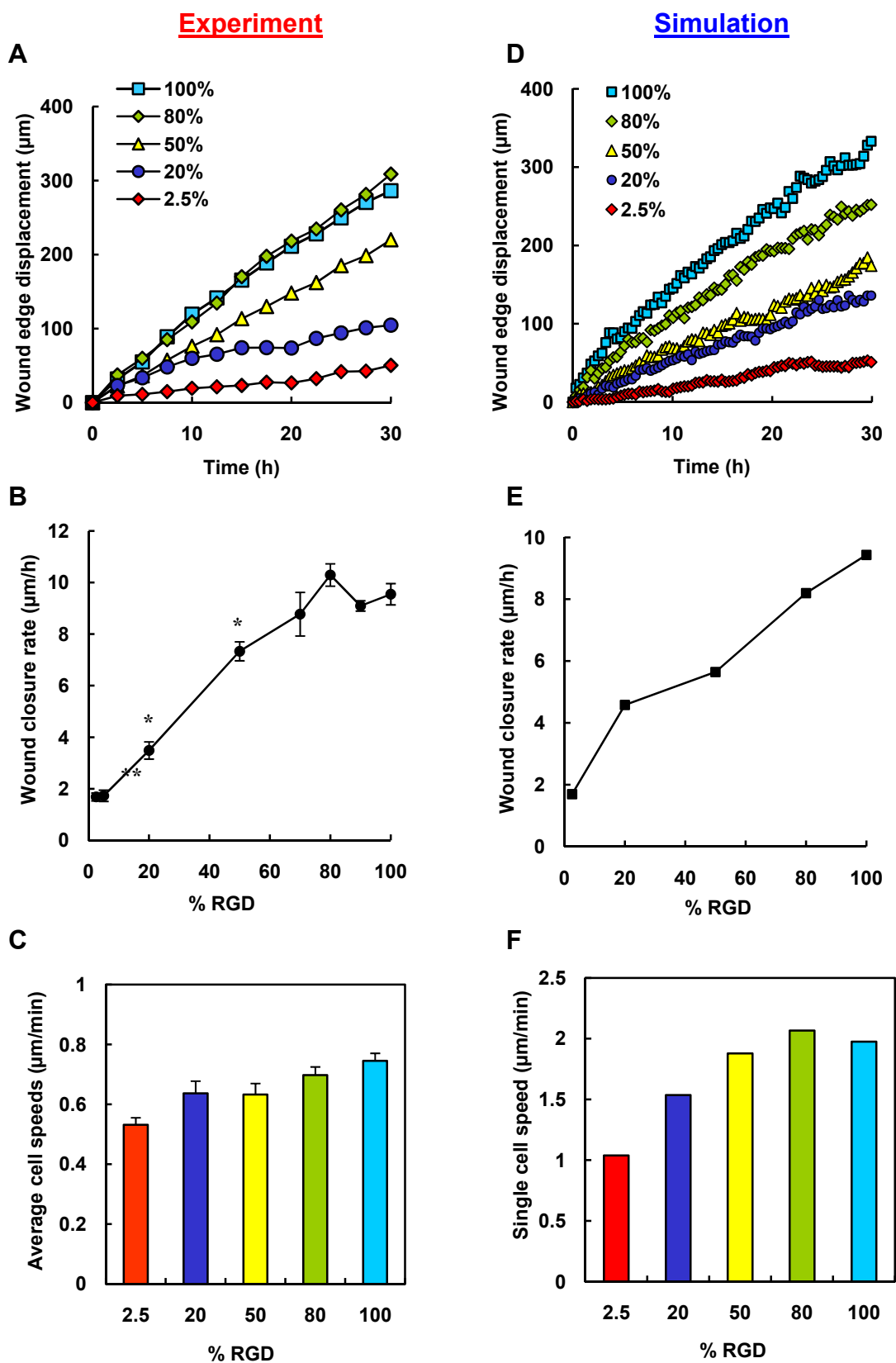


Figure 2.3 Wound healing behavior observed in experiments (A to C) and simulations (D to F). (A) Displacement of the wound edge for various surfaces over time. (B) Wound closure rate for substrates with varying RGD densities. *, significant difference from 100% RGD ($P < 0.05$). (C) Average cell speeds for individual cells migrating on the test surface for the last 10 h. (D) Displacement of simulated wound edges as a function of time. (E) Wound closure rate as a function of RGD percentage. The wound closure rate is five fold faster on 100% RGD than on 2.5% RGD, consistent with experimental observations. (F) Single cell speed as a function of RGD concentration. Only cells on the test surface were included. Error bars represent SEM.

The cells in the simulation behaved similarly to those observed experimentally, in the dynamic nature of their bonds and in the difference in cell behaviors observed on surfaces that present different densities of RGD ligands. Figure 2.2B compares snapshots taken from the simulation and from experiments for the 100% and 2.5% RGD surfaces. The wound closure rates derived from the simulation are shown in Figure 2.3E. The wound closure rate is defined as the average distance traveled by the wound edge per unit time (Figure 2.3D). As observed experimentally, there is a 5.6-fold difference between the wound closure rates on the 100% and on 2.5% RGD surfaces. Figure 2.3F shows the single cell speeds calculated from the simulation for surfaces bearing various RGD densities. At each time point, only cells on the test surface were included in the analysis. The difference between the single cell speeds on 100% RGD and 2.5% RGD is only 1.9-fold. These observations are consistent with the experimental results, and confirm that the increase in overall wound closure rate does not require faster cell migration.

The probability that a cell crosses the matrix boundary is given by its probability to spread onto the RGD test surface multiplied by its probability to retract from the FN surface, i.e., $W_s^{RGD} \times W_r^{FN}$. Hence, the ratio of the probabilities for crossing to the 100% RGD and 2.5% RGD test surfaces is: $P_{FN \rightarrow 100\%RGD} / P_{FN \rightarrow 2.5\%RGD} = W_s^{100\%RGD} / W_s^{2.5\%RGD} = 5.3$. The second equality was obtained from the spreading rates used in the simulation. As explained in detail in the supporting information, we used the cell spreading assay data (Figure 2.1E) to determine these rates. Hence, the 5.3-fold difference in crossing probability arises from the 5.3-fold difference in the rate of cell spreading. Following the same logic, we can also explain the small differences in cell speed observed on surfaces with different RGD concentrations. The ratio between single cell migration rates on 100% and 2.5% RGD is $W_s^{100\%RGD} \times W_r^{100\%RGD} / W_s^{2.5\%RGD} \times W_r^{2.5\%RGD} = 1.8$.

The simulation results suggest that the 5.6-fold variation in wound closure rates observed experimentally arises primarily from variation in boundary-crossing rates (Figure 2.5B and see supporting information, Figure A7). To measure boundary-crossing rates directly, we prepared substrates by spin-coating one layer of aECM protein on top of another (Figure 2.4). A typical surface used for studying the crossing probabilities was imaged by AFM. The height of the step at the boundary was 119.2 ± 14 nm ($n = 30$).

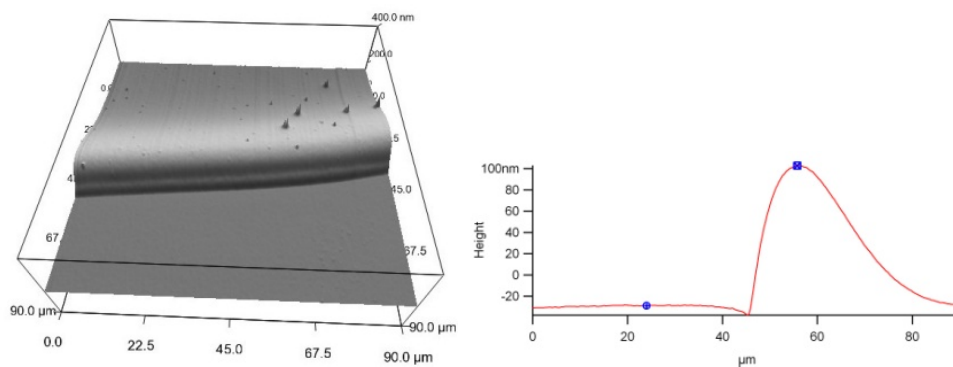


Figure 2.4 Image of typical substrate with an interface imaged using an atomic force microscope (left). A cross-section of the interface region is also shown (right).

Single HCE cells were seeded on these surfaces, and cells at the boundary were followed by time-lapse microscopy. The total time in contact with the boundary and the subsequent decision (i.e., to cross the boundary or not) were recorded for each cell. The crossing rate was calculated by dividing the number of crossings by the total time in contact with the boundary (see supporting information for crossing rate calculations). The results confirm that the crossing rate increases 5.7-fold as the adhesivity of the substrate increases (Figure 2.5C), supporting the hypothesis that the variation in wound closure rate is determined primarily by variation in the rate of boundary crossing.

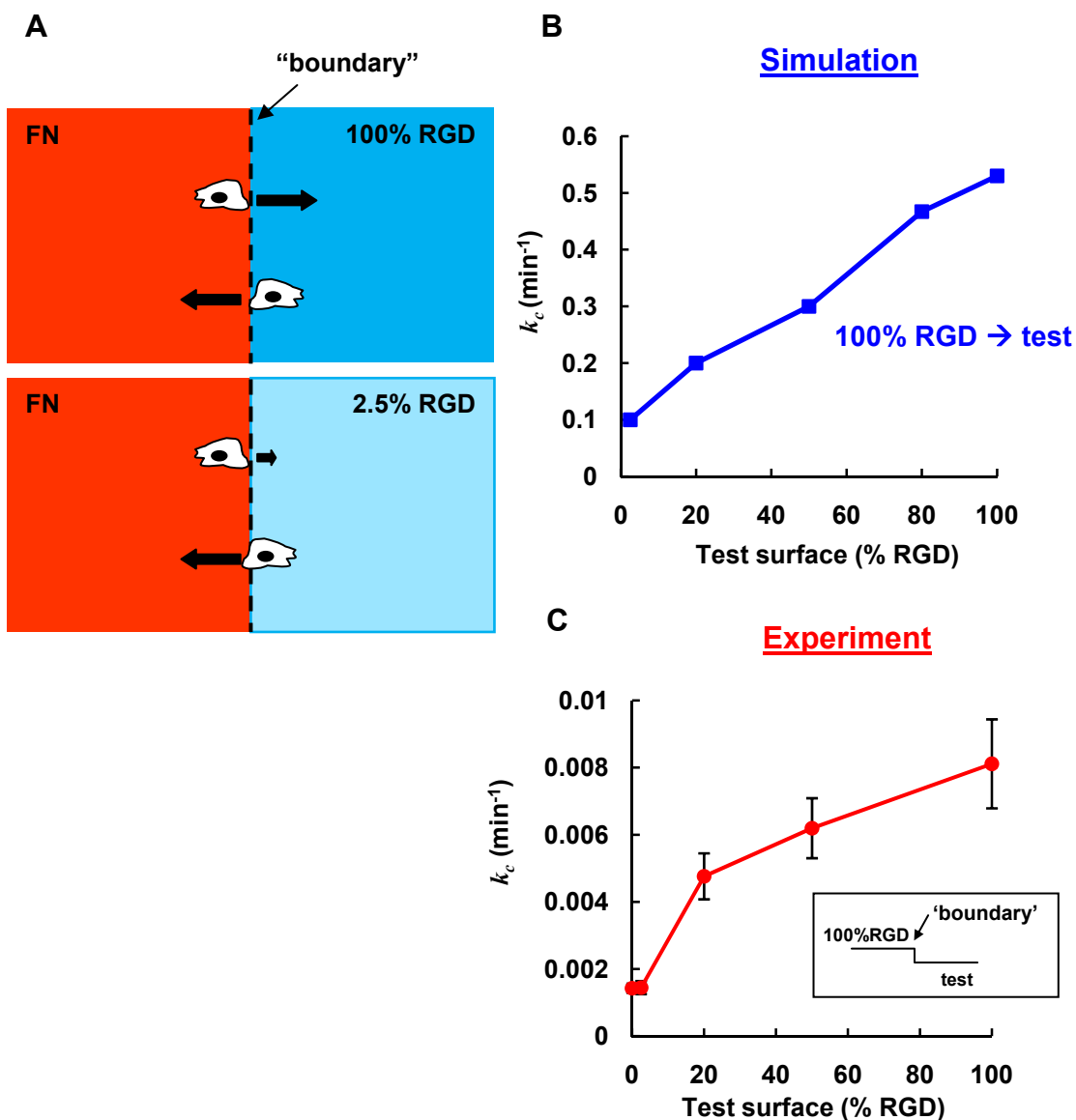


Figure 2.5 (A) Schematic representation of boundary crossing. Black arrows represent relative crossing rates for each condition. (B and C) show the rate constants of crossing, k_c (from 100% RGD to the test surfaces) for simulation and experimental data, respectively. In both curves, the crossing rates from 100% RGD to 100% RGD and from 100% RGD to 2.5% RGD differ by a factor of five. Error bars in C are experimental errors (see supporting information for this chapter).

2.4 Conclusions

In summary, we find that the rate of healing of epithelial cell monolayers cultured on aECM proteins increases with increasing density of adhesion ligands presented at the substrate surface. As shown both experimentally and through simulation of the healing process, the variation in healing rate arises not from variation in the rate of cell migration, but instead from variation in the rate at which cells cross the boundary between the matrix deposited by the cell monolayer and the aECM protein. The simulation method described here can be applied to many cell types, and — through variation in the cell-cell interaction energy (see supporting information) — captures a broad range of wound healing behavior, from diffusion-like behavior in which cell-cell contacts break and reform (as observed for corneal epithelial cells) to behavior that resembles that of an elastic sheet in which cell-cell contacts remain unchanged during wound healing (as observed in monolayers of MDCK cells (27)).

2.5 Acknowledgements

We acknowledge Drs. Julie Liu, Paul Nowatzki, and Stacey Maskarinec for help with protein expression and cell culture. We also thank Dr. Zhen-Gang Wang for useful advice on the simulation model. E.F. is supported by the Nanyang Overseas Scholarship, Singapore; S.T. is supported by the Human Frontier Science Program Cross-Disciplinary Fellowship. This work is funded by the NSF Center for the Science and Engineering at Caltech and by NIH grant EB1971.

2.6 References

1. P. Martin, J. Lewis, *Science* **360**, 179 (1992).
2. W. M. Bement, P. Forscher, M. S. Mooseker, *J. Cell. Biol.* **121**, 565 (1993).
3. P. J. Sammak, L. E. Hinman, P. O. T. Tran, M. D. Sjaastad, T. E. Machen, *J. Cell Sci.* **110**, 465 (1997).
4. M. Poujade et al., *Proc. Natl. Acad. Sci. U.S.A.* **104**, 15988 (2007).
5. E. R. Block, A. R. Matela, N. SundarRaj, E. R. Iszkula, J. K. Klarlund, *J. Biol. Chem.* **279**, 24307 (2004).
6. D. L. Nikolic, A. N. Boettiger, D. Bar-Sagi, J. D. Carbeck, S. Y. Shvartsman, *Am. J. Physiol. Cell Physiol.* **291**, 68 (2005).
7. G. J. Todaro, G. K. Lazar, H. Green, *J. Cell Physiol.* **66**, 325 (1965).
8. K. Suzuki, J. Saito, R. Yanai, N. Yamada, T. Chikama, K. Seki, T. Nishida, *Prog. Ret. Eye Res.* **22**, 113 (2003).
9. R. A. F. Clark, *J. Invest. Dermatol.* **94**, 128S (1990).
10. S. P. Palecek, J. C. Loftus, M. H. Ginsberg, D. A. Lauffenburger, A. F. Horwitz, *Nature* **385**, 537 (1997).
11. D. K. Pettit, A. S. Hoffman, T. A. Horbett, *J. Biomed. Mater. Res.* **28**, 685 (1994).

12. R. van Horssen, N. Galjart, J. A. P. Rens, A. M. M. Eggermont, T. L. M. ten Hagen, *J. Cell Biochem.* **99**, 1536 (2006).
13. L. Aucoin, C. M. Griffith, G. Plezrier, Y. Deslandes, H. Sheardown, *J. Biomater. Sci. Polymer Edn.* **13**, 447 (2002).
14. P. J. Nowatzki, D. A. Tirrell, *Biomaterials*, 1261 (2003).
15. K. Di Zio, D. A. Tirrell, *Macromolecules* **36**, 1553 (2003).
16. J. C. Liu, S. C. Heilshorn, D. A. Tirrell, *Biomacromolecules* **5**, 497 (2003).
17. S. C. Heilshorn, K. A. Di Zio, E. R. Welsh, D. A. Tirrell, *Biomaterials* **24**, 4245 (2003).
18. J. C. Liu, D. A. Tirrell, *Biomacromolecules* **9**, 2984 (2008).
19. L. Luo, P. S. Reinach, W. W. Y. Kao, *Exp. Biol. Med. Vol.* **226**, 653 (2001).
20. M. A. Stepp, *Exp. Eye Res.* **83**, 3 (2006).
21. E. K. Dimitriadis, F. Horkay, J. Maresca, B. Kachar, R. S. Chadwick, *Biophys. J.* **82**, 2798 (2002).
22. M. Zhao, B. Song, J. Pu, J. V. Forrester, C. D. McCaig, *FASEB J.* **17**, 397 (2003).
23. M. D. M. Evans, J. G. Steele, *J. Biomed. Mater. Res.* **40**, 621 (1997).
24. M. D. M. Evans, J. G. Steele, *Exp. Cell Res.* **233**, 88 (1997).
25. K. Y. Chan, D. L. Patton, Y. T. Cosgrove, *Invest. Ophthalmol. Vis. Sci.* **30**, 2488 (1989).
26. R. Farooqui, G. Fenteany, *J. Cell Sci.* **118**, 51 (2005).

ADDITIONAL INFORMATION FOR CHAPTER 2

A

M-MASMTGGQMG-HHHHHHH-*DDDDK* (LD-YAVTGRGDSPASSKIA ((VPGIG)₂VPGKG(VPGIG)₂)₄VP)₃-LE

T7 tag His tag cleavage site RGD cell-binding domain Elastin-like repeats

B

M-MASMTGGQMG-HHHHHHH-*DDDDK* (LD-YAVTGRDGSPASSKIA ((VPGIG)₂VPGKG(VPGIG)₂)₄VP)₃-LE

Scrambled RGD domain

Figure A1. Amino acid sequences of aECM proteins containing (A) RGD and (B) RDG cell-binding domains. Each aECM protein contained a T7 tag, a hexahistidine tag, an enterokinase cleavage site, and elastin-like domains containing lysine residues (italicized) for crosslinking.

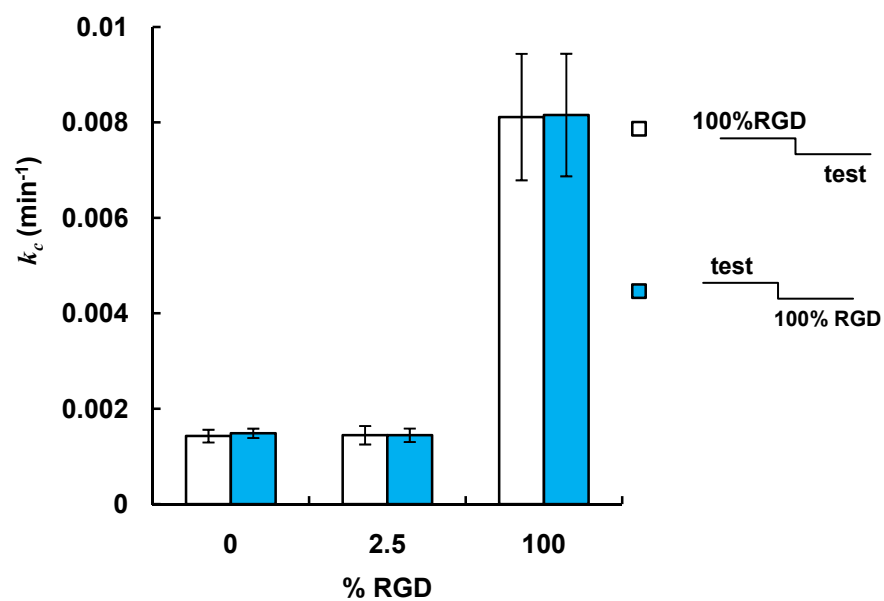


Figure A2. Rate constants of interface crossing, k_c from 100% RGD into various test surfaces. The crossing probabilities computed for both configurations of the interface. There were no significant differences between the rate constants for the two configurations of each test surface, suggesting that the small “step” at the interface did not affect the boundary-crossing rate.

Mathematical model

A simple model for spreading and retraction

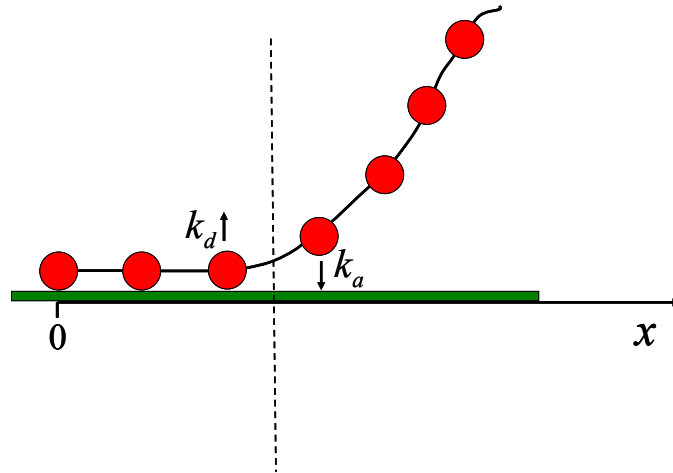


Figure A3. A schematic illustration of the cell spreading and retraction model. The beads represent integrin receptor clusters, while the chain represents the cell membrane. The cell edge is represented by the dashed line. Receptor clusters adjacent to the cell edge can adsorb or desorb with rate constants k_a and k_d respectively.

We use a simplified picture for cell spreading and retraction in order to estimate numerical values for the speed of these processes. In Fig. A3, the cell membrane is modeled as a chain of beads which represent integrin receptors or clusters. Both spreading and retraction advance through adsorption and desorption of receptor clusters at the ligand-bearing surface. Only the receptor clusters adjacent to the cell edge (represented by the dashed line in Fig. A3) can adsorb or desorb. The rate constants for adsorption and desorption are k_a and k_d , respectively.

During spreading and retraction, the cell edge performs a random walk where each adsorption event results in an increase in its x position while each desorption event results in a decrease in its x position.

The master equation, describing the processes discussed above, is of the form:

$$(1) \quad \frac{dP(x,t)}{dt} = k_a P(x-1,t) + k_d P(x+1,t) - (k_a + k_d) P(x,t)$$

where $P(x,t)$ is the probability of the cell edge to be at position x at time t , and x is measured in units equal to the average distance between receptor clusters.

The solution for the average cell edge displacement is:

$$(2) \quad \langle x \rangle = (k_a - k_d) \cdot t$$

An increase in $\langle x \rangle$ corresponds to an increase in the cell area in contact with the surface.

Therefore, we define the spreading rate, W_s , as the change in the average value of x with time:

$$(3) \quad W_s = \frac{d\langle x \rangle}{dt} = (k_a^s - k_d^s)$$

Similarly, the retraction rate, W_r , is defined as:

$$(4) \quad W_r = -\frac{d\langle x \rangle}{dt} = (k_d^r - k_a^r)$$

The forces exerted by the cell influence the effective rate of receptor adsorption and desorption events (k_a and k_d). Since, the forces exerted by the cell are different when the

cell is in a state of spreading or retraction, the rate constants for adsorption and desorption in these two cases will be different. Consequently, we add a superscript in Equations 3 and 4 (*s* or *r*) to denote the cell state (spreading or retraction).

In a cell-free system with receptors incorporated in a rigid planar membrane, the binding of the receptors to the surface ligands, can be described as a second order reaction. Denoting the rate constant for binding by k and the rate constant for unbinding by k_{-1} , the ratio between these rate constants is: $k_{-1}/k = \exp(-\varepsilon/k_B T)$ where $\varepsilon > 0$ is the binding energy (the difference in energy between the unbound and bound states).

For the case of a flexible membrane, the spreading process is associated with a change in membrane shape. The shape deformation results in an energy barrier which we denote by ε_{el} .

Spreading and retraction processes are not spontaneous and require forces to be applied by the cell (1). In the case of spreading, a protrusive force is exerted on the cell membrane, thereby reducing the energy barrier associated with membrane deformation in an amount $f\gamma$ where f is the force applied by the cell and γ is the length along which the force is applied (2, 3). In this case the rate constants for adsorption and desorption in our model are:

$$(5) \quad k_a^s = k \exp(-\varepsilon_{el}/k_B T + f\gamma/k_B T), \quad k_d^s = k \exp(-\varepsilon/k_B T)$$

When retracting, the cell pulls on the receptor-ligand bond, thereby reducing the energy barrier associated with bond breakage in an amount $f'\gamma'$ (1, 2).

In this case, the rate constants take the form:

$$(6) \quad k_a^r = k \exp(-\varepsilon_{el} / k_B T), \quad k_d^r = k \exp(-\varepsilon / k_B T + f'\gamma' / k_B T)$$

Following Equations 3 - 6, the rates for spreading and retraction can be expressed as:

$$(7) \quad W_s = k \exp(-\varepsilon_{el} / k_B T + f\gamma / k_B T) - k \exp(-\varepsilon / k_B T)$$

$$(8) \quad W_r = k \exp(-\varepsilon / k_B T + f'\gamma' / k_B T) - k \exp(-\varepsilon_{el} / k_B T)$$

Using equations 7 - 8, we can connect between the spreading and retraction rates on surfaces with the same RGD fraction, φ_{RGD} :

$$(9) \quad \tilde{W}_r(\varphi_{RGD}) = \exp(f'\gamma' / k_B T) \left[A - \tilde{W}_s(\varphi_{RGD}) \right] - k \exp(-\varepsilon_{el} / k_B T) / W_s(FN)$$

In Equation 9, $W_s(FN)$ denotes the spreading rate on fibronectin, $\tilde{W}_s(\varphi_{RGD}) = W_s(\varphi_{RGD}) / W_s(FN)$ and $\tilde{W}_r(\varphi_{RGD}) = W_r(\varphi_{RGD}) / W_s(FN)$ are the spreading and retraction rates relative to the spreading rate on fibronectin and $A \equiv k \exp(-\varepsilon_{el} / k_B T + f\gamma / k_B T) / W_s(FN)$.

We can use the results from the spreading assay (Fig. 2.1E) in order to get a numerical value for the constant A . If we assume that the binding energy, ε is proportional to the RGD fraction on the surface, i.e., $\varepsilon = \tilde{\varepsilon}\varphi_{RGD}$, we get

$$(10) \quad \tilde{W}_s = A - B \exp(-\tilde{\epsilon}\phi_{RGD} / k_B T)$$

where $B \equiv k/W_s(FN)$.

The percent spread cells on aECM with different RGD concentrations after 4 h (shown in Fig. 2.1E) relative to the percent of spread cells on FN after 4 h, was taken as a measure for the relative rate of cell spreading, \tilde{W}_s , and was fitted to Equation 10. The fit is shown in Fig. A4.

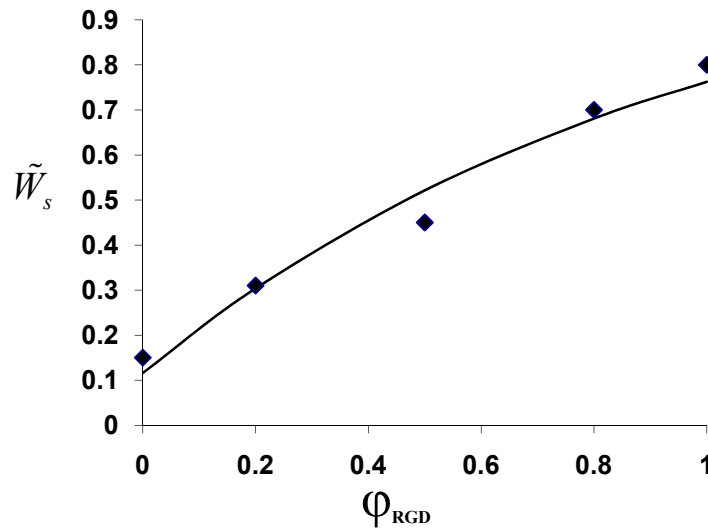


Figure A4. The fit of the experimental spreading data to the theoretical expression for the relative spreading rate, Equation 10.

Out of the fit we obtain $A = 1.11$

The rest of the model parameters were estimated on the basis of experimental results described in the literature:

1. γ is the characteristic distance between bonds between the cell and the substrate (the distance between beads in our model) and is estimated to be 100 nm (4).
2. The characteristic traction force is assumed in the literature to be on the order of $1 \text{ nN}/\mu\text{m}^2$ (3, 5, 6) and the protrusion has a typical diameter of $0.1 \mu\text{m}$ (6), comparable to the average distance between bonds (4). These estimates lead to a traction force, f' , on the order of 8 pN. The RGD-integrin bond length, γ' , is on the order of 1 nm (2, 3).
3. Recent estimates suggest that the thermal deformation of the membrane is on the order of 5-10 nm (6, 7) implying that the energy required for deformation on the scale of the distance between bonds ($\sim 100 \text{ nm}$) cannot be provided by thermal fluctuations. Consequently, we assume that the term $\exp(-\varepsilon_{el}/k_B T)$ in Equation 9 is negligible.

The rates of spreading and retraction in the simulation are measured in units of the spreading on FN, i.e., the values used in the simulation are \tilde{W}_s and \tilde{W}_r , respectively.

Notice that in these units, $\tilde{W}_s(FN) = W_s(FN)/W_s(FN) = 1$. For each RGD concentration, φ_{RGD} , the spreading rate, $\tilde{W}_s(\varphi_{RGD})$ was taken from the experimental data presented in

Fig. A4. The value for the retraction rate on the same surface, $\tilde{W}_r(\varphi_{RGD})$ was calculated using Equation 9.

Estimation of the proliferation rate

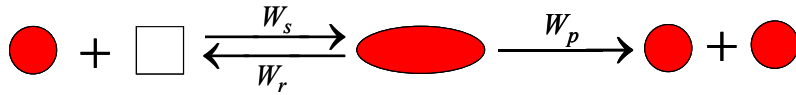


Figure A5. An illustration of the proliferation kinetic scheme. The white box represents an empty neighboring lattice site on which the cell can spread in order to proliferate.

The number of cells confined to a single lattice site is denoted by n_1 (●); the number of spread on two adjacent lattice sites by: n_2 (◻). The empty square in Fig. A5 represents an empty neighboring site on the lattice. The rates for spreading, retraction and proliferation steps are denoted by W_s , W_r and W_p respectively.

In our model, only cells that are spread on two adjacent lattice sites can proliferate. This assumption is consistent with the observation that decreased cell spreading can inhibit proliferation signals (8), and it creates an effective time lag between consecutive cell divisions, resembling inter-phase (9).

The rate equations for the kinetic scheme illustrated in Fig. A5 are:

$$(10) \quad \frac{dn_1}{dt} = -W_s n_1 (1 - n_1/n_1^* - n_2/n_2^*) + W_r n_2 + 2W_p n_2$$

$$(11) \quad \frac{dn_2}{dt} = W_s n_1 (1 - n_1/n_1^* - n_2/n_2^*) - W_r n_2 - W_p n_2$$

The first term is the rate of spreading, where the probability to find a neighboring empty lattice site is taken to be the mean field probability, i.e., $P_{empty_site} = (1 - \theta)$ where θ is the fraction of occupied sites on the lattice and is given by $\theta = n_1/n_1^* + n_2/n_2^*$ where n_1^* is the number of cells that occupy a single site when at confluence. Likewise, n_2^* is the number of cells that occupy two adjacent sites at confluence.

The change in the total number of cells $n = n_1 + n_2$ is then:

$$(12) \quad \frac{dn}{dt} = \frac{dn_1}{dt} + \frac{dn_2}{dt} = W_p n_2$$

Since for most cases, $W_p \ll W_r, W_s$, we can assume fast equilibrium in order to solve the rate equations (Equations 10 - 12). In the limit of low cell concentration ($n_1/n_1^* \ll 1$), we get the expected exponential growth:

$$(13) \quad \frac{dn}{dt} = \frac{W_p}{1 + \left(\frac{W_r}{W_s}\right)} n$$

The doubling time, t_D , for a cell population which grows according to the kinetic scheme presented in Fig. A5 is:

$$(13) \quad t_D = \frac{\ln 2}{W_p} (1 + W_r/W_s)$$

According to the literature, the doubling time for human corneal epithelial (HCE) cells is estimated to be 25 h (10). Using the values for W_r and W_s on FN, we get $W_p = 0.05h^{-1}$.

We assume that W_p is identical on all the surfaces.

Simulation details

We use a dynamic Monte Carlo scheme (11, 12) to simulate the dynamics of collective cell migration. The surface is modeled as 100×100 hexagonal lattice with a lattice constant of $d = 50 \mu\text{m}$, which is on the order of a cell diameter. At time $t = 0$, the first 10 columns of the lattice are occupied by cells (total number of cells, $N = 1000$), while the rest of the lattice sites are empty. Since proliferation is enabled, N increases with time.

In every Monte Carlo step, N cells are chosen randomly and an attempt is made to change their state according to the appropriate probabilities. As explained before, the spreading rate on fibronectin (FN) in the simulation is defined as 1 and the rest of the rates are calibrated accordingly. All the rates in the simulation are scaled to make sure that the time steps are small enough so that in any Monte-Carlo (MC) step only one event can occur. The conversion between simulation time and experimental time was done by a one-time calibration, equating the wound closure rate for the case of 2.5% RGD obtained from the simulation and from the experiment. Working backwards we get: 1 MC step equals 0.15 min and $W_s(FN) = 0.54 \text{ min}^{-1}$.

Cell-cell interactions

Wound healing behavior depends not only on cell-aECM interaction but also on the inter-cellular interaction. The energy of a cell fluctuates, but unlike in a fluid, the origin of the fluctuations is not collisions with the solvent or the thermal energy. The fluctuations in energy in a cellular system originate from fluctuations around the steady state of the biochemical networks of the cell (13). Consequently, it is accepted to define an effective temperature $T_{eff} = F_T / k_B$ where F_T is the magnitude of the energy fluctuations and k_B is the Boltzmann constant (14-16). As a result, the probability of a cell to have an energy fluctuation ε' is $\exp(-\varepsilon' / F_T)$.

In the simulation, we measure the intercellular interaction energy, $\varepsilon_{cell-cell}$, in units of F_T and use a value of $\varepsilon_{cell-cell} / F_T = 1.0$. The interaction energy between cells comes into play in the simulation for the case of cell retraction. When a cell retracts, there is an active force that pulls it from the surface and from its neighbors as explained in the model for spreading and retraction (see section of model for spreading and retraction). This force can either lead to cell-cell bond breakage or to retraction of the cell, pulling the neighboring cell along.

Let us denote the number of neighbors that the cell in question would lose upon retraction by ν . The cell can retract and break the bonds with its neighbors with probability $W_r \times (\exp(-\varepsilon_{cell-cell} / F_T))^\nu$. Or the cell can retract, break the bonds with $\nu - 1$ of its neighbors and pull the remaining cells with it with probability $W_r \times (\exp(-\varepsilon_{cell-cell} / F_T))^{\nu-1}$.

A neighboring cell can only be stretched if it occupies a single lattice site. This is to ensure that the total elastic energy of the cell does not exceed the cell fluctuation energy F_T .

Single cell crossing rates

When a cell is at the interface, it can either cross the interface with a rate constant, k_c or move away from the interface with a rate constant, k_b as illustrated in the schematic figure below.

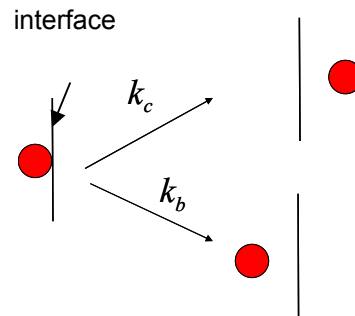


Figure A6. Schematic diagram of cell at an interface, showing two possible outcomes. A cell can cross the interface with a rate constant k_c , or it can move away with a rate constant, k_b .

From the time-lapse movies, we recorded the time spent by the cell at the interface until a reaction occurs (i.e., waiting time), as well as the outcome (i.e. crossing or moving away). In order to extract the rate constant for interface crossing from the experiment, it is necessary to know the waiting time distribution for cells at the interface.

Let us define $P_0(t; t_0)$ as the probability that no event occurs in the interval $(t_0, t_0 + t)$ and assume that the events are independent and the rate constants do not depend on time.

Then, $P_0(t+dt; t_0) = P_0(t; t_0) \times \left(1 - \sum_i k_i dt\right)$, where k_i is the rate constant for event i (in our case: $i = c, b$).

$$\text{Consequently, } \frac{P_0(t+dt; t_0) - P_0(t; t_0)}{dt} = \left(-\sum_i k_i\right) P_0(t; t_0)$$

And in the limit of $dt \rightarrow 0$, we get:

$$\frac{dP_0(t)}{dt} = \left(-\sum_i k_i\right) P_0(t) \text{ so that } P_0(t) = \exp\left(-\sum_i k_i \times t\right)$$

We denote the waiting time distribution as $w(t)$. The waiting time distribution can be expressed as:

$$w(t) = \frac{P_0(t) - P_0(t+dt)}{dt} = -\frac{d}{dt} P_0(t)$$

and hence,

$$(14) \quad w(t) = K \exp(-Kt)$$

where $K = \sum_i k_i$ is the sum of the rate constants for all possible events.

Using the waiting time distribution (Equation 14), the average waiting time is:

$$(15) \quad \langle t \rangle = \frac{\int_0^{\infty} t \times K \exp(-Kt) dt}{\int_0^{\infty} K \exp(-Kt) dt} = \frac{1}{K}$$

In the case of the cell crossing experiment, the waiting at the interface can end with either crossing of the interface (k_c) or with bouncing back (k_b) and thus, $\langle t \rangle = 1/(k_c + k_b)$.

If we define N_1 as the number of events which end with interface crossing and N as the total number of events, we get:

$$(16) \quad \frac{N_c}{N} = \frac{k_c}{k_c + k_b}$$

Using Equations 14-16, the rate constant of interface crossing can be expressed as:

$$(17) \quad k_c = \frac{N_c}{N \langle t \rangle}$$

Notice, that according to Equation 17, the rate constant of interface crossing, k_c can be calculated as the number of crossing events divided by the total waiting time at the interface.

The 15-min time interval between two consecutive time-lapse images is taken to be the experimental error for the waiting time.

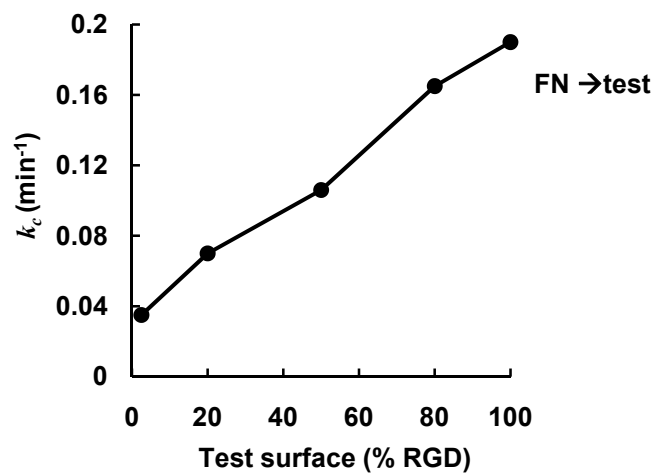


Figure A7. The rate constants of interface crossing from FN to test surfaces obtained from simulation. The ratio between crossing rates from 100% RGD to 100% RGD and 100% RGD to 2.5% RGD is also five fold, consistent with experimental observations (Table A1).

| | Simulation | Experiment |
|--|------------|------------|
| Surface composition (the line represents the wound edge at time t=0) | FN RGD | FN RGD |
| Wound closure rate ($\mu\text{m/h}$) (100% RGD) | 9.4 | 9.6 |
| Wound closure rate ($\mu\text{m/h}$) (2.5% RGD) | 1.7 | 1.7 |
| Wound closure rate ratio (100% RGD/2.5% RGD) | 5.6 | 5.6 |
| Single cell speed ratio (100% RGD/2.5% RGD) | 1.9 | 1.4 |
| $P_{FN \rightarrow RGD}$ ratio (100% RGD/2.5% RGD) | 4.7 | 5.7 |

Table A1. Summary of the rates for 100% and 2.5% RGD surfaces.

References

1. D. A. Lauffenburger, *Cell* **84**, 359 (1996).
2. G. I. Bell, *Science* **200**, 618 (1978).
3. S. P. Palecek, A. F. Horwitz, D. A. Lauffenburger, *Ann. Biomed. Eng.* **27**, 219 (1999).
4. T. R. Weikl, M. Asfaw, H. Krobath, B. Rozycki, R. Lipowsky, *Soft Matter* **5**, 3213 (2009).
5. M. Prass, K. Jacobson, A. Mogilner, M. Radmacher, *J. Cell Biol.* **174**, 767 (2006).
6. A. Pierres, V. Monnet-Corti, A. M. Benoliel, P. Bongrand, *Trends in Cell Biol.* **19**, 428 (2009).
7. A. Zidovska, E. Sackmann, *Phys. Rev. Lett.* **96**, 048103 (2006).
8. C. M. Nelson, C. S. Chen, *FEBS Lett.* **514**, 238 (2002).
9. B. Alberts et al., *Molecular Biology of the Cell*. (Garland Science, 2008), pp. 637-655.
10. C. R. Kahn, E. Young, I. H. Lee, J. S. Rhim, *Invest. Ophthalmol. Vis. Sci.* **34**, 3429 (1993).
11. K. A. Fichthorn, W. H. Weinberg, *J. Chem. Phys.* **95**, 1090 (1991).
12. C. H. Kang, W. H. Weinberg, *Accts. Chem. Res.* **25**, 253 (1992).
13. B. C. Goodwin, *Temporal Organization in Cells: A Dynamic Theory of Cellular Control Processes*. (Academic Press, 1963), pp. 55-80.
14. D. A. Beysens, G. Forgacs, J. A. Glazier, *Proc. Natl. Acad. Sci. U.S.A.* **97**, 9467 (2000).
15. A. Neagu, K. Jakab, R. Jamison, G. Forgacs, *Phys. Rev. Lett.* **95**, 178104 (2005).
16. D. Drasdo, S. Hohme, *Phys. Biol.* **2**, 133 (2005).

3 ARTIFICIAL EXTRACELLULAR MATRIX PROTEINS FOR RAPID WOUND HEALING

Abstract

Short RGD sequences exhibit biological activity but their responses are often not identical to that of fibronectin. Longer fibronectin fragments are difficult to purify and hence limit their use as biomaterials. Here we employ a genetic strategy to incorporate full-length fibronectin domains into artificial extracellular matrix (aECM) materials. We show that these aECM proteins promoted rapid spreading of Rat-1 fibroblasts. In particular, the aECM protein containing full-length fibronectin 9 and 10 exhibited increased $\alpha_5\beta_1$ integrin binding affinity. The aECM proteins with full-length fibronectin domains also promoted rapid wound healing of Rat-1 fibroblasts *in vitro* by supporting cell migration and proliferation; a result of increased phosphorylation of FAK and ERK.

3.1 Introduction

The discovery of the Arg-Gly-Asp (RGD) sequence (1) has triggered the widespread use of RGD-functionalized materials for directing cell behavior (2). In studies of this kind, however, cell responses on RGD surfaces are never identical to those observed on fibronectin (3). An obvious strategy to improve biological activity in biomaterials is to expand the RGD domain to include neighboring domains. The PHSRN domain on the 9th type III domain of fibronectin for instance, has been found to act synergistically with the RGD domain on the neighboring 10th domain (4). Recombinant full-length fibronectin type III domains 8 through 11 have also been shown to enhance integrin binding in cell attachment (5-6). However, full-length fibronectin fragments are expensive to purify in large quantities and difficult to attach to synthetic surfaces without denaturation.

Here we use a genetic strategy to fabricate biomaterials bearing full-length fibronectin domains. Functional full-length fibronectin domains 9 and 10 were incorporated within artificial extracellular matrix (aECM) proteins. Each aECM protein consists of a central full-length cell-binding domain and flanking elastin-like domains (Figure 3.1). Lysine residues were interspersed within the elastin-like sequences to allow crosslinking and fabrication of viscoelastic materials with tunable moduli (7-8). For simplicity, each aECM protein will be referred to by its cell binding domains (CBD).

MMASMTGGQMGHHHHHHDDDDKLD[(VPGIG)₂VPGKG(VPGIG)₂]₆**CBD**[(VPGIG)₂VPGKG(VPGIG)₂]₆LE

| Encoded protein (s) | CBD amino acid sequence |
|---------------------|--|
| FN910 | FGLDSPTGIDFSDITANSFTVHWIAPRATITGYRIRH HPEHFSGRPREDRVPHSRNSITLTNLTPGTEYVSSI VALNGREESPLLIGQQSTVSDVPRDLEVVAATPTS LLISWDAPAVTVRYRITYGETGGNSPVQEFTVPG S <u>K</u> STATISGL <u>K</u> PGVDYTITVYAVTGRGDSPASS <u>K</u> PI SINYR |
| FN910m | FGLDSPTGIDFSDITANSFTVHWIAPRATITGYRIRH HPEHFSGRPREDRVPHSRNSITLTNLTPGTEYVSSI VALNGREESPLLIGQQSTVSDVPRDLEVVAATPTS LLISWDAPAVTVRYRITYGETGGNSPVQEFTVPG S <u>A</u> STATISGL <u>A</u> PGVDYTITVYAVTGRGDSPASS <u>A</u> PI SINYR |
| FN10m | VSDVPRDLEVVAATPTSLISWDAPAVTVRYRITY GETGGNSPVQEFTVPGS <u>A</u> STATISGL <u>A</u> PGVDYTITV YAVTGRGDSPASS <u>A</u> PI SINYR |
| RGDm | YAVTGRGDSPASS <u>A</u> PIA |

Figure 3.1 Amino acid sequences of the aECM proteins containing full length fibronectin domains. The general sequence of the aECM proteins is shown above. Each protein contains an N-terminal T7 tag, hexahistidine tag, enterokinase cleavage site, followed by six elastin-like repeats, a cell-binding domain (CBD) and six elastin-like repeats. The amino acid sequence of the CBD used for each encoded protein is as shown. The differences between FN910 and FN910m are highlighted in yellow. The letter “m” is used to denote cell-binding domains containing lysine-to-alanine mutations.

3.2 Materials and methods

Cells, antibodies, and reagents

Dulbecco's modified eagle medium (DMEM), fetal bovine serum (FBS), penicillin/streptomycin, 0.05% Trypsin/0.25% EDTA, and PBS were obtained from Invitrogen (Carlsbad, CA). Rat-1 fibroblasts were generous gifts from the Asthagiri laboratory at Caltech. Cells were maintained in growth media containing phenol-red, 10% fetal bovine serum (FBS) and 0.1% penicillin/streptomycin through passages 9 – 25. All experiments were performed in phenol-red-free and serum-free DMEM with 0.1% penicillin/streptomycin (SFM).

Restriction enzymes were obtained from New England Biolabs, NEB, Ipswich, MA. All ligations were performed using T4 DNA ligase (Roche Applied Science, 2.5 h, 25 °C). DNA was isolated using QIAprep Spin Miniprep Kits (Qiagen). DNA segments encoding various cell-binding domains were purchased from Genscript (Piscataway, NJ) or Integrated DNA Technologies (IDT, San Diego, CA). Cloning was performed using *E. coli* XL10-Gold cloning strain (Stratagene) and subsequently transformed into *E. coli* strain BL21 (DE3) pLysS host (Novagen, Madison, WI) for protein expression.

Anti-phospho-FAK and anti-ERK 1/2 were purchased from Invitrogen. All other antibodies, human $\alpha_5\beta_1$ integrin, human plasma fibronectin (FN), Hoechst 33342 dye, and TMB/E substrate were obtained from Chemicon (Temecula, CA). Bovine serum albumin (BSA) was obtained from Sigma. Bis[sulfosuccinimidyl] suberate (BS³) used for crosslinking aECM proteins was obtained from Pierce, Rockford, IL. The 5-bromo-2'-

deoxyuridine (BrdU) labeling kit was purchased from Roche Applied Science (Indianapolis, IN). Round coverslips (12mm diameter, No.1) were from Deckgläser, Germany. All Western blotting reagents were obtained from GE Healthcare (Piscataway, NJ).

Construction, expression, and purification of aECM proteins

Standard molecular biological techniques were used for DNA manipulations, bacterial growth, and electrophoresis. DNA encoding various cell-binding domains was ligated into the pET28aRW vector containing an N-terminal T7 tag, hexahistidine tag, and an enterokinase cleavage tag (9-11). All products were verified by restriction digestion and DNA sequencing (Laragen, Los Angeles, CA).

Expression was performed in a 10 L Bioflow 3000 fermentor (New Brunswick Scientific, Edison, NJ). Cells harboring appropriate aECM expression constructs were grown in Terrific Broth supplemented with 25 mg/ml kanamycin and 35 mg/ml chloramphenicol to an optical density at 600 nm (OD_{600}) of 6-8. Protein expression, under the control of a bacteriophage T7 promoter, was induced with the addition of 1 mM β -isopropyl thiogalactoside (IPTG, GoldBio, St Louis, MO) for 2 h. The cell pellet was harvested and resuspended in TEN buffer (10 mM Tris-HCl, 1 mM EDTA, 100 mM NaCl, pH 8) at 0.5 g/ml and purified by thermal cycling (7, 10). Briefly, cells were frozen at -20 °C and thawed with 10 μ g/ml Deoxyribonuclease I, 10 μ g/ml of Ribonuclease A, 50 μ g/ml of Phenylmethylsulfonyl fluoride (Sigma, St Louis, MO), and 5 mM $MgCl_2$ for 3 h at 37 °C. The solution was sonicated for 10 min using a Misonix Sonicator 3000

(Farmingdale, NY, 1/2 inch flat tip, level 7, 5 s on, 5 s off). Water was added to bring the total volume of the solution to 1.3 L, adjusted to pH 9 and stirred at 4 °C for 2 h. The solution was centrifuged at 27915g, 1 h, 4 °C and the supernatant was collected. The supernatant was adjusted to 1 M NaCl, warmed to 37 °C for 1 – 2 h with shaking, and again centrifuged at 27915g, 1 h, 37 °C. The resulting pellet was retained and re-suspended in distilled H₂O (100 mg/ml) at 4 °C overnight. This process was repeated twice, with centrifugation spins at 39750g for better separation. The protein solution after the third cycle was dialyzed at 4 °C for 3 days and lyophilized. Purified aECM proteins (1 mg/ml) were verified using SDS-PAGE (Figure B2). The yields obtained for each aECM protein from typical 10 L fermentations are shown in Table B1.

Preparation of spin-coated aECM films

Spin-coated aECM proteins were prepared as described previously (11). Glass coverslips were sonicated in a mixture of ethanol and KOH for 15 min and rinsed several times with distilled H₂O. Protein solutions were prepared by dissolving 15 mg of lyophilized of FN910 (or FN910m) in 150 µl of sterile distilled H₂O at 4 °C for 3 – 4 h. BS³ (2.0 mg) dissolved in 17 µl of sterile distilled H₂O was added to 150 µl of protein solution, mixed, and centrifuged to remove bubbles. The stoichiometric ratio of activated esters in BS³ to primary amines in the aECM proteins was roughly 1:1. A 14 µl volume of BS³-protein solution was then spin-coated on a 12 mm diameter round glass cover slip at 329g for 30 s at 4 °C. Protein films were stored overnight at 4 °C before use.

Cell spreading

Standard 24-well tissue culture plates were coated with aECM protein solutions (1 mg/ml) or FN (10 μ g/ml) overnight at 4 °C. Coverslips containing crosslinked aECM films were also mounted separately into the wells using sterile grease. Wells containing adsorbed proteins were rinsed with PBS and subsequently blocked with 500 μ l of 0.2 wt% heat-inactivated BSA solution at room temperature for 30 min. In each well, 4×10^4 cells were added to 1 ml of SFM and incubated at 37 °C under 5% CO₂/95% air. Images of five random positions in each well were acquired every 15 min for 1.5 h. The projected cell areas for 200 cells were measured using ImageJ for each condition at various times.

$\alpha_5\beta_1$ integrin binding assay (ELISA)

In ELISA binding assays, adsorbed aECM proteins were used instead of adsorbed integrins to eliminate high levels of non-specific adsorption of aECM to polystyrene during binding. Integrin binding conditions were as reported by Altroff et al. (5). Briefly, FN, BSA, and various aECM proteins were dissolved in 25 mM Tris-HCl, pH 7.4, 150 mM NaCl, 1 mM MnCl₂, 0.1 mM MnCl₂, and 0.1 mM CaCl₂ (EB) to obtain a final concentration of 0.1 μ M. Clear, flat-bottom 96-well plates (Greiner, VWR) were coated with 100 μ l of various protein solutions and left overnight at 4 °C. The plates were then washed once with EB containing 1% BSA and 0.1% Tween-20 (wash buffer), and blocked with 320 μ l of EB with 5% BSA at 37 °C for 30 min. At the same time, $\alpha_5\beta_1$ integrins were diluted in EB with 1% BSA to various concentrations. The wells were washed twice with 200 μ l of wash buffer and incubated with integrins for 2 h at 37 °C. The wells were again washed five times with wash buffer, and 50 μ l of mouse anti- $\alpha_5\beta_1$

(clone JBS5, 1:200 in EB with 1% BSA) was added to each well and incubated at room temperature for 1 h. Finally, wells were washed five times with wash buffer before adding 50 μ l of goat anti-mouse-HRP (AP124P, 1:5000 in EB with 1% BSA) at room temperature for 30 min. Finally, wells were again washed five times with wash buffer and developed with 100 μ l of TMB/E substrate (ES001) for 10 min at room temperature. The reaction was stopped by addition of 100 μ l of 1 N H₂SO₄, and absorbance at 450 nm was read immediately using a Safire plate reader (Tecan, San Jose, CA). Assays were performed in triplicate and non-specific binding in the BSA wells for each integrin concentration was subtracted from the total binding values. The dose response data from the assays were fitted to a non-linear regression sigmoidal curve fit using Origin v.8 (OriginLab, Northampton, MA). The apparent K_D's for various aECM proteins and FN were calculated. The molecular weights of fibronectin and $\alpha_5\beta_1$ integrin were assumed to be 250 kDa and 265 kDa, respectively.

Wound healing

Wound healing was performed as described in Chapter 2 (see Figure 2.2A). Proteins were adsorbed on cleaned glass coverslips at 4 °C for up to 1 week and air-dried before use. A thin block of PDMS was placed in the center of the glass and mounted into a 24-well plate using silicone glue. To aid cell adhesion, FN solution (500 μ l, 10 μ g/ml in PBS) was added to each well and incubated overnight at 4 °C. Subsequently, all wells were aspirated before seeding Rat-1 fibroblasts in growth media. Upon reaching confluence, the growth medium was replaced with SFM, and the cells were incubated for another 24 h to arrest growth at the G₀/G₁ phase through contact inhibition (12-13).

Subsequently, the PDMS block was removed, and cells were washed twice with SFM to remove cell debris. Finally, images of several spots on the wound edge were acquired (per protein surface) every 15 min for 72 h. Images were analyzed using ImageJ v1.37. The wound area was traced manually at various time points, t , and the wound edge displacement was calculated as follows:

$$\text{Wound edge displacement } (\mu\text{m}) = \frac{\text{Wound area (t = 0 h)} - \text{Wound area (t = t h)}}{\text{Length of wound}}.$$

Individual cell tracking

Cells at the edge of the wound sheet were tracked for 10 h from the start of wounding. Cell tracking was performed manually by tracking the centroids of each cell, using ImageJ with plug-in MTrackJ, developed by Meijering and coworkers (<http://www.bigr.nl/>). The average distance over time for all the tracked cells was fitted to a linear fit, and the slope was reported as the average speed. An average of 100 cells was tracked for each protein surface.

Quantification of cell proliferation using BrdU-labeling

Wounding healing experiments were performed as previously described for 24 h, after which the medium in each well was replaced with SFM containing 10 μM BrdU. Cells were incubated for another 24 h, during which cells entering S-phase could incorporate BrdU during DNA synthesis. Cells were then washed twice with pre-warmed PBS, and fixed in 70% ethanol/30% Glycine (pH 2) at $-20\text{ }^{\circ}\text{C}$ for 20 min. After washing with PBS twice, cells were incubated with 200 μl of anti-BrdU (100 μl anti-BrdU with 900 μl incubation buffer) for 30 min at $37\text{ }^{\circ}\text{C}$. Cells were again washed with PBS and

incubated with 1 μ l Hoechst 33342 and 200 μ l anti-mouse-FITC in PBS (1: 200) for 30 min at 37 °C. Finally, cells were washed twice with PBS and once with distilled H₂O before mounting with 1:1 PBS/glycerol. Cells labeled with BrdU whose locations in the cell sheet were within a distance of 350 μ m of the wound edge were counted. The percent BrdU-positive cells was taken to be the number of BrdU-labeled cells as a percentage of the total Hoescht-labeled cells.

Immunoblotting

Standard 10-cm tissue culture petri dishes were coated with 3 ml of FN (10 μ g/ml or 100 μ g/ml in PBS), BSA (2 mg/ml in PBS), or aECM proteins (1 mg/ml in PBS) for 2 – 3 days at 4 °C. Dishes were washed twice with pre-warmed PBS, and blocked with 2 ml of heat-inactivated BSA (2 mg/ml in PBS) for 30 min at room temperature. Dishes were rinsed again twice with pre-warmed PBS. Confluent Rat-1 fibroblasts were serum-starved for 24 h (12-13) to arrest cell growth and reduce signaling to background. Cells were then trypsinized and held in suspension in SFM for 45 min at 37 °C to further minimize contact-mediated signaling. Subsequently, 3 x 10⁴ cells/cm² were seeded into each well containing pre-coated proteins and allowed to adhere for 1 h at 37 °C 5% CO₂/95% air. Cells were placed on ice, washed twice with ice-cold PBS, and lysed in 300 μ l of Laemmli buffer (62.5 mM Tris-Cl, pH 6.8, 20% glycerol, 10% 2-mercaptoethanol and 4% SDS). The cell lysates were collected and centrifuged at 18000g, room temperature for 15 min. Equal amounts of proteins were boiled for 5 min and separated on 7% or 10% SDS-PAGE gels, transferred to nitrocellulose membranes, and blocked with TBST (20 mM Tris-Cl, pH 7.6, 0.9% NaCl, 0.1% Tween-20) with 5% BSA for 1 h

at room temperature. Membranes were incubated with antibodies against FAK, phosphorylated FAK (pY397; 1:1000), ERK 1/2, and phosphorylated ERK 1/2 (Thr202/Tyr204, Thr185/Tyr187; 1:1000) in TBST with 3% BSA overnight at 4 °C. After washing with TBST, secondary antibodies (horse-radish peroxidase-conjugated anti-rabbit or anti-mouse IgG; 1:5000 in TBST) were incubated for 1 h at room temperature. Blots were washed three times for 15 min with TBST and developed according to manufacturer's instructions using the ECL Plus™ kit (GE Healthcare) and subsequently visualized by Typhoon™ Trio (GE Healthcare). Protein band intensities were measured using ImageQuant TL v7.0 and phosphorylation levels normalized to total FAK or total ERK1/2.

Statistical analysis

The statistical significance of differences was estimated by analysis of variance followed by the Tukey test. Differences were taken to be significant at $P \leq 0.05$.

3.3 Results and discussion

The amino acid sequences of the aECM proteins were designed to accommodate the large cell binding domains from fibronectin. We also mutated lysine residues to alanines in the fibronectin cell-binding domains (CBD) to eliminate any crosslinking with the lysine residues in the elastin domains, which could preclude the accessibility of the cell-recognition region for integrin binding (Figure 3.1). Large-scale expression of these constructs yielded 500 mg to 2g of purified lyophilized products per 10L of cell culture

obtained using fermentation. The purity and molecular weight of the lyophilized proteins were verified by SDS-PAGE (Figure 3.2).

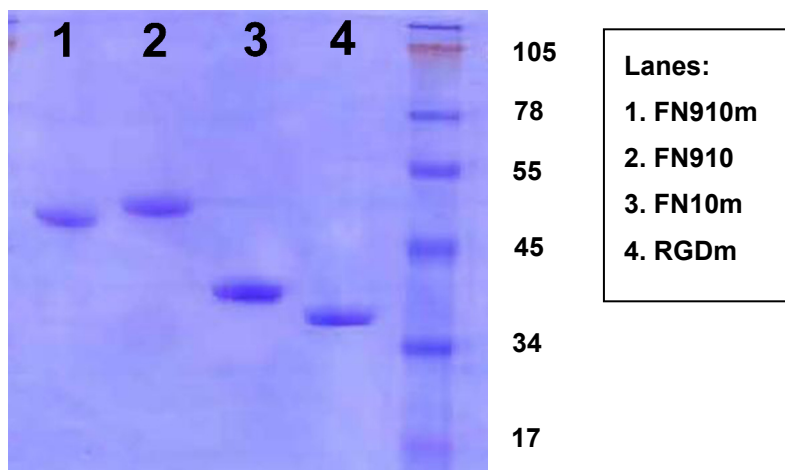
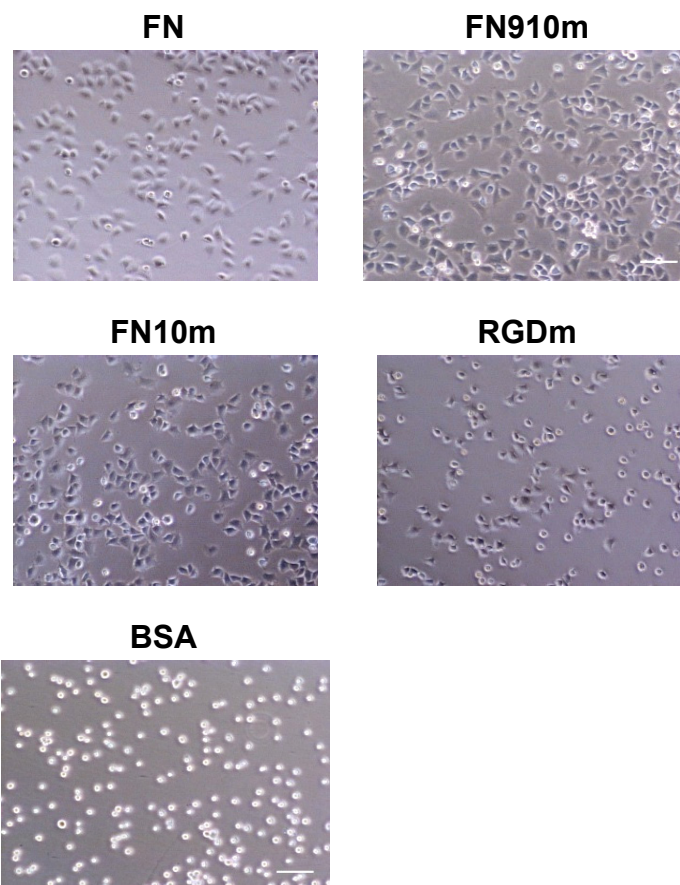


Figure 3.2 Coomassie SDS-PAGE gel of purified aECM proteins. 10 μ l of each denatured protein solution (1 mg/ml in PBS pH 7.4) was loaded for each lane and run with SeeBlue Plus2 molecular weight ladder.

Fibroblasts undergo rapid migration and proliferation during wound healing to replace cell loss following an injury (14). Fibroblasts express both the $\alpha_5\beta_1$ and $\alpha_v\beta_3$ integrins, which are utilized for cell spreading and wound healing (15-16). Here, Rat-1 fibroblasts were allowed to spread on both adsorbed and cross-linked aECM films. Cells spread faster on adsorbed FN910m and FN10m compared to RGDm surfaces (Figure 3.3A). After 1.5 h, cell areas on FN910m and FN10m were comparable to those on the positive control fibronectin (FN). In contrast, the average cell area on RGDm was two-fold lower (Figure 3.3B).

A



B

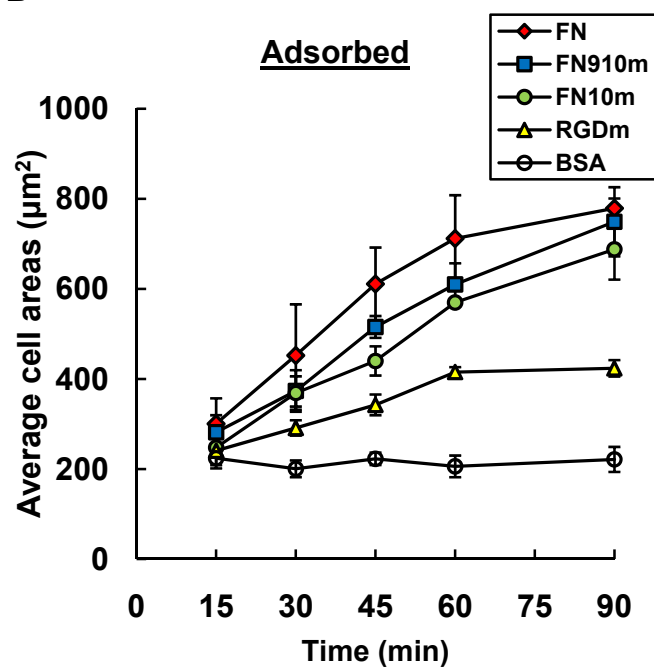


Figure 3.3 Time course of cell spreading of Rat-1 fibroblasts on adsorbed protein surfaces.

(A) Phase contrast images of spreading of Rat-1 fibroblasts on various adsorbed protein surfaces after 1.5 h. (B) The average projected cell areas for the adsorbed protein surfaces at each time point. Data represent means \pm SEM from three independent experiments. Scale bar represents 100 μm .

A similar trend was also observed on cross-linked aECM films (Figure 3.4A). There were also no differences in cell spreading behavior on cross-linked FN910 and FN910m, suggesting that the lysine-to-alanine mutations had no effect on the overall biological activity of the aECM proteins (Figure 3.4B).

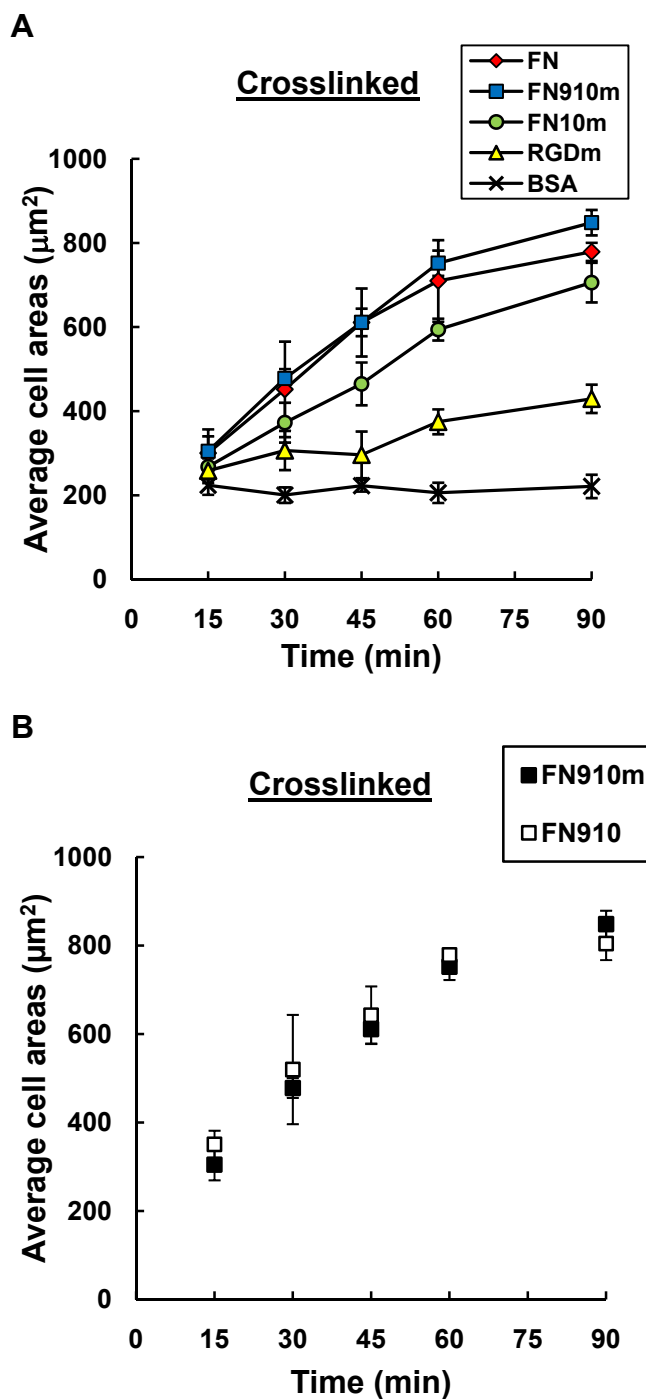
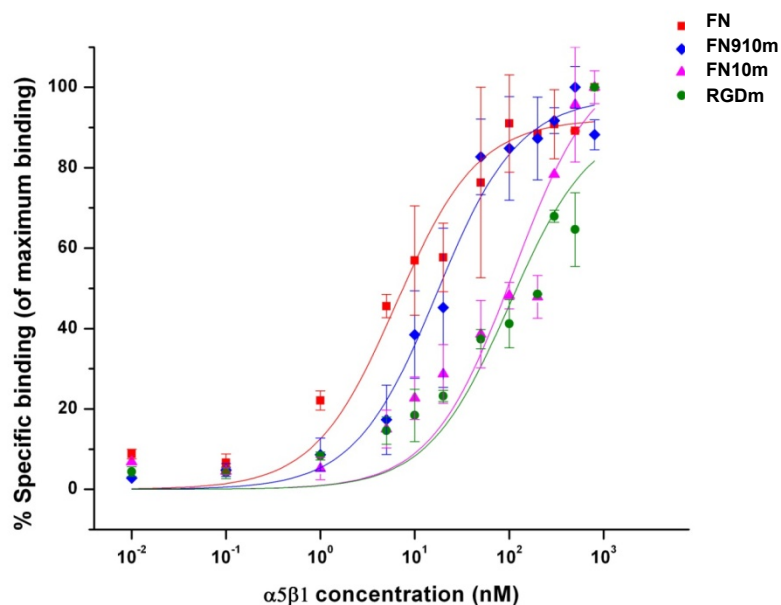


Figure 3.4 Time course of cell spreading for crosslinked aECM protein surfaces. (A) Cell spreading on spin-coated crosslinked FN910m, FN10m, and RGDm compared to adsorbed FN and BSA control surfaces. (B) Rat-1 cell spreading on spin-coated crosslinked FN910 and FN910m

Fibroblasts have been shown to spread faster on surfaces that promote specific $\alpha_5\beta_1$ integrin binding (17). To see if aECM proteins containing full-length cell-binding domains promoted increased integrin binding, we used a modified solid-phase integrin binding assay (ELISA). Indeed, we found a 10-fold enhancement in $\alpha_5\beta_1$ integrin binding affinity for FN910m (17.2 nM), compared to FN10m (109 nM) and RGDm (100 nM). Under the same conditions, the $\alpha_5\beta_1$ binding affinity for FN was 6.2 nM (Figure 3.5). The values for FN910m were higher than reported K_D values of 2 – 4 nM (6, 18-19), but were most likely due to the way the integrins are presented (i.e., immobilized integrins versus soluble integrins). The increase in $\alpha_5\beta_1$ integrin binding affinity also confirmed the synergistic effect of PHSRN (6, 18), suggesting that the full-length FN910 domains within the aECM proteins are indeed functional.

We did not see any significant differences in $\alpha_5\beta_1$ integrin binding affinities for FN10m and RGDm (Figure 3.5). However, FN10m promoted faster cell spreading than RGDm (Figure 3.3B and Figure 3.4A). A possible explanation for the increase in cell spreading rates on FN10m could be due to increased accessibility of the RGD loop with the increased structural stability of the full-length fibronectin 10 domain. Another possibility could be that FN10m promotes an increased binding affinity to the vitronectin receptor ($\alpha_v\beta_3$) integrin (20-21).



| | FN | FN910m | FN10m | RGDm |
|----------------|--------|---------|--------|--------|
| Apparent K_D | 6.3 nM | 17.2 nM | 109 nM | 100 nM |

Figure 3.5 Binding of $\alpha_5\beta_1$ integrin to fibronectin and aECM proteins by ELISA. Individual dose-response curves for various surfaces were corrected for non-specific binding in the BSA wells. Results are normalized and expressed as percentages of maximum binding activity. The apparent K_D 's were derived by fitting the data to a non-linear regression sigmoidal curve fit for each surface.

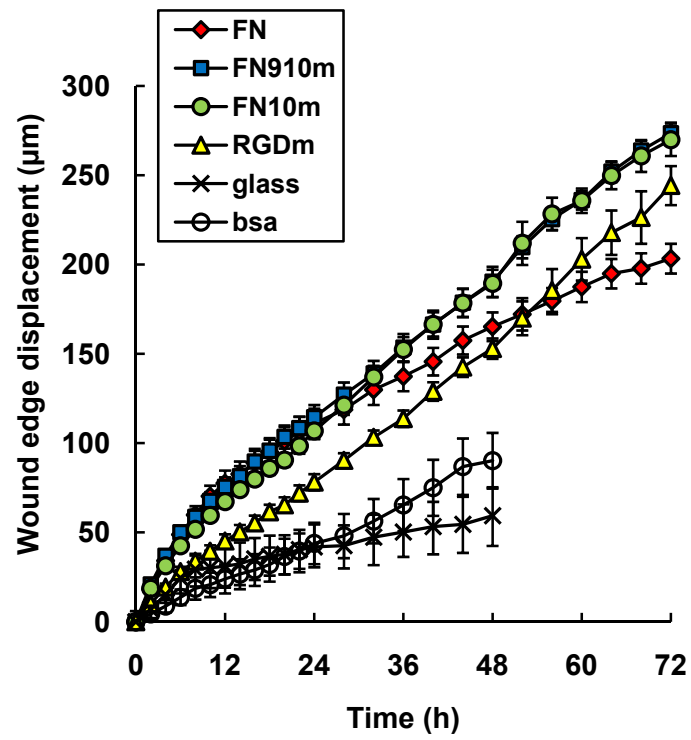
Given the faster cell spreading on the aECM proteins with full-length cell-binding domains, we next examined the ability of these proteins to promote wound healing using the wound healing assay developed in Chapter 2. Collective migration was observed on all adsorbed protein surfaces except on uncoated glass and BSA surfaces. Cells at the wound edge developed a polarized morphology after 2 h, extending their lamellipodia in

the direction of the wound (22). Cells consistently moved in the direction of the wound, and proliferation was observed after 24 h at the wound edge.

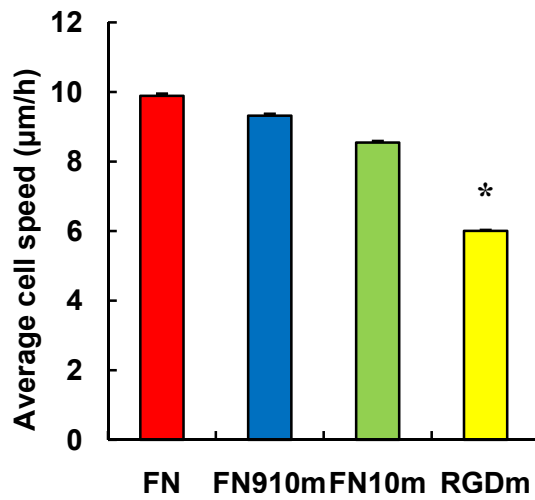
Figure 3.6A shows the wound edge displacement on various adsorbed protein surfaces over 72 h. In the first 24 h, cell sheets migrated with similar rates on FN, FN910m and FN10m surfaces. There were no significant differences between FN910m and FN10m; both surfaces supported faster migration than RGDm. Individual cells at the migrating wound edge were tracked for 10 h from the start of wounding. The average cell speeds are shown in Figure 3.6B. Cell speeds on FN910m ($9.2 \pm 0.8 \mu\text{m/h}$) and FN10m ($8.3 \pm 0.6 \mu\text{m/h}$) were comparable to that on FN ($9.4 \pm 0.8 \mu\text{m/h}$). On the other hand, cells migrated significantly slower on RGDm ($5.9 \pm 0.4 \mu\text{m/h}$; $P < 0.05$), accounting for the overall slower wound closure on RGDm.

The general wound healing behavior on aECM proteins with full-length fibronectin domains was also different than on FN after 24 h (Figure 3.6A). These differences could be accounted for by increased proliferation on FN910m and FN10m. Wounded Rat-1 monolayers were first allowed to migrate for 24 h in serum-free media and subsequently incubated with 50 μM of bromodeoxyuridine (BrdU) for another 24 h ($t = 24$ to 48 h). The number of BrdU-labeled cells is reported as a percentage of total Hoechst-positive cells in Figure 3.6C. The percentages of BrdU-labeled cells on the aECM proteins surfaces were significantly higher than that on FN, which would explain the slower wound healing behavior on FN at $t > 24$ h (Figure 3.6A).

A



B



C

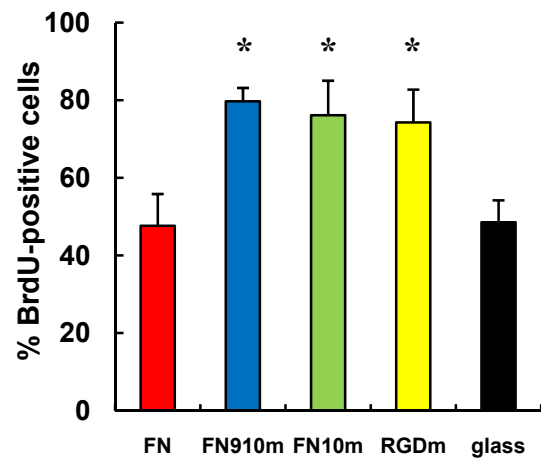
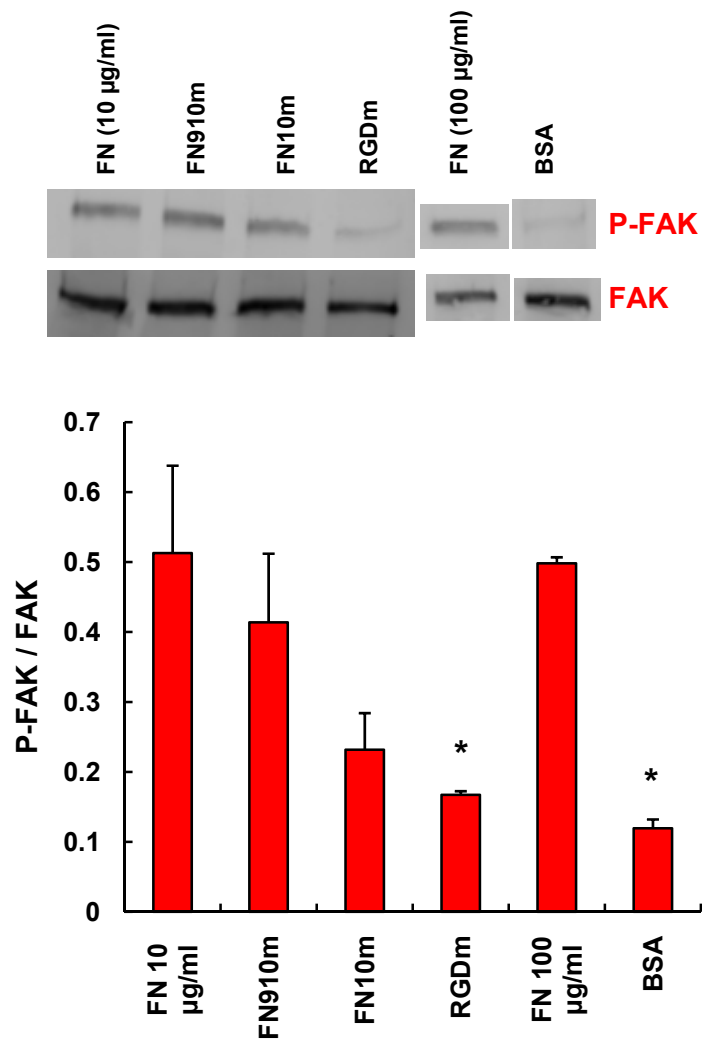


Figure 3.6 Quantification of wound healing behavior on adsorbed protein surfaces. (A) Rat-1 monolayers were wounded and allowed to migrate over various protein surfaces. The displacement of the wound edge as a function of time is shown. (B) Average speeds of cells migrating on various surfaces from $t = 0$ to 10 h. Individual cells in the first row of the wound edge were tracked for 10 h post wounding. Cell speeds are slopes from linear fit of distance over time data. Error bars are standard errors from fit. (C) The percentage of BrdU-positive cells for the period of $t = 24$ to 48 h (wounding; $t = 0$ h). The number of BrdU-labeled cells located in the cell sheet within 350 μm from the wound edge was represented as a percentage of the total number of Hoechst-positive cells in the same region. Data are means \pm SEM from five independent experiments for each surface. *, significant difference from FN surface ($P < 0.05$).

The difference in wound healing behavior on FN and aECM proteins is likely due to differences in cell signaling. To dissect these differences, we examined the key cell signaling pathways involved in wound healing. The focal adhesion kinase (FAK) is up-regulated during integrin-mediated signaling in cell migration (23), while the extracellular signal-regulated kinase (ERK) pathway is activated during cell proliferation (24-25). Figure 3.7 shows amounts of phosphorylated FAK and ERK represented as ratios of total FAK and ERK. We found high levels of P-FAK on FN, FN910m and FN10m, accounting for faster cell speeds measured on these surfaces (Figure 3.7A and Figure 3.6B).

Consistent with the BrdU data (Figure 3.6C), high levels of P-ERK were also found on all aECM protein surfaces (Figure 3.7B). The P-ERK/ ERK ratio was significantly lower on FN ($P < 0.05$), suggesting that the lower proliferation rate observed

on FN was due to low levels of ERK phosphorylation. To ensure that these observations were not due to low FN concentrations, we repeated these experiments with ten-fold higher FN concentrations (i.e., 100 $\mu\text{g/ml}$). As expected, the degree of phosphorylation for both FAK and ERK was unchanged.

A

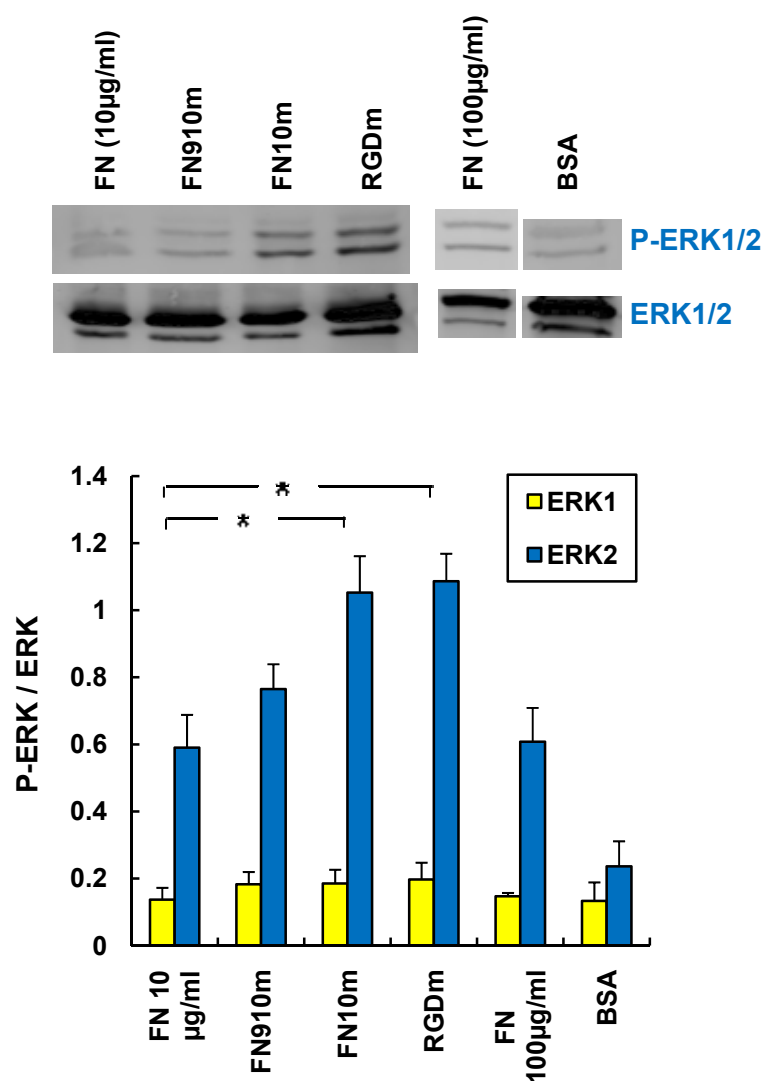
B

Figure 3.7 Determination of FAK and ERK phosphorylation in Rat-1 fibroblasts on adsorbed protein surfaces. (A, B) Rat-1 fibroblast cell sheets were serum-starved for 24 h, held in suspension in SFM for 45 min and allowed to attach onto protein-coated 10-cm petri dishes at 3.8×10^4 cells/cm². The cell lysates were analyzed by Western blotting with anti-FAK, anti-phosphoFAK (pY397), anti-phosphoERK1/2(p42/p44) and anti-total ERK1/2, antibodies. Band intensities were normalized to total-FAK or total-ERK bands. Reported data are means \pm s.d. for three independent experiments. *, significantly different from FN surface ($P < 0.05$)

3.4 Conclusions

In this work, we developed functional biomaterials incorporating full-length cell-binding domains. We showed that the artificial extracellular matrix proteins containing full-length fibronectin domains promoted rapid cell spreading of Rat-1 fibroblasts. The aECM protein containing full length fibronectin 9 and 10 was shown to bind the $\alpha_5\beta_1$ integrin with higher affinity, confirming the synergistic effect between the PHSRN and RGD cell binding domains. The aECM proteins containing full-length fibronectin domains 9 and 10 also promoted rapid wound healing *in vitro* by supporting cell migration and proliferation. The increase in cell migration speeds and proliferation observed on these surfaces was due to increased phosphorylation of FAK and ERK.

3.5 Acknowledgements

We thank Dr. Stacey Maskarinec and Dr. Shelly Tzlil for discussions. We acknowledge Dr. Anand Asthagiri for the Rat-1 fibroblasts and generous usage of fluorescence microscope. E. F. is supported by the Nanyang Overseas Scholarship, Singapore. This work is supported by NIH and by the NSF Center for Science and Engineering of Materials.

3.6 References

1. E. Ruoslahti, M. D. Pierschbacher, *Science* **238**, 491 (1987).
2. U. Hersel, C. Dahmen, H. Kessler, *Biomaterials* **24**, 4385 (2003).

3. H. B. Streeter, D. A. Rees, *J. Cell Biol.* **105**, 507 (1987).
4. S. Aota, M. Nomizu, K. M. Yamada, *J. Biol. Chem.* **269**, 24756 (1994).
5. H. Altroff et al., *J. Biol. Chem.* **276**, 38885 (2001).
6. H. Altroff, L. Choulier, H. J. Mardon, *J. Biol. Chem.* **278**, 491 (2003).
7. P. J. Nowatzki, D. A. Tirrell, *Biomaterials* **25**, 1261 (2003).
8. P. J. Nowatzki, C. Franck, S. A. Maskarinec, G. Ravichandran, D. A. Tirrell, *Macromolecules* **41**, 1839 (2008).
9. S. C. Heilshorn, K. A. Di Zio, E. R. Welsh, D. A. Tirrell, *Biomaterials* **24**, 4245 (2003).
10. J. C. Liu, S. C. Heilshorn, D. A. Tirrell, *Biomacromolecules* **5**, 497 (2003).
11. J. C. Liu, D. A. Tirrell, *Biomacromolecules* **9**, 2984 (2008).
12. C. Schorl, J. M. Sedivy, *Methods* **41**, 143 (2007).
13. W. A. Kues et al., *Biol. Reprod.* **62**, 412 (2000).
14. J. Gailit, R. A. F. Clark, *N. Engl. J. Med.* **2**, 738 (1999).
15. R. A. F. Clark, J. Q. An, D. Greiling, A. Khan, J. E. Schwarzbauer, *J. Invest. Dermatol.* **121**, 695 (2003).
16. J. Gailit, R. A. F. Clark, *J. Invest. Dermatol.* **106**, 102 (1996).
17. S. P. Massia, J. A. Hubbell, *J. Biomed. Mater. Res. A* **56**, 390 (2001).
18. R. P. Grant, C. Spitzfaden, H. Altroff, I. D. Campbell, *J. Biol. Chem.* **272**, 6159 (1997).
19. A. P. Mould et al., *J. Biol. Chem.* **272**, 17283 (1997).
20. T. A. Petrie, J. R. Capadona, C. D. Reyes, A. J. Garcia, *Biomaterials* **27**, 5459 (2006).
21. Y. Mao, J. E. Schwarzbauer, *Cell Comm. Adhesion* **13**, 267 (2006).
22. C. D. Nobes, A. Hall, *J. Cell Biol.* **144**, 1235 (1999).
23. D. J. Sieg et al., *Nat. Cell Biol.* **2**, 249 (2000).
24. L. Barberis et al., *J. Biol. Chem.* **275**, 36532 (2000).

25. H. R. Reiske, J. H. Zhao, D. C. Han, L. Ann Cooper, J. L. Guan, *FEBS Letters* **486**, 275 (2000).

4 EARLY PATTERNS IN WOUND HEALING

Abstract

The mechanisms by which cells move in a coordinated fashion have been studied intensively for decades. Current wound healing studies focus primarily on how cells migrate collectively within the cell sheet. However, how cells generate patterns and select one wound healing mechanism over the other has yet to be explored. The wound healing behavior of Madin-Darby Canine Kidney (MDCK) epithelial cells was examined *in vitro*, using circular wounds of increasing diameters. A unique wound healing pattern was observed on aECM surfaces: “leader cell groups” formed along the wound edge, separated by regions of actomyosin “purse strings”. This unique healing pattern was observed only on aECM surfaces, and not on glass. The spacing between consecutive leader cell groups was found to be independent of wound diameter. However, this spacing decreased with increasing concentrations of blebbistatin, a myosin II inhibitor. The wound healing behavior could be explained by a simple force transmission model. We verified experimentally that the selection of wound mechanism could be controlled by wound geometry. These results are consistent with the model predictions.

4.1 Introduction

How cells move together to heal a wound is fundamentally relevant to tissue repair, tumor progression, and developmental biology. Recent experiments have identified two distinct healing mechanisms (1). First, wound closure can occur via a “purse string” mechanism where cells use the motor protein myosin II to assemble actin filaments into a contractile bundle along the wound edge (2-3). The bundle contracts and generates mechanical forces, which can be transmitted continuously through intercellular adhesions along the wound edge (3-5). This draws the cell sheet into the wound area, thereby closing the gap (6-7). The second mechanism requires cells at the wound edge to extend their lamellipodia and pull the cells behind them as they migrate in the direction of the wound. Morphologically, they resemble “finger-like” protrusions and have been termed “leader cells” (8-9).

Current studies on wound healing have primarily focused on how cells create collective migration within the cell sheet (9-10). However, how cells select one mechanism over the other is still unclear. In this work, we attempted to address how cells select one healing mechanism over the other along the periphery of the wound.

We use an *in vitro* “barrier” wound healing assay, similar to that described in earlier chapters. To study wounds of controlled geometries and diameters, we used microfabrication to create micropatterned PDMS blocks to be used as barriers in the assay. The Madin-Darby Canine Kidney (MDCK) cell model was used because the MDCK cells display collective behavior and has shown both purse-string and lamellipodial crawling mechanisms in *in vitro* healing assays (11). We also examined

how MDCK cells responded to artificial extracellular matrix (aECM) proteins containing the full-length fibronectin 10 cell binding domain (Figure 4.1). This aECM protein has been shown to promote wound healing, similar to fibronectin *in vitro* in Chapter 3.

M MASMTGGQMG HHHHHH DDDDKLD[(VPGIG)₂VPGKG(VPGIG)₂]FN10m[(VPGIG)₂VPGKG(VPGIG)₂]₆LE

FN10m:

**VSDVPRDLEVVAATPTSLLISWDAPAVTVRYRITYGETGGNSPVQEFTVPGSASTATISGLAPGVDTITV
YAVTGRGDSPASSAPISINYR**

Figure 4.1 Amino acid sequence of aECM protein containing the fibronectin 10 domain

4.2 Materials and methods

Reagents

All reagents were purchased from Sigma-Aldrich unless otherwise specified. Phalloidin-rhodamine, mouse anti-T7 tag primary antibody, and goat anti-mouse FITC secondary antibody were obtained from Chemicon. The SU-8 3050 photoresist was obtained from MicroChem Corp (Newton, MA), silicon wafers were purchased from Wafer World, Inc. (West Palm Beach, FL), and polydimethylsiloxane (PDMS, Sylgard® 184) was from Dow Corning (Midland, MI). The tridecafluoro-1,1,2,2-tetrahydrooctyl-1-trichlorosilane was purchased from United Chemical Technologies, Inc. (Bristol, PA). Bis(sulfosuccinimidyl) suberate (BS³) was from Pierce (Rockford, IL). All cell culture reagents were obtained from Invitrogen (Carlsbad, CA). Fibronectin solution was from Chemicon.

Preparation of aECM substrates

Glass coverslips (No. 1, round, 25 mm diameter) were cleaned in KOH/ethanol solution for 30 min and incubated in 6N NaOH for 10 min. The treated coverslips were washed briefly in distilled H₂O and incubated in 2% 3-aminopropyltriethoxysilane/95% ethanol/H₂O solution for 2 min at room temperature. Subsequently, amine-functionalized glass coverslips were rinsed with methanol for 2 min and air-dried. The aECM protein containing the full-length FN10 domain was cloned, expressed, and purified as previously reported (see Figure 4.1). The aECM protein was dissolved in distilled H₂O (25 mg/ml) and crosslinked with bis(sulfosuccinimidyl) suberate (BS³, 100 mg/ml in distilled H₂O) at 4 °C. The protein mixture was pipetted onto amine-functionalized glass coverslips and spin-coated at 5000 rpm for 30 s at 4 °C. aECM protein films were dried overnight at 4 °C before use.

Cell culture

MDCK cells were generous gifts from Elowitz laboratory (Caltech). Cells were maintained in Dulbecco's modified eagle medium (DMEM) containing 10% fetal bovine serum, 1% penicillin/streptomycin, and phenol-red (growth medium). Cells from passages 10 to 30 were used with no observable differences in growth and cell morphologies. All experiments were performed in DMEM lacking phenol-red, supplemented with 1% penicillin/streptomycin (serum-free medium).

Microfabrication of micropatterned PDMS blocks

The wound features were designed using DesignCAD software and printed on transparencies as positive photomasks (CAD/Art Services, Inc., Bandon, OR) as shown in Figure 4.2. Standard photolithography techniques were used to fabricate mold features that were 50 μm high (12). Briefly, the SU-8 3050 photoresist was spin-coated on a silicon wafer at 3000 rpm, exposed to UV light through a photomask, and developed to form a “master” mold. We pre-coated the master with tridecafluoro-1,1,2,2-tetrahydrooctyl-1-trichlorosilane for 30 min under vacuum to facilitate subsequent removal of the cured PDMS. PDMS was mixed at 10:1 PDMS base/curing agent ratio, degassed for 15 min, poured over the master, and cured overnight at 80 °C. PDMS was peeled from the master, and cut into blocks for subsequent wound healing experiments. A sharpened blunt-end needle was used to punch holes through the blocks to allow injection of cells and media underneath the block.

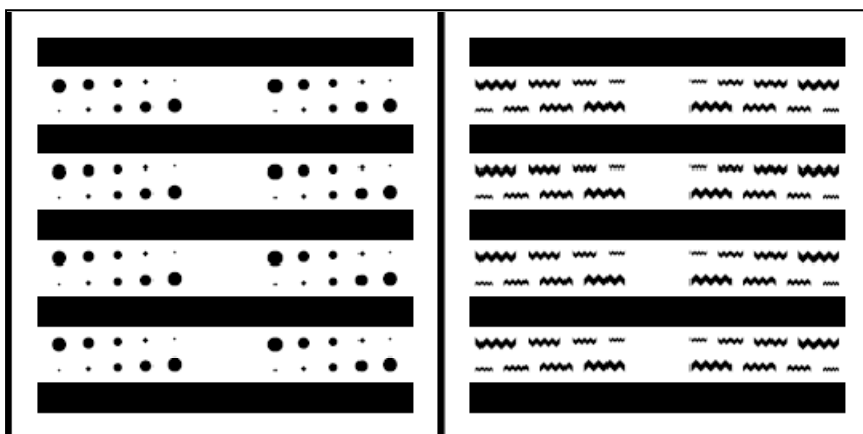


Figure 4.2 Design of micropatterned PDMS blocks for creating circular and zigzag-shaped wounds

Wound healing

The wound healing assay used in this chapter was modified from previous work (see Chapter 2, Figure 2.2A). PDMS blocks bearing the wound features (microposts) were cleaned with ethanol, air-dried, inverted, and pressed firmly onto a clean petri dish surface. To prevent non-specific adhesion of cells to the PDMS micropatterns, we pre-coated the walls of each PDMS block with 1 % Pluronic F-127 for 10 min at room temperature. The Pluronic was aspirated with a vacuum pump and the blocks were quickly dried with a jet of sterile air. At the same time, untreated glass coverslips or glass coverslips containing the spin-coated aECM films were mounted in 6-well tissue culture plates (BD Biosciences, CA) using silicone glue (GE healthcare, Piscataway, NJ). The Pluronic-treated PDMS blocks were pressed firmly onto the center of each coverslip. To allow cells to adhere to glass, fibronectin solution (10 $\mu\text{g/ml}$ in PBS) was incubated underneath the blocks overnight at 4 °C. The next day, MDCK cells were injected underneath the PDMS blocks and allowed to grow to confluence around the micropatterns. The PDMS blocks were subsequently removed, creating a wound of controlled shape. The wound healing process was observed using time lapse phase contrast microscopy (Figure 4.3).

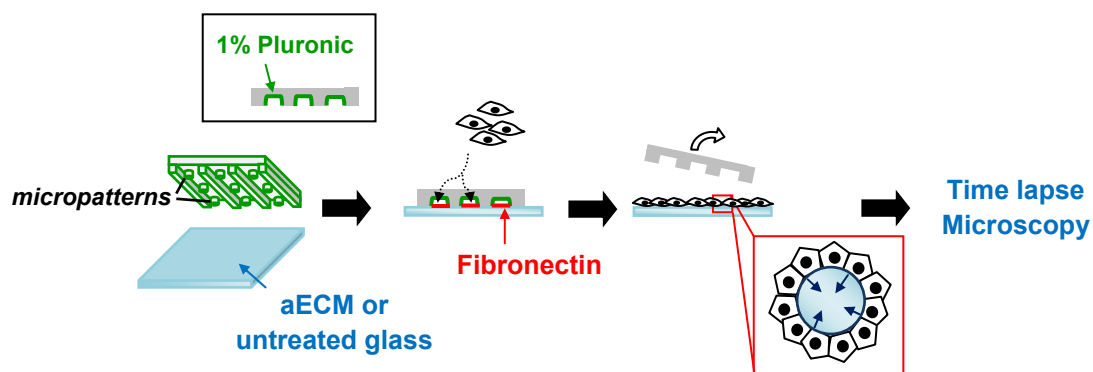


Figure 4.3 Schematic of wound healing assay. PDMS blocks were pre-treated with 1% pluronic and placed on either aECM or untreated glass substrates. Fibronectin was adsorbed underneath the stamps to aid cell adhesion. When MDCK cells were grown to confluence, the PDMS stamps were removed, revealing circular wounds previously occupied by the micro wound features. Wounded cell sheets were then observed using time lapse microscopy until wound closure.

Fluorescence imaging

The MDCK cell monolayers were wounded as described in Figure 4.3 and maintained in serum-free medium at 37 °C for 4 h. Cells were fixed with pre-warmed 3.7% paraformaldehyde in PBS at pH 7.5 for 20 min at 37 °C. After washing with PBS, cells were blocked in blocking solution (10% FCS, 5% sucrose, 2% BSA in PBS) for 30 min at room temperature. To visualize actin, cells were incubated with 100 μ l of rhodamine-phalloidin in 1 ml PBS (1:50 Molecular Probes, Inc., Eugene, OR) for 1 h at 37 °C. In order to detect the aECM protein, wounded monolayers migrating on aECM protein substrates were fixed, blocked, and incubated with a primary mouse anti-T7 tag antibody (1: 1000) in PBS for 2.5 h at 37 °C, followed by a secondary anti-mouse FITC

(1: 2000). Glass coverslips were mounted with 1:1 glycerol in PBS and imaged using an Zeiss Axiovert 200M microscope with epifluorescence optics and AxioVision LE software.

Myosin II inhibition studies

Cell monolayers were wounded and allowed to migrate on glass substrates in serum-free media containing various concentrations of (-) blebbistatin. Images of the wound area were acquired every 15 min for 24 h to obtain time-lapse videos.

Image analysis using MATLAB

To facilitate the analysis, we first outlined the wound edge using the properties of phase contrast and then identified leader cells by using the local geometry along the wound edge. The phase contrast effect enhanced the periphery of cell bodies along the wound edge. This allowed us to identify the edge of wound by comparing the intensity difference between neighboring pixels. The contour of the edge of the wound was iteratively smoothed using a nearest neighbor averaging method until the difference was less than a pre-set threshold. To identify the leader cell groups along the contour, we set three criteria. First, the leader cell group must be closer to the geometrical center of the wound than its neighboring points. Second, the local curvature around the leader cell group must be concave inward. Third, the migration of leader cell group must be moving toward the geometrical center of the wound. Once the leader cell groups were identified,

we tracked their speed of migration and separation distances along the edge of the wound. The number of leader cell groups and the spacing between them were calculated relative to the image at $t = 0$ h, and averaged for all frames. Since the program is limited to non-complicated contours, we limited our analysis to the first 4 h of each wound healing movie. Moreover, other factors such as cell-cell signaling have been shown to drive wound closure (13-14) at longer times (> 4 h).

4.3 Results and Discussion

We performed wound healing assays and allowed cell monolayers to migrate on aECM and glass substrates. To decouple from the effects of biochemical pathways, wound healing experiments were performed in the absence of serum and growth factors. In the same experiment, we also examined the effect of wound size by creating wounds of different diameters ranging from 300 to 500 μm . Under our wounding conditions, the aECM protein surface appeared intact after removal of the PDMS stamp. We further verified the integrity of the surface by labeling the N-terminal T7 tag of the aECM protein (Figure 4.4).

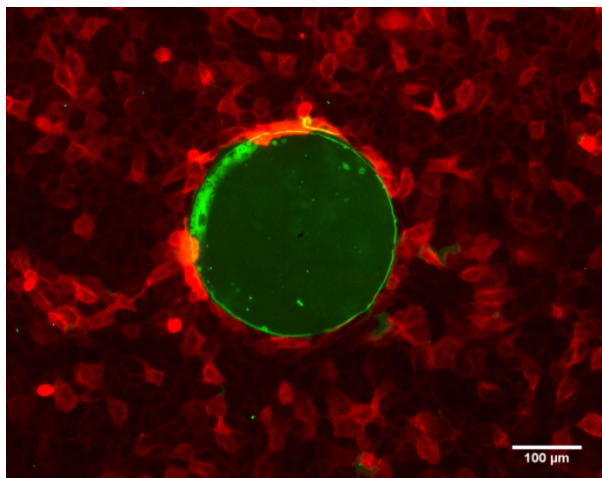


Figure 4.4 Removal of PDMS preserved aECM protein surface underneath. Cells were grown to confluence underneath the PDMS stamps. Following removal of the PDMS stamp, the cell sheets were immediately fixed and stained for F-actin (red) and the T7 tag (green). This confirmed that the original aECM protein substrate (green) was not affected by the PDMS micro wound features.

Wound closure on aECM protein substrates was generally complete by 10 h. On aECM surfaces, leader cells developed within 1 h after wounding, and these leader cells persisted until the entire wound area was closed (Fig 4.5, left panel). A striking pattern was observed on these substrates: leader cells appeared at regular intervals along the periphery of the wound. Figure 4.6A shows the presence of leader cells (white arrows) and purse strings (yellow triangles) in wounds stained for F-actin.

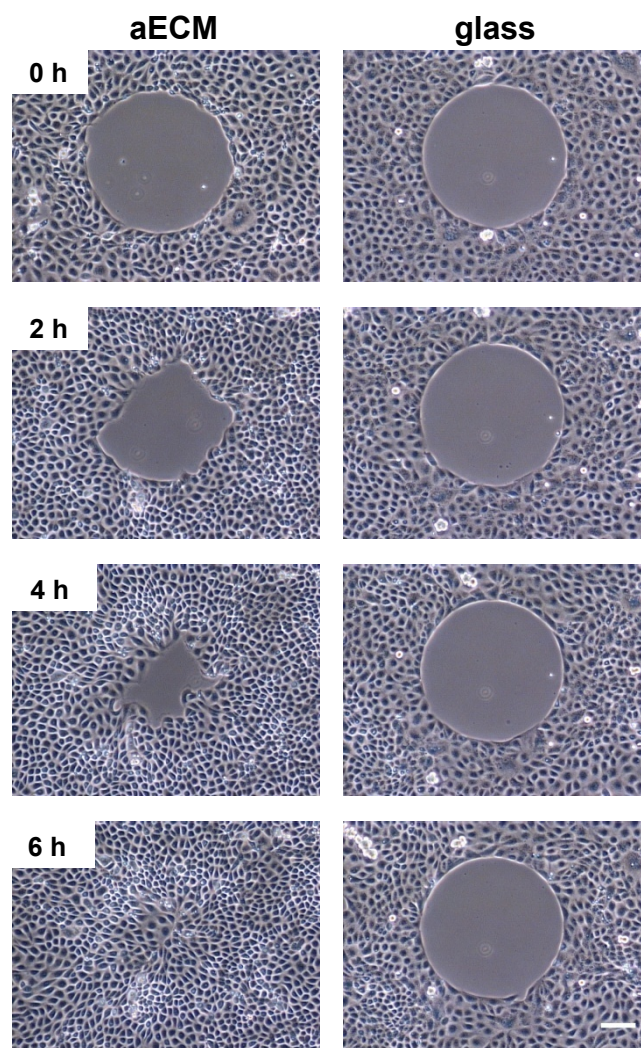


Figure 4.5 Time-lapse images of MDCK wound healing behavior on both aECM and untreated glass substrates. Time-lapse images show MDCK wound closure behavior on aECM (left panel) and on untreated glass (right panel) for a 400- μm -diameter circular wound. Scale bar represents 100 μm for all images.

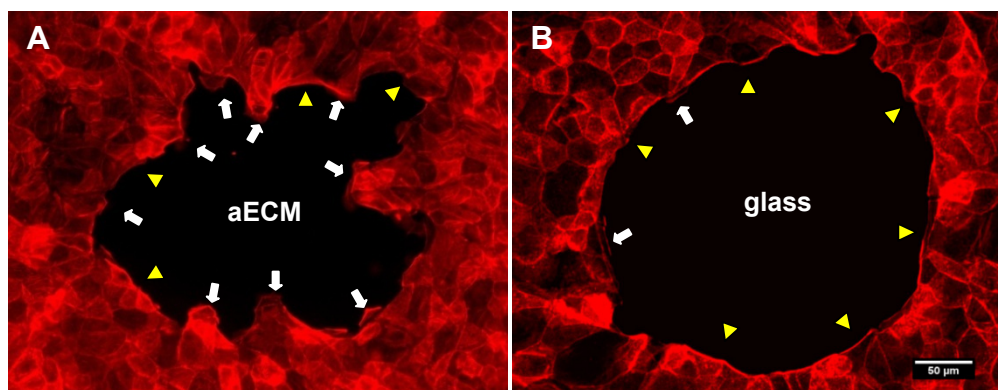


Figure 4.6 Verification of leader cells and purse-string structures. MDCK monolayers were wounded as described and allowed to heal on (A) aECM and (B) glass surfaces for 4 h. Cells were fixed and stained with phalloidin-rhodamine. White arrows indicate leader groups while yellow triangles indicate purse string structures. Scale bar represents 50 μm .

In the absence of ECM (i.e., on glass substrates), wound closure appeared to proceed largely by actomyosin contraction. The wound healing behavior was significantly slower and often led to incomplete wound closure even after 24 h (Fig 4.5, right panel). F-actin staining at 4 h after wounding confirmed the presence of actomyosin purse strings (yellow arrows) in these wounds (Figure 4.6B).

When we quantified the wound healing behaviors using MATLAB, we found that the number of leader cells increased with wound size on aECM surfaces but not on glass surfaces (Figure 4.7A). Although we observed one or two leader cells that developed spontaneously on glass, they moved with little persistence and retracted quickly (which accounted for the non-zero values for glass). The average spacing between consecutive leader groups, (L) was approximately 300 μm on aECM surfaces, independent of wound size (Figure 4.7B). Since no leader groups formed on glass surfaces, the spacing between

leader groups on glass was the entire length of the wound circumference (Figure 4.7B and inset).

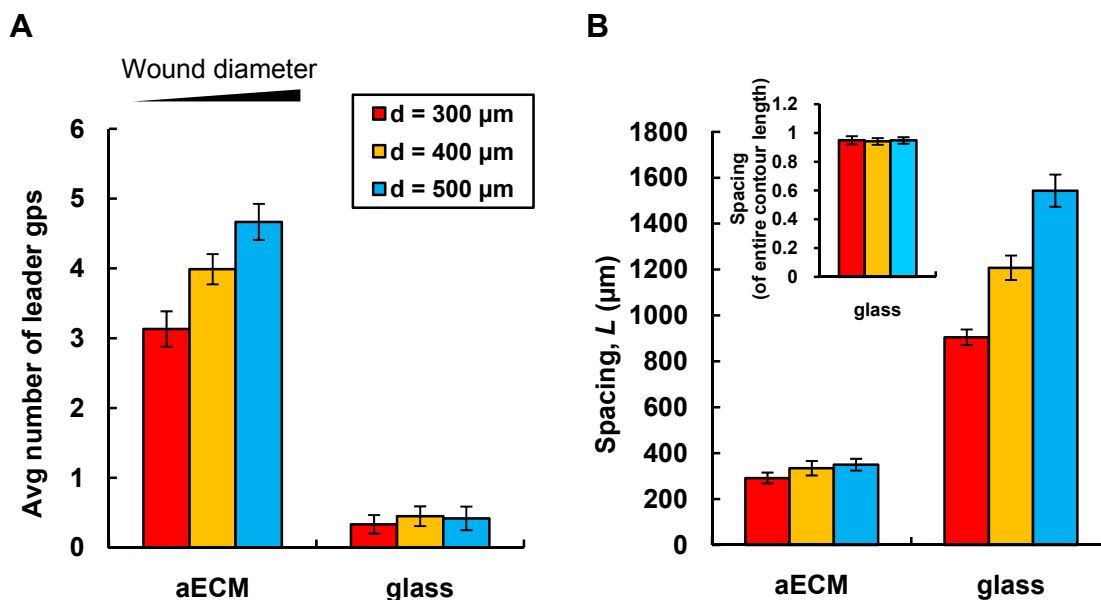


Figure 4.7 Quantification of wound healing behavior for circular wounds of increasing diameters. (A) The average number of leader groups as a function of wound size for aECM and glass. (B) The average spacing between these leader groups as a function of wound size. Inset represents the same data for glass as a fraction of total wound length. Error bars represent SEM.

To see if the spacing between leader cells was affected by decreasing the myosin II activity, we incubated wounded MDCK monolayers with blebbistatin, a known myosin II inhibitor (15). In blebbistatin-treated cultures, leader cells developed on glass substrates, resulting in patterns similar to those observed on aECM surfaces (Figure 4.8A). The average spacing between leader groups decreased with increasing blebbistatin concentrations (Figure 4.8B).

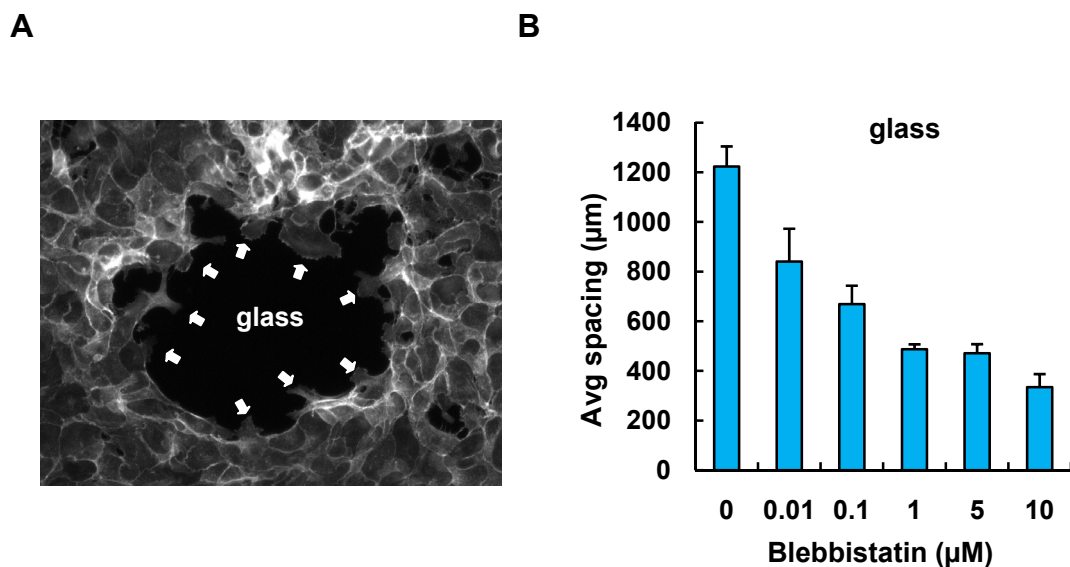


Figure 4.8 Effect of myosin inhibition on leader cell formation. (A) Wounded cell sheets were incubated in 5 μM blebbistatin and allowed to migrate over glass substrates. Cells were fixed and stained for F-actin. Arrows indicate leader groups. (B) The average spacing between leader groups decreases with increasing blebbistatin concentration. Error bars represent SEM.

From our experimental results, the selection of wound healing mechanism is dictated primarily by the presence of ECM in the wound area. The MDCK wound healing patterns observed on the aECM surfaces could be explained by a simple mechanical model. Figure 4.9 shows a schematic diagram of the proposed model. In the presence of ECM, leader cells develop at the wound edge and start to migrate into the wound. As they do so, they generate traction forces underneath the cell sheet (10). These forces are transmitted to neighboring cells through the adjacent actomyosin cable using the efficiency of myosin binding and unbinding (16-17). The increased tension inhibits the formation of additional leader cells in this region, resulting in regular spacing (L) between consecutive leader cells (see Figure 4.7B).

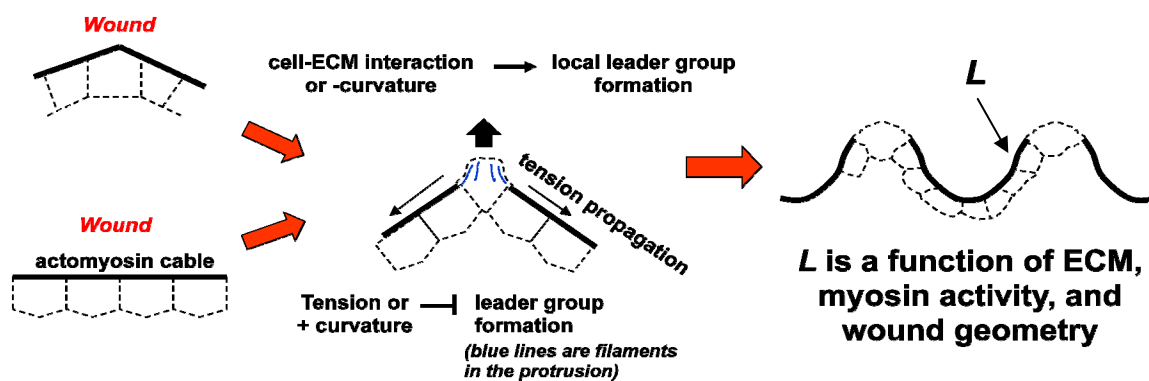



Figure 4.9 Schematic of proposed mechanical model. Model details and predictions can be found in the additional information section following this chapter.

The propagation of the tension through the actomyosin cables in our model depended on the activity of myosin II. Hence, increasing blebbistatin concentrations would increase the number leader cells formed (resulting in smaller spacing along the wound periphery). This argument is in line with our data obtained from the blebbistatin experiments (Figure 4.8). The model was further developed by Dr. Guo to yield predictions that were consistent with our experimental observations (see Figure B1 in the additional information for this chapter).

It is clear from our work and that of others (15), that cell-ECM interactions in the wound area provide the driving force for leader cell formation. Therefore, in the absence of ECM, cells rarely transform into leader cells. However, according to our model, we can also bias wound healing mechanisms by controlling wound geometry (Figure 4.9). To test this idea, we created zigzag-shaped wounds, and allowed MDCK cell monolayers to migrate on glass substrates. Indeed, 97.5% of the cells at apical regions (🏠) of the zigzag wound adopted leader cell morphologies after 2.5 h, while only 4.7 % of the cells

at the concave () regions became leaders (Figure 4.10A, B and E). Consequently, the leader cells also migrated on glass substrates even though cell-ECM interactions in the wound area were absent. This result is striking compared to a typical rectangular wound, where no leader cells were observed (and no advancement of the wound edge) was observed up to 24 h (Figure 4.10C, D and E).

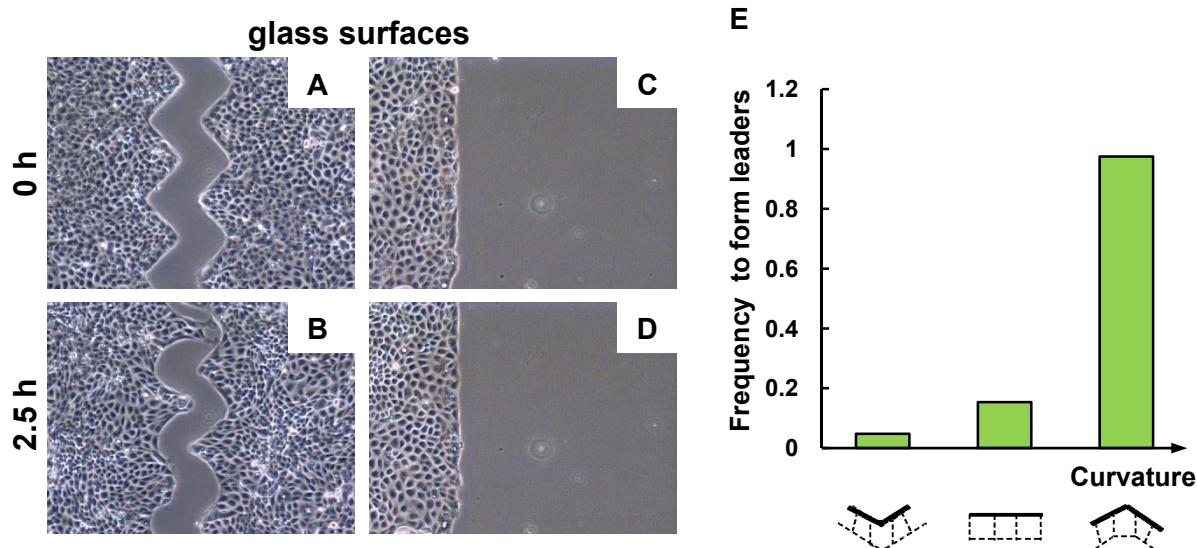




Figure 4.10 Wound curvature biases wound closure mechanisms. (A – D) show images of the wound edge at $t = 0$ h (A, C) and $t = 2.5$ h (B, D) migrating on glass substrates. Comparing (B) and (D), leader cells develop at apical regions () whereas purse-strings form in all concave regions () along the zig-zag wound edge. In contrast, in straight-edged wounds, no leader cell formation was observed up to 24 h. (E) The effect of wound curvature on the frequency of leader cell formation was observed up to 24 h. (E) The effect of wound curvature on the frequency of leader cell formation was observed up to 24 h. The frequency to form leaders was obtained by dividing the total number of leader cells by the total number of convex, straight, or concave regions.

4.4 Conclusions

In this work, MDCK wound healing behavior was examined on both aECM and glass surfaces. We observed leader cell formation on aECM surfaces, while wounds close primarily via actomyosin purse strings on glass surfaces. Wound healing on aECM surfaces exhibited a characteristic healing pattern, which consists of successive leader cells separated by regions of actomyosin purse strings. The average spacing between consecutive leader cell groups was constant for wounds of increasing diameter. However, this spacing decreased with increasing myosin II inhibition. We proposed a simple phenomenological model to provide a qualitative explanation of the wound healing pattern in the presence of ECM. We also verified by experiments that the selection of healing mechanisms could be controlled by wound geometry.

4.5 Acknowledgements

I would like to acknowledge Dr. Carson Yu, Dr. Ouyang Mingxing, and Dr. Woonhee Lee for help with the CAD design of the micropatterned PDMS stamps. I also thank Dr. Woonhee Lee and Amy Lam for training on the clean room apparatus.

4.6 References

1. P. Martin, J. Lewis, *Nat. Lett.* **360**, 179 (1992).
2. W. M. Bement, P. Forscher, M. S. Mooseker, *J. Cell Biol.* **121**, 565 (1993).
3. D. P. Kiehart, *Curr. Biol.* **9**, R602 (1999).

4. M. Tamada, T. D. Perez, W. J. Nelson, M. P. Sheetz, *J. Cell Biol.* **176**, 27 (2007).
5. Y. Danjo, I. K. Gipson, *J. Cell Sci.* **111**, 3323 (1998).
6. A. Jacinto, A. Martinez-Arias, P. Martin, *Nat. Cell Biol.* **3**, E117 (2001).
7. R. Fernandez-Gonzalez, J. A. Zallen, *Sci. Signal.* **2**, pe78 (2009).
8. T. Omelchenko, J. M. Vasiliev, I. M. Gelfand, H. H. Feder, E. M. Bonder, *Proc. Natl. Acad. Sci. USA* **100**, 10788 (2003).
9. M. Poujade et al., *Proc. Natl. Acad. Sci. USA* **104**, 15988 (2007).
10. X. Trepate et al., *Nat. Phys. Lett.* **5**, 426 (2009).
11. G. Fenteany, P. A. Janmey, T. P. Stossel, *Curr. Biol.* **10**, 831 (2000).
12. J. C. MacDonald et al., *Electrophoresis* **21**, 27 (2000).
13. Y. Matsubayashi et al., *Curr. Biol.* **14**, 731 (2004).
14. D. L. Nikolić, A. N. Boettiger, D. Bar-Sagi, J. D. Carbeck, S. Y. Shvartsman, *Am. J. Physiol. Cell Physiol.* **291**, 68 (2006).
15. S. Grasso, J. A. Hernandez, S. Chifflet, *Am. J. Physiol. Cell Physiol.* **293**, C1327 (2007).
16. A. Vaezi, C. Bauer, V. Vasioukhin, E. Fuchs, *Dev. Cell* **3**, 367 (2002).
17. R. S. Fischer, M. Gardel, X. Ma, R. S. Adelstein, C. M. Waterman, *Curr. Biol.* **19**, 260 (2009).

ADDITIONAL INFORMATION FOR CHAPTER 4

The mathematical model (Work of Dr. Chin-lin Guo)

We used the following reasoning and assumptions to construct the model. We modeled the dynamics of filament density f at the adhesion site because both cell protrusion and adhesion formation depend on f (1), while f self-amplifies itself by using existing filaments as templates to nucleate more filaments (2). Meanwhile, we modeled the formation of actomyosin bundle B and the dynamics of its tension T because T down-regulates f , and the formation of B depends on f (3). The self-amplification of f is local, whereas myosin facilitates the transmission of T along the actomyosin bundle over the entire cell periphery. This tension is further transmitted between neighboring cells at the wound edge. As a result, we can model all the cells at the wound edge as a single entity and expect that the dynamics of f and T form a feedback circuit to control the shape of wound during the healing process. In this work, we used the change in f to indicate the corresponding change of cell shape in the formation of leader cells (i.e., a higher value of f corresponds to a higher propensity to form a cell protrusion).

First, we consider that at the wound edge, cells develop two profiles of filament density f : cell protrusion can occur above a certain threshold, and no cell protrusion forms below this threshold. Since the formation of an actomyosin bundle requires filaments polymerized at the adhesion sites, cells with a lower level of f possess a lower level of tension. However, the tension within these cells is increased if they are neighboring to cells that form protrusions (i.e., with a higher level of f), because the tension can be transmitted between neighboring cells and cells with a higher level of f produce a strong

tension. The increment of tension within the non-protruding cells further inhibits their formation of protrusions. As a result, we expected to see interleaved protruding and non-protruding cells along the wound edge. This leads to the pattern formation of two healing mechanisms.

To model f and T , we first set N discrete points along the edge of the wound. For each of these points, we assigned an index $i = 1$ to N with the $(i - 1)^{\text{th}}$ point next to the i^{th} point and the $(N + 1)^{\text{th}}$ point referred to the first point. For the dynamics of f , we first assumed that the rate of filament formation depends on f (4), the local curvature κ (5), and the density of adhesions A which is a function of f and the concentration of ECM molecules, $[ECM]$ (1). Second, we assumed that the loss of f results from a tug-of-war between the tension from the actomyosin bundle, T , and the force generated by the motor clutch, F_{clutch} . Here we assumed that F_{clutch} depends on the myosin contractility m . We further assumed that the rate at which f decays is proportional to the ratio of T and F_{clutch} . In other words, a larger tension T results in a higher loss rate of f , whereas a stronger F_{clutch} allows for the accumulation of f and hence advances cell protrusion. Finally, we assumed that the accumulation of f at a point i increases its propensity to form a protrusion; this changes the membrane shape and in turn increases the chance to form more filaments at its neighboring points (5). Taken together, we have the equation for the dynamics of f at each point i, f_i ,

$$\begin{aligned} \frac{df_i}{dt} &= k_{poly} e^{\kappa} f_i A_i - k_{diss} \frac{T_i}{F_{clutch}} f_i + D_m (f_{i+1} + f_{i-1} - 2f_i) \\ &= k_{poly} \frac{[ECM]}{K_d + [ECM]} e^{\kappa} f_i^2 - k_{diss} \frac{T_i}{m} f_i + D_m (f_{i+1} + f_{i-1} - 2f_i) \end{aligned} \quad (3)$$

Here the first term indicates how adhesions and existing filaments f facilitate the polymerization of actin filaments, the second term indicates how the tug-of-war determines the rate of filament dissociation, and the third term indicates how the change of the membrane shape induced by neighboring points influences the filament formation with D_m as a coupling constant, where we approximated the shape effect by a term $(f_{i+1} + f_{i-1} - 2f_i)$ based on the assumption that the propensity to form a protrusion is proportional to f . In addition, we have used the approximation $A \sim f[ECM]/(K_d + [ECM])$ with K_d as the dissociation constant for ECM-integrin interaction, and used a term e^κ to mimic the curvature effect on the formation of actin filaments. In the present case, we found K_d is very small and the term $[ECM]/(K_d + [ECM])$ is saturated at even very low coating concentrations of ECM molecules. We set the rate at which f grows $\sim k_{poly}f e^\kappa A$ with k_{poly} as a constant. Likewise, we have approximated that $F_{clutch} \sim m$ and set the rate at which f decays $\sim k_{diss}T/F_{clutch}$ with k_{diss} as a constant.

For the dynamics of bundle tension T , we first assumed that the formation of the actomyosin bundle B depends on f and m , and the bundle generates the tension through a pairwise interaction. Second, we assumed that the dissembling of B and hence the dissipation of T depend on the curvature of the wound edge as well, in that curvatures that favor the formation of protrusions might enhance the dissembling of the actomyosin bundle (5). Third, we assumed that m facilitates the transmission of T between neighboring points (3). Taken together, we have the equation for the dynamics of T ,

$$\begin{aligned} \frac{dT_i}{dt} &= k_T B_i^2 - k_{dissip} e^\kappa T_i + m D_T [(T_{i+1} - T_i) + (T_{i-1} - T_i)] \\ &= k_T m^2 f_i^2 - k_{dissip} e^\kappa T_i + m D_T (T_{i+1} + T_{i-1} - 2T_i) \end{aligned} \quad (4)$$

Here the first term indicates how myosin and existing filaments f facilitate the assembly of the bundle B which in turn generates the tension through a pairwise interaction, the second term indicates the dissipation of the tension at a rate of $k_{dissip}e^\kappa$ with k_{dissip} as a constant, and the third term indicates the transmission of the tension between neighboring points in a myosin-dependent manner with D_T as a constant. To obtain Equation 4, we have approximated $B \sim fm$ and set the rate at which T is created $\sim k_T B^2$ with k_T as a constant. Likewise, we have implemented myosin contractility m into the transmission efficiency of T between neighboring points. We did not express the tension T in a vector form because the directionality of the tension is balanced with intracellular pressure. For simplicity, the force balance within and between the cells were also ignored.

Next, we took the continuous limit by setting $N \rightarrow \infty$. We set l as the spacing between neighboring points and x as the coordinate along the periphery of a single cell or a single cell cluster. These allow us to rewrite Equations 3 and 4 to yield

$$\frac{df}{dt} = k_{poly} \frac{[ECM]}{K_d + [ECM]} e^\kappa f^2 - k_{diss} \frac{T}{m} f + D_m l^2 \frac{d^2 f}{dx^2} \quad (5)$$

and

$$\frac{dT}{dt} = k_T m^2 f^2 - k_{dissip} e^\kappa T + m D_T l^2 \frac{d^2 T}{dx^2}. \quad (6)$$

The continuous limit approach transformed our model into a reaction-diffusion scheme. Equations 5 and 6 were simplified by rescaling variables and grouping

parameters. By setting $u = (k_{diss}k_{Tm}/k_{dissip}^2 e^{2\kappa} r[MLCK]_0)^{1/2} f$, $v = (k_{diss}/k_{dissip} e^{\kappa} m) T$, $\tau = k_{dissip} e^{\kappa} t$, $z = (k_{dissip} e^{\kappa} / D_m l^2)^{1/2} x$, $m' = m D_p / D_m$, and $\kappa' = \kappa + 1/2 \log(D_p / k_{diss} k_{poly} D_m)$, we have

$$\frac{du}{d\tau} = \alpha u^2 - vu + \frac{d^2 u}{dz^2}, \text{ and} \quad (7)$$

$$\frac{dv}{d\tau} = u^2 - v + D \frac{d^2 v}{dz^2}, \quad (8)$$

where

$$\alpha = \frac{[ECM]}{K_d + [ECM]} \times \frac{e^{\kappa'}}{\sqrt{m'}}$$

as shown in Equation 1 is an effective “strength” to stimulate the accumulation of filaments and hence the formation of leader cell groups, and

$$D = m'$$

as shown in Equation 2 is an effective “diffusivity” to transmit the retraction tension and inhibit the formation of leader cells groups.

Model analysis

Equations 7 and 8 possess the same reaction-diffusion scheme as in the Turing model (6). Thus, we used the standard approach for Turing model (6) to obtain the analytical results. To proceed, we set $F(u, v) = \alpha u^2 - vu$ and $G(u, v) = u^2 - v$. According to reference (6), the system can form spatially inhomogeneous patterns only if a) in the

absence of diffusion there are at least one stable and non-zero steady-state solution, and b) in the presence of diffusion the stable steady-state solution becomes unstable, allowing the system to evolve from a spatially homogeneous state to a spatially inhomogeneous state, which in turn forms the morphological pattern. We examined the stability of the solution by performing the linear stability analysis; that is, allowing small perturbations of u and v away from their homogeneous steady-state solutions and using Fourier transform to identify the growth or decay rates of various modes parameterized by their wave number k . The mode with the dominant growth rate in turn determines the pattern (6).

We assumed (u_s, v_s) as the stable, non-zero, and spatially homogeneous steady-state solution in Equations 7 and 8. (u_s, v_s) satisfies $F(u_s, v_s) = G(u_s, v_s) = 0$, which leads to $u_s = \alpha$ and $v_s = \alpha^2$. To examine the stability of u_s and the corresponding pattern formation in Equations 7 and 8, we allowed small perturbations of u and v away from their homogeneous steady-state solutions, $u = u_s + \delta u$ and $v = v_s + \delta v$, and performed Fourier transform on δu and δv by setting $\delta u = \sum_{k=-\infty}^{\infty} A_k \exp(\lambda_k \tau + ikz)$ and $\delta v = \sum_{k=-\infty}^{\infty} B_k \exp(\lambda_k \tau + ikz)$, where k is the wave number, A_k and B_k are the magnitudes for each mode, λ_k is the growth or decay rate (depending on the sign), and $i = (-1)^{1/2}$ is the imaginary number. These lead to

$$(\lambda_k - F_u + k^2)A_k = F_v B_k, \text{ and} \quad (9)$$

$$(\lambda_k - G_v + Dk^2)B_k = G_u A_k, \quad (10)$$

where

$$\begin{aligned}
F_u &= \left. \frac{\partial F(u, v)}{\partial u} \right|_{u=u_s, v=v_s} = 2\alpha u_s - v_s = \alpha^2 \\
F_v &= \left. \frac{\partial F(u, v)}{\partial v} \right|_{u=u_s, v=v_s} = -u_s = -\alpha \\
G_u &= \left. \frac{\partial G(u, v)}{\partial u} \right|_{u=u_s, v=v_s} = 2u_s = 2\alpha \\
G_v &= \left. \frac{\partial G(u, v)}{\partial v} \right|_{u=u_s, v=v_s} = -1
\end{aligned} \tag{11}$$

Multiplying Equations 9 and 10 from both sides to eliminate A_k and B_k (assuming that A_k and B_k both are non-zero), we have

$$\lambda_k^2 + [(D+1)k^2 - (F_u + G_v)]\lambda_k + Dk^4 - (DF_u + G_v)k^2 + (F_u G_v - F_v G_u) = 0. \tag{12}$$

Equation 12 indicates that in the absence of diffusion term (i.e., $k = 0$), the steady-state solution (u_s, v_s) is stable only if there is no real and positive solution of λ_k ; this requires $(F_u + G_v) < 0$ and $(F_u G_v - F_v G_u) > 0$, which requires $\alpha < 1$. Meanwhile, to have an unstable steady-state solution in the presence of diffusion, from Equation 12 we found that the term $Dk^4 - (DF_u + G_v)k^2 + (F_u G_v - F_v G_u) < 0$ is necessary, which occurs only if $(DF_u + G_v) \geq 0$ and $(DF_u + G_v)^2 \geq 4D(F_u G_v - F_v G_u)$. Taken together, these requirements confine a region in the parameter space,

$$\frac{\sqrt{2}+1}{\sqrt{D}} \leq \alpha < 1 \tag{13}$$

where cells or cell clusters can form non-random and non-uniform patterns.

From Equations 1 and 2, $\alpha = e^{\kappa} [ECM] / m'^{1/2} (K_d + [ECM])$ and $D = m'$. Thus, Equation 13 indicates the range of the wound curvature and ECM molecule coating concentrations for the pattern formation of alternative healing mechanisms around the wound edge at a given myosin contractility m' . Inside the confined region the wound edge can form patterns. Outside the region, the healing is completely controlled by either the purse-string or leader cells. With these requirements, we can obtain the modes with real and positive λ_k , among which the dominant mode (i.e., the mode with largest growth rate) is the one satisfying $\partial \lambda_k / \partial k = 0$. From Equation 12, the wave number of the dominant mode, k_{dom} , obeys

$$D[(D-1)k_{dom}^2 + F_u - G_v]^2 + (D+1)^2 F_v G_u = 0. \quad (14)$$

The mode of the dominant pattern can be expressed as $k_{dom} = 2n\pi/Z$ where n is an integer and Z is the periphery length of the wound. Thus, n defines the number of leader cell groups. For example, $n = 2$ represents the case where there are two separated leader cell groups along the wound edge.

Using Equation 11 and the relation $D = m'$, we rewrote Equation 14 for the mode with a wave number $k = 2n\pi/Z$ (n indicates the number of leader cell groups) as

$$n^2 = \left(\frac{Z}{2\pi}\right)^2 \frac{(m'+1) \sqrt{\frac{2}{m'} \alpha - \alpha^2 - 1}}{m'-1}. \quad (15)$$

Thus, for a given n , we can solve α numerically. Using graphical method, we found that smaller α leads to smaller n in Equation 15. For a fixed size of wound, this suggests that the absence of ECM molecules leads to a larger spacing between leader cell groups

(Figure B1a). At the same time, Equation 15 suggests that a smaller myosin contractility m' leads to a larger n (Figure B1b).

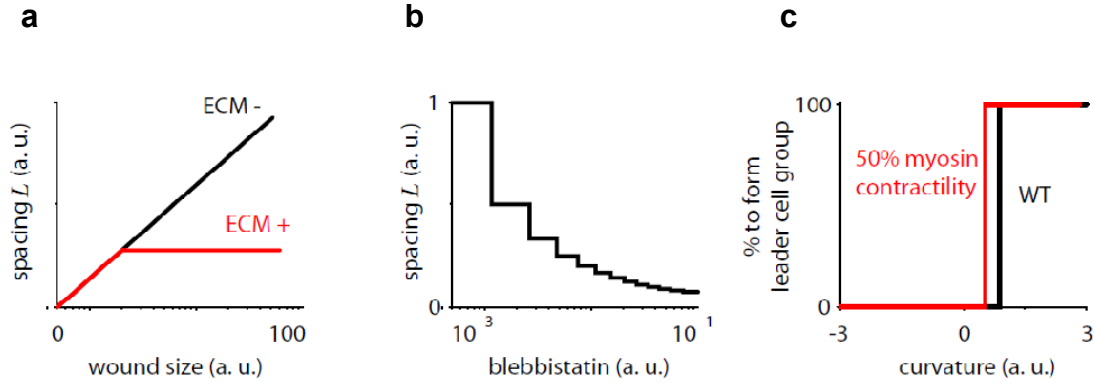


Figure B1 Model predictions. (a) The average spacing, L between consecutive leader cell groups as a function of wound size in the presence and absence of ECM. (b) The average spacing, L between leader cell groups as a function of increasing blebbistatin concentration. (c) Percent leader cell group formation as a function of wound curvature.

Parameters in Figure B1

To obtain Figure B1, we used the following parameters. For the change of spacing upon the treatment of blebbistatin, we set $(2\pi/Z)^2 = 0.003$ in Equation 15, the dose of blebbistatin = $1/m'$, and $[ECM]e^{K_2}/(K_d + [ECM]) = 8$ in Equation 1. We also used the reverse of n , $1/n$, to represent the spacing in Figure B1. To obtain the propensity of leader cell group formation on the change of the curvature, we identified the minimal α in Equation 1 which allows for an unstable non-zero steady-state solution in the absence of

diffusion term. This occurs at $\alpha = 1$ as shown in Equation 13. Then, we set $[ECM]/[(K_d + [ECM])(m')^{1/2}] = 1$ in Equation 1 to obtain the corresponding κ^2 .

References

1. M. Bailly, *Trends Cell Biol.* **13**, 163 (2003).
2. A. Upadhyaya, A. van Oudenaarden, *Curr. Biol.* **14**, R467 (2004).
3. A. Vaezi, C. Bauer, V. Vasioukhin, E. Fuchs, *Dev. Cell* **3**, 367 (2002).
4. L. G. Smith, R. Li, *Curr. Biol.* **14**, R109 (2004).
5. A. P. Liu et al., *Nat. Phys. Lett.* **4**, 789 (2008).
6. J. D. Murray, *Mathematical Biology*. S. A. Levin, Ed., Biomathematics, vol. 19, (Springer, New York, second ed., 1991), pp. 372 – 424.

5 HARNESSING THE PURSE STRING FOR ACCELERATED WOUND CLOSURE

Abstract

Wound healing is essential in maintaining tissue integrity. Wounds can close via lamellipodial crawling, which involves the rapid migration of cell sheets. A slower mechanism also exists, which involves the assembly of an actomyosin cable and subsequent contraction in a “purse string” manner to close the wound. Here we vary wound geometry to generate conditions where both mechanisms act synergistically to accelerate wound closure. In wounds that take the shape of zigzag patterns, cells at the apical points develop into leader cells while the cell sheet undergoes purse string contraction in concave regions. Especially strong purse string contraction was observed in 45° zigzag wounds, resulting in nearly eight-fold faster wound healing rates compared to wounds with straight edges.

5.1 Introduction

The process of collective migration has been well-studied for its importance in wound healing, morphogenesis, and tumor metastasis. In tissue repair, wound closure can occur via two distinct mechanisms (1). Using cell-ECM interactions, cells at the wound edge can actively extend their lamellipodia as they migrate into the wound area (2-3). These leader cells guide the cells behind them, forming “finger-like” protrusions. Wound closure can also occur via a “purse string” mechanism using a continuous actomyosin cable that develops along the periphery of the wound (4-5). As the cable contracts, the mechanical force it generates can be transmitted through intercellular adhesions along the wound edge (6-8).

There are numerous strategies to influence cell migration, which include controlling surface adhesiveness (9), substrate stiffness (10), and micropatterning (11). We present here a novel strategy to influence cell sheet migration in wound healing in the absence of ECM. We pre-dispose wounds to a zigzag geometry and create conditions where both the lamellipodial crawling and purse string mechanisms can act synergistically to accelerate wound closure.

Although the selection of wound healing mechanism has been reported to be independent of wound shape (12), we report here configurations that strongly bias the selection of wound healing mechanisms based on local geometry. Whitesides and coworkers demonstrate that cells confined to a square shape are likely to form lamellipodia at corners (13). Likewise, in zigzag wounds, cells located at the apex have a high propensity to develop into leader cells. Conversely, cells confined to concave

regions are likely to undergo purse string contractions. Local geometry at the apex induced the formation of leader cells, but on glass surfaces, cells were unable to migrate into the wound area. The traction forces generated by the leader cells however, generate tension in the adjacent actomyosin cables. The tension reinforces purse string contraction in the neighboring regions and drives the cell sheet forward. We further hypothesize that the propensity for leader cell formation increases with decreasing angle θ at the apex, and that the resulting contractile forces will increase with decreasing angle (Figure 5.1).

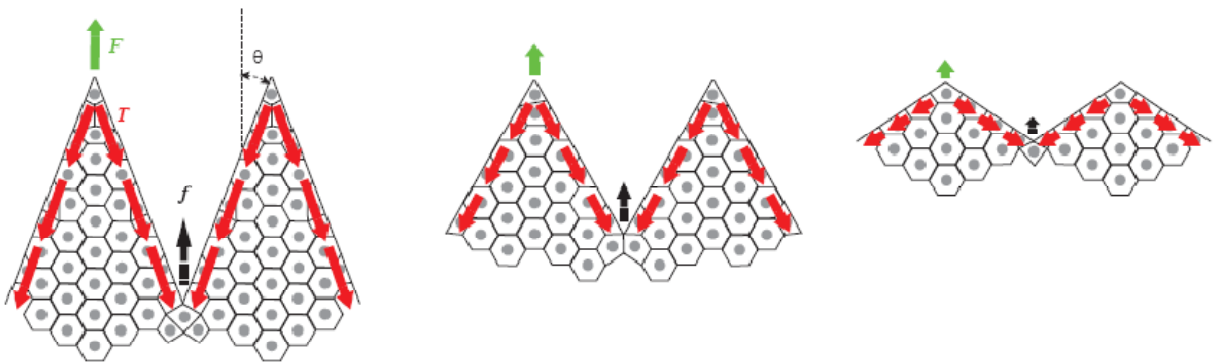


Figure 5.1 Schematic of wound closure in zigzag wounds and the effect of angles on purse string contraction. Cells at the apex develop into leader cells and create traction forces (F , green arrows) that are transmitted through the neighboring actomyosin cables (red arrows). The increased tension, T strengthens the contraction forces (f , black arrows) in the actomyosin purse string, drawing the cell sheet forward. The propensity for leader cell formation increases with decreasing angle θ at the apex, and contraction forces are expected to increase with decreasing angle.

5.2 Materials and methods

Cell culture

Madin-Darby Canine Kidney (MDCK) cells were cultured in Dulbecco's modified eagle medium (DMEM) containing 10% fetal bovine serum, 1% penicillin/streptomycin, and phenol-red (growth medium). All experiments were performed in DMEM lacking phenol-red, supplemented with 1% penicillin/streptomycin (serum-free medium).

Wound healing with micropatterned PDMS blocks

The micropatterned PDMS blocks were fabricated as described in Chapter 4. The wound features were designed using DesignCAD software and printed on transparencies as positive photomasks (CAD/Art Services, Inc., Bandon, OR) as shown in Figure 5.2A. Similarly, the wound healing assay used in this work was described in Chapter 4 (Figure 5.2A).

Fluorescence imaging

The MDCK cell monolayers were wounded and maintained in serum-free media at 37 °C for 4 h. Cells were fixed with pre-warmed 3.7% paraformaldehyde in PBS at pH 7.5 for 20 min at 37 °C. After washing with PBS, cells were blocked in blocking solution (10% FCS, 5% sucrose, 2% BSA in PBS) for 30 min at room temperature. To visualize actin, cells were incubated with phalloidin-rhodamine (1:50 in PBS, Molecular Probes, Inc., Eugene, OR) for 1 h 37 °C. Glass coverslips were mounted with 1:1 glycerol in PBS

and imaged using an Zeiss Axiovert 200 M microscope with epifluorescence optics and AxioVision LE software.

Data analysis

The wound areas demarcated by the red box (Figure 5.3B) were traced manually using ImageJ v1.42 (NIH). The displacement of the cell sheet in the direction of the wound was calculated by dividing the change in the wound area by the length of the wound (l) at various time points. The point on the wound edge furthest from the apex was followed for 24 h using MTrackJ, an ImageJ plugin developed by Meijering and coworkers at the Biomedical Imaging Group Rotterdam. The displacement was averaged for all videos and plotted as a function of time for each angle. The data was fitted to a linear fit and the slopes resulting from the fit were reported as contractile speeds ($\mu\text{m/h}$).

Statistical Analysis

For all experimental data, the statistical significance of differences was estimated by analysis of variance followed by the Tukey test. Differences were taken to be significant at $P \leq 0.05$.

5.3 Results and discussion

As expected, the zigzag wound geometry promoted both leader cells and actomyosin purse strings at the apex and concave regions, respectively. After 4 h, cells developed lamellipodia in convex regions (indicated by position b in Figure 5.2A), which were similar to “finger-like” leader cell protrusions (3). As expected, the purse string mechanism was dominant in concave regions of the wound edge (position c in Figure 5.2A). Images of the wound edge labeled with F-actin confirmed the presence of lamellipodia and actomyosin purse string cables in these regions (Figures 5.2B and C).

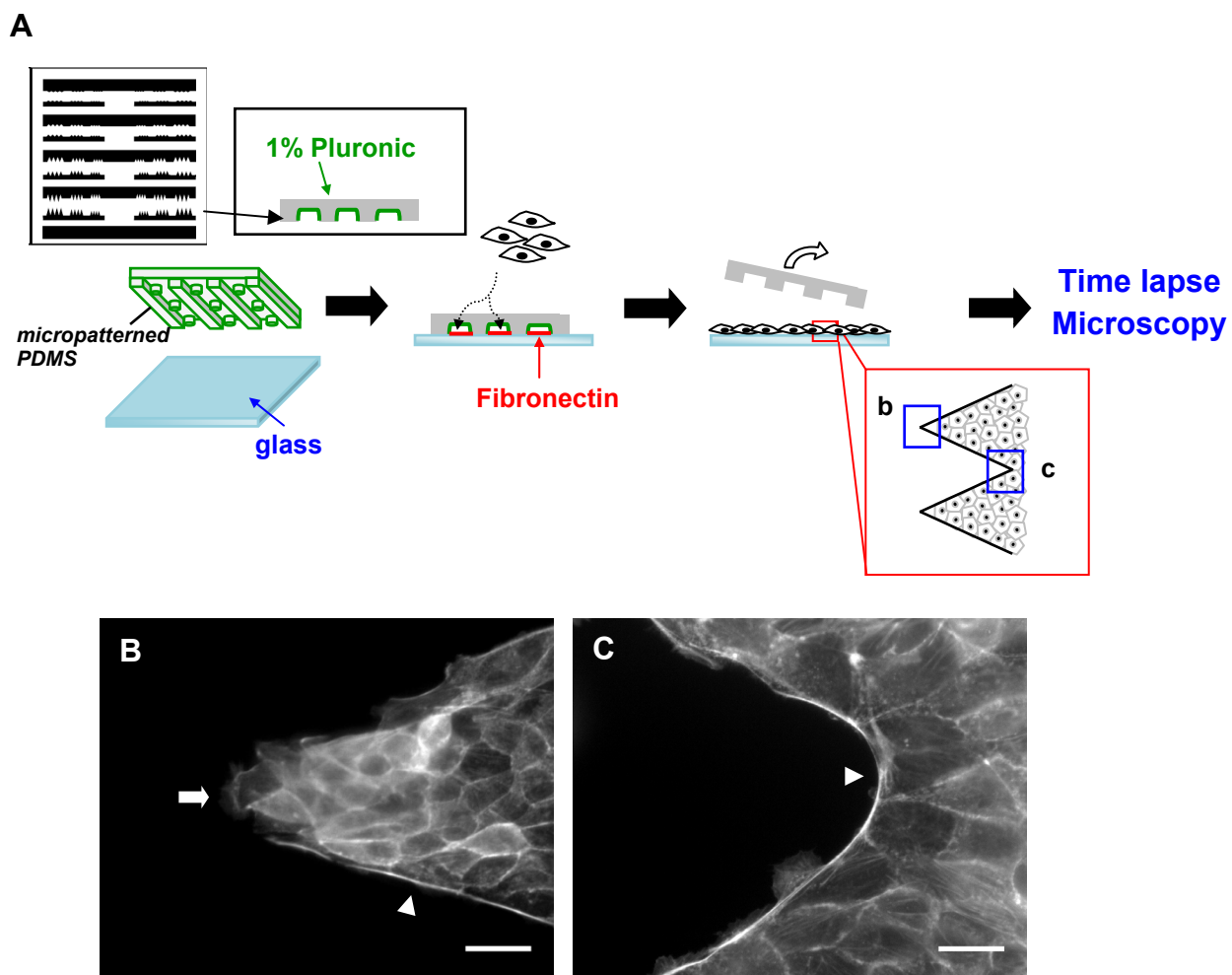


Figure 5.2 Initial wound geometry determines mode of wound healing. (A) Schematic of wound healing assay. The PDMS micropatterns were released and MDCK cell monolayers were allowed to migrate on glass surfaces for 4 h in serum-free media. Cells were fixed and stained with phalloidin-rhodamine. (B, C) Fluorescence images show the formation of leader cells (white arrow) and purse string structures (white triangles) after 4 h, corresponding to positions b and c as shown in A. Scale bars represent 20 μm .

Figure 5.3A shows time-lapse images of zigzag wounds for varying angles 2θ . For all zigzag wounds with $2\theta = 45^\circ$, cells in the convex regions extended their lamellipodia, but did not migrate into the wound area. Instead, cells often rearranged themselves at the corners while preserving the “finger-like” patterns. In the concave regions of the cell sheet, purse strings contracted in the direction of the wound, propelling the cell sheet forward. At later times (> 20 h), the finger-like patterns also became motile. Wounds with $2\theta = 45^\circ$ are most likely to promote the formation of leader cells.

Similar behavior was also observed in zigzag wounds with larger angles. Although cells at the apex extend lamellipodia, these finger-like features were quickly re-integrated into the cell sheet. Nonetheless, purse string contractions were also observed in the concave regions, giving rise to net movement in the direction of the wound. In comparison, minimal migration was observed on the straight-edged wounds (i.e., $2\theta = 180^\circ$).

To quantify the wound closure rates, we manually tracked the change in the wound area over time (Figure 5.3B). We represented the displacement of the cell sheet by dividing the change in the wound area by the length of the cell sheet, l (Figure 5.3C). The wound closure rates were obtained by fitting the data from time interval $t = 12$ h to 22 h to a linear fit (Table 5.1).

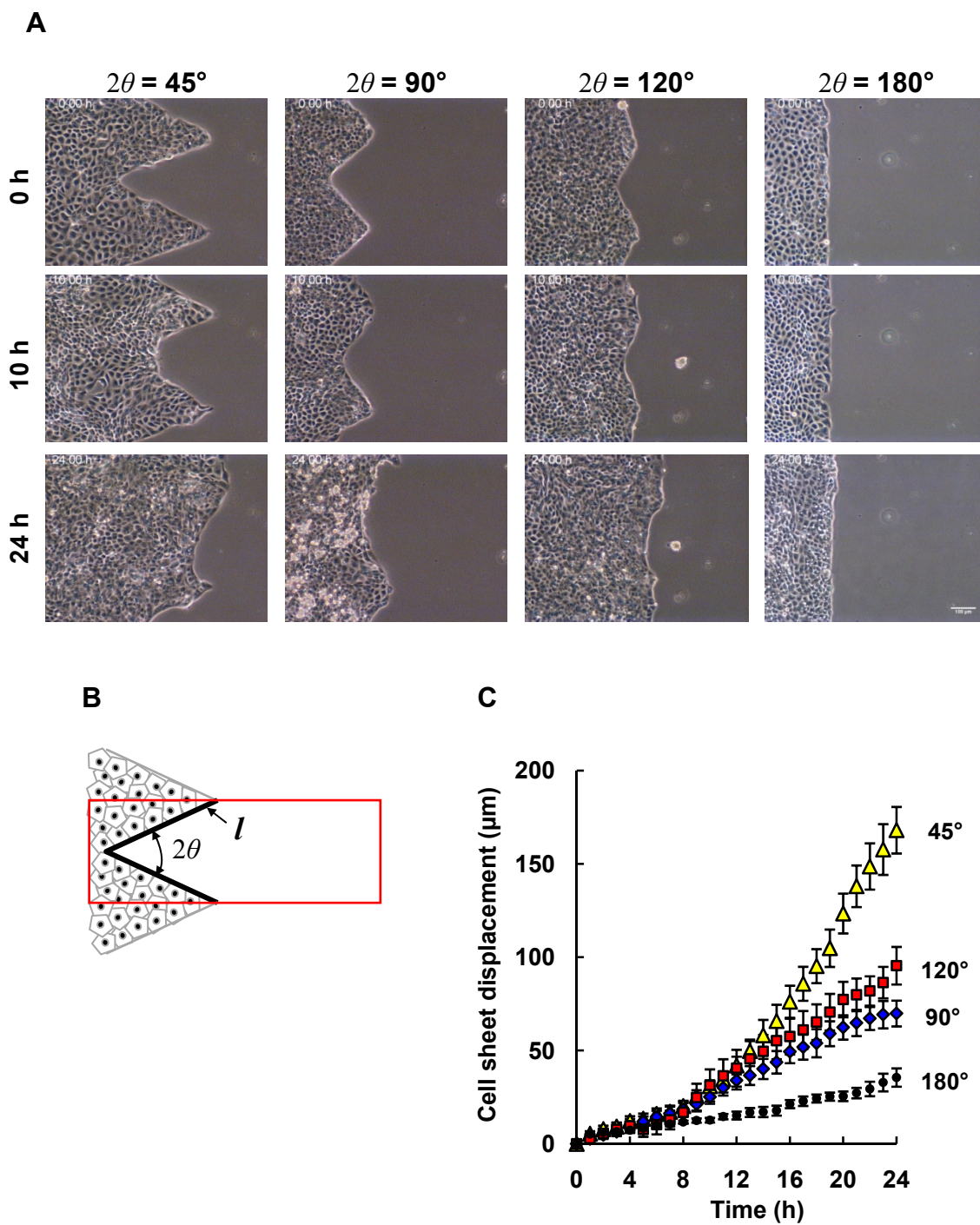


Figure 5.3 Time course of wound healing for zigzag wounds. (A) Time-lapse images of various zigzag wounds with angles 2θ . Scale bar represents $100\ \mu\text{m}$ for all images. (B) Schematic of the wound closure analysis. The length of the wound (l) is highlighted in black. (C) The displacement of the cell sheet over time. Cell sheet displacement for each time point was

calculated by measuring the change in wound area within the red box and divided by the length of the wound (l). Data are means \pm SEM for at least 10 independent experiments.

| 2θ | Wound closure rate \pm S.E. ($\mu\text{m/h}$) |
|-----------|--|
| | $t = 12$ to 22 h |
| 45 | 10.7 ± 0.5 |
| 90 | 3.5 ± 0.1 |
| 120 | 4.2 ± 0.1 |
| 180 | 1.4 ± 0.1 |

Table 5.1 Wound closure rates as a function of 2θ . The data in Figure 5.3C were subjected to linear fits for time intervals $t = 12$ to 22 h. The slopes obtained from the fit are reported as wound closure rates \pm S.E.

The overall wound closure rates for zigzag wounds with $2\theta = 45^\circ$ was 7.6-fold higher than for a straight-edged wound ($2\theta = 180^\circ$) (Table 5.1). These wounds promoted rapid contraction of the wound edge via the actomyosin purse string with speeds up to $20 \mu\text{m/h}$ (Figure 5.4). In comparison, contractile speeds for purse strings resulting from zigzag wounds with larger angles were two-fold lower (Figure 5.4).

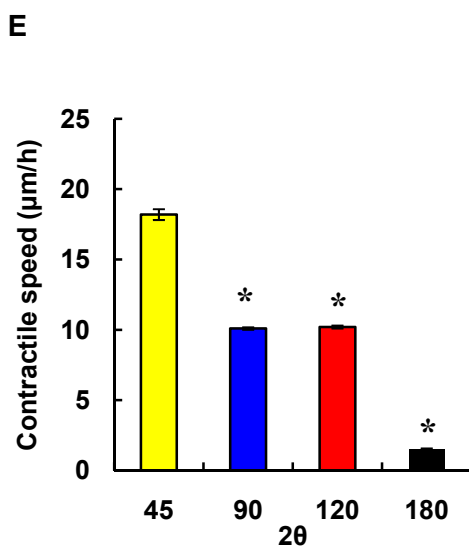
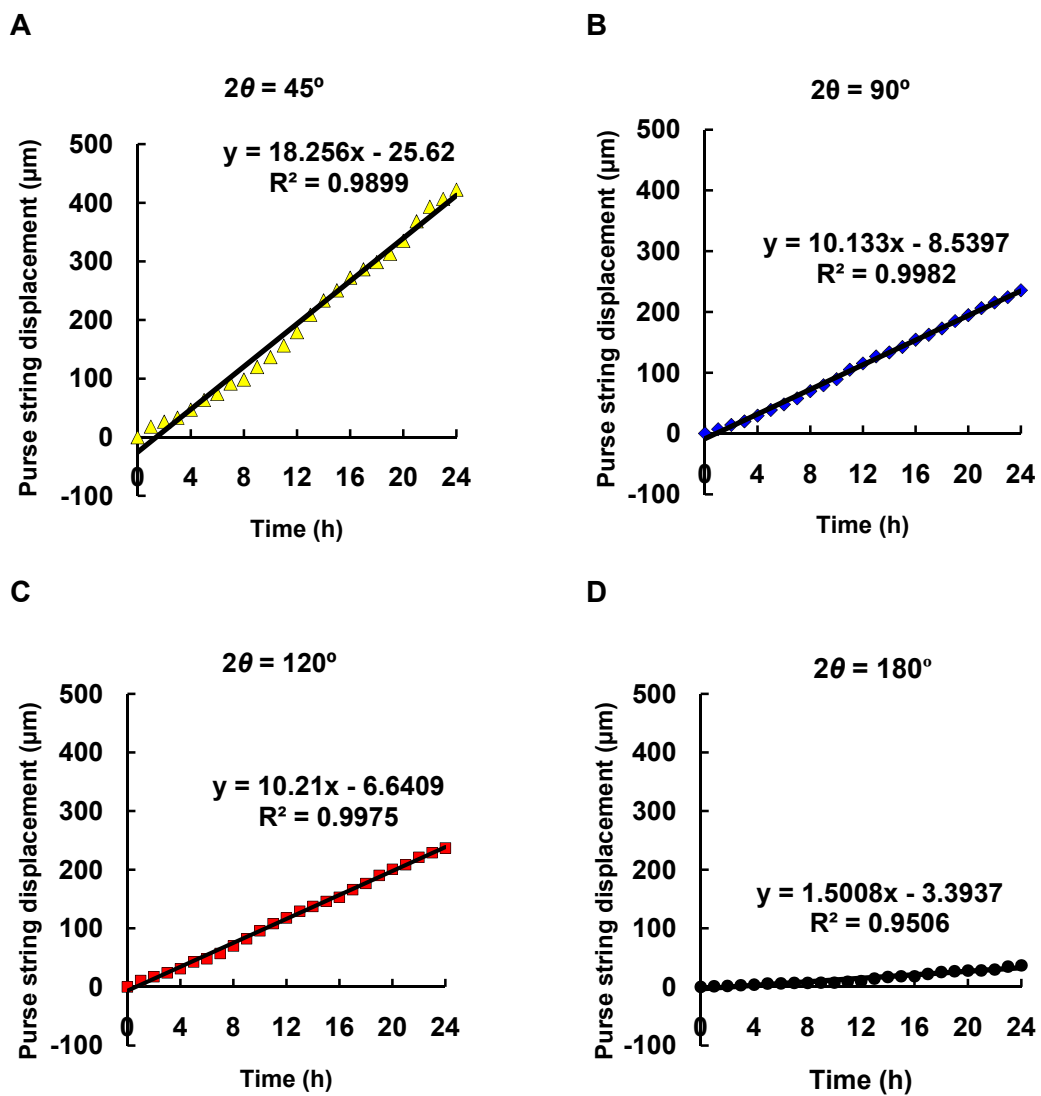


Figure 5.4 Overall contractile speed of purse string as a function of 2θ . The point on the wound edge furthest away from the apex was tracked manually for 24 h and the displacement of the purse string was measured over time. (A to D) Average purse string displacement over time of all the videos analyzed. (E) Contractile speed of purse string for zigzag wounds of with angles 2θ . Data are slopes from fitted data shown in A to D. Error bars are standard errors calculated from the fit. *, significant difference from $2\theta = 45^\circ$.

5.4 Conclusions

In summary, we demonstrate the synergistic use of both wound healing modes to accelerate wound closure. We also demonstrate that cells at the wound edge can be made to adopt specific wound healing mechanisms based on the local geometry. By patterning wound geometry in a zigzag shape, we show that cells at the apex develop into leader cells and cells at concave regions activate the actomyosin purse string. Under these conditions, leader cells generate traction forces that are transmitted through the actomyosin purse strings. The increased tension results in higher contractile forces, pulling the cell sheet forward. As a result of the strengthened purse string contraction, wound closure rates were increased nearly eight-fold in zigzag wounds with the smallest angles (i.e. $2\theta = 45^\circ$), compared to wounds with straight edges.

5.5 Acknowledgements

I thank Dr. Ouyang Mingxing for help with producing the CAD drawing for the micropatterns and Elowitz lab for the MDCK cells. This work is funded by the NIH.

5.6 References

1. P. Martin, J. Lewis, *Nat. Lett.* **360**, 179 (1992).
2. G. Fenteany, P. A. Janmey, T. P. Stossel, *Curr. Biol.* **10**, 831 (2000).
3. T. Omelchenko, J. M. Vasiliev, I. M. Gelfand, H. H. Feder, E. M. Bonder, *Proc. Natl. Acad. Sci. USA* **100**, 10788 (2003).
4. W. M. Bement, P. Forscher, M. S. Mooseker, *J. Cell Biol.* **121**, 565 (1993).
5. D. P. Kiehart, *Curr. Biol.* **9**, R602 (1999).
6. M. Tamada, T. D. Perez, W. J. Nelson, M. P. Sheetz, *J. Cell Biol.* **176**, 27 (2007).
7. Y. Danjo, I. K. Gipson, *J. Cell Sci.* **111**, 3323 (1998).
8. O. M. Rossier et al., *EMBO J.* **29**, 1055 (2010).
9. S. P. Palecek, J. C. Loftus, M. H. Ginsberg, D. A. Lauffenburger, *Nature* **385**, 537 (1997).
10. C. M. Lo, H. B. Wang, M. Dembo, Y-L. Wang, *Biophys. J.* **79**, 144 (2000).
11. X. Jiang, D. A. Bruzewicz., A. P. Wong, M. Piel, G. M. Whitesides, *Proc. Natl. Acad. Sci. USA* **102**, 975 (2005).
12. S. Grasso, J. A. Hernandez, S. Chifflet, *Am. J. Physiol. Cell Physiol.* **293**, C1327 (2007).
13. K. K. Parker et al., *FASEB J.* **16**, 1195 (2002).

6 CONCLUSIONS AND FUTURE WORK

Protein-based biomaterials have gained considerable attention in recent years as potential candidates in various biomedical applications (1). Artificial proteins can be designed to present the appropriate biological and mechanical cues for directing cell behavior. For tissue repair, biomaterials are required to promote rapid cell migration and proliferation of cell sheets. In this thesis, we attempted to design artificial extracellular matrix (aECM) proteins for accelerating wound healing by incorporating relevant biological and mechanical functionalities.

We have demonstrated that human corneal epithelial cells attach and spread preferentially to aECM protein containing the RGD cell-binding domain. These surfaces also promote wound healing, in a fashion dependent on the RGD density. However, the rate of healing of epithelial cell monolayers was surprisingly not determined by the rate of cell migration. Instead, we found that the overall wound closure rates were dictated by the boundary-crossing rates; a result verified by simulation and experimental data.

In previous work from our laboratory (2-3) and others (4), cell responses on RGD surfaces were never identical to that of fibronectin. To improve the activity of aECM proteins, full length cell-binding domains were incorporated. We showed that Rat-1 fibroblasts attach and spread two fold faster on the aECM protein containing full-length fibronectin domains 9 and 10, compared to the short RGD variant. These proteins also supported rapid cell migration and proliferation, resulting in wound closure rates comparable to those observed on fibronectin. aECM proteins containing full-length fibronectin domains also promoted phosphorylation of focal adhesion kinase (FAK) and extracellular signal-regulated kinase (ERK), accounting for the higher cell migration speeds and proliferation rates on these proteins.

Following this work, we used the aECM protein containing the fibronectin domain 10 to investigate how cells select the wound healing mechanism along the periphery of the wound. To create wounds with precise geometry, we used microfabrication to prepare micropatterned PDMS blocks to be used as barriers in the wound healing assay. MDCK wound healing on aECM surfaces exhibited unique patterns: leader cell groups are separated by constant regions of actomyosin purse string. The average spacing between consecutive leader cell groups was independent of wound size. However, this spacing was found to decrease with increasing myosin inhibition. These observations could be explained by a simple phenomenological model of force transmission. We also verified by experiments that the selection of wound mechanism along the wound edge could be controlled by wound geometry. These results were consistent with the model predictions.

Wound geometry could also be used to influence wound healing behavior of cell sheets. Using zigzag wounds, we created configurations where both lamellipodial crawling and actomyosin purse string act synergistically to accelerate the wound. In these zigzag-shaped wounds, cells located at the apex of zigzag wounds have a high propensity to develop into leader cells. At the same time, cells in concave regions are likely to undergo actomyosin contraction. Using a similar force transmission mechanism described in Chapter 4, we hypothesized that zigzag wounds with smaller angles at the apex have larger probability to develop into leader cells, and hence generate larger purse string contractions. Indeed, we observed especially strong purse string contraction in zigzag wounds with the smallest angle at the apex (i.e., $2\theta = 45^\circ$) and these wounds healed nearly eight fold faster compared to wounds with straight edges.

Genetic engineering has demonstrated tremendous potential for creating protein-based materials for use in the body. Artificial proteins with novel mechanical and biological properties

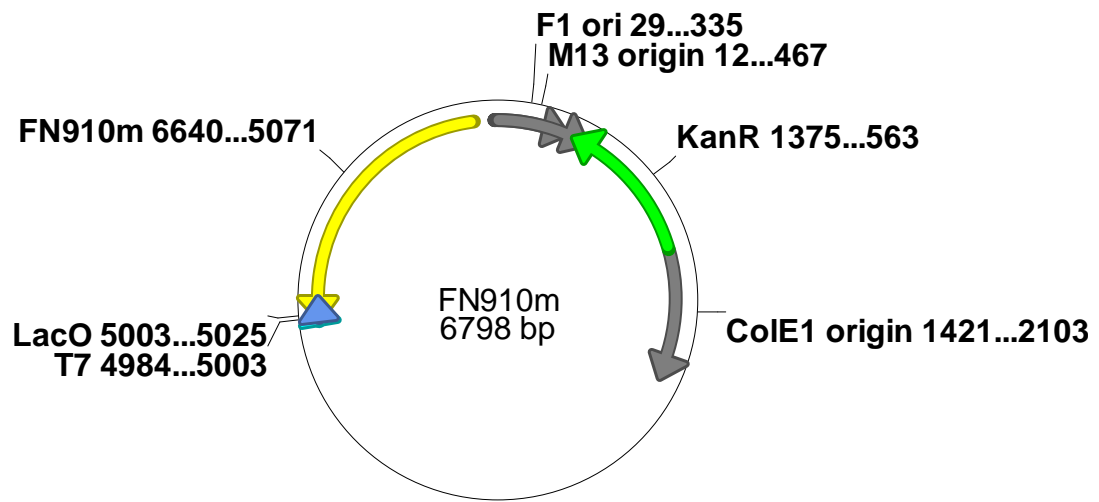
could be fabricated to create complex 2D and 3D environments for directing cell sheet migration in tissue repair. For instance, the biological domains could also be expanded to include sequences from other types of ECM molecules or full length functional growth factors (5-6). Similarly, domains derived from other structural proteins such as silk (7) could be used to create materials with dramatically different mechanical properties. Since chemical and mechanical properties could also be controlled separately, artificial proteins provide a convenient system to decouple and study the effects of physical and chemical signals in collective migration. The wound healing studies could also be expanded to examine wound healing in 3D matrices, which are physiologically relevant to implantable biomaterial applications (8).

References

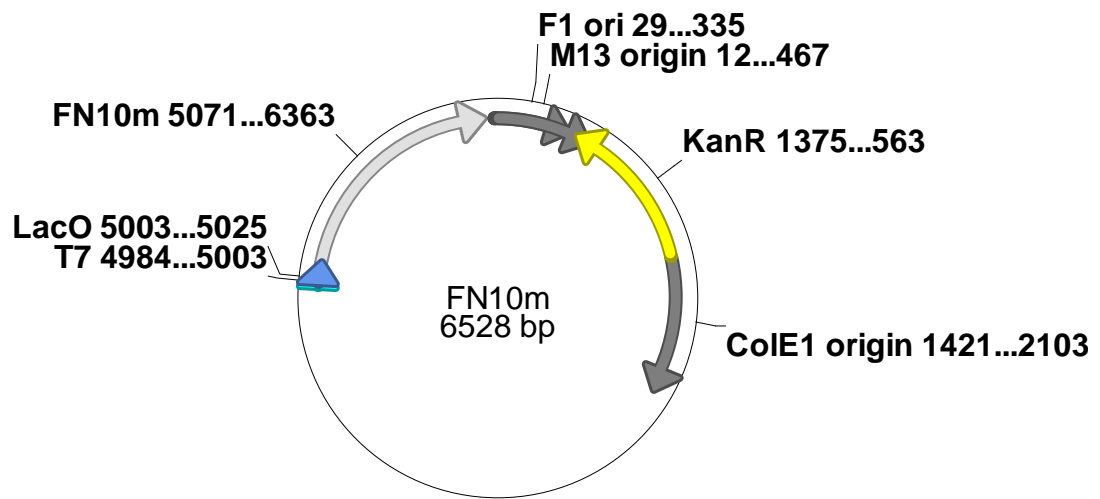
1. S. A. Maskarinec, D. A. Tirrell, *Curr. Opin. Biotechnol.* **16**, 422 (2005).
2. J. C. Liu, S. C. Heilshorn, D. A. Tirrell, *Biomacromolecules* **5**, 497 (2003).
3. J. C. Liu, D. A. Tirrell, *Biomacromolecules* **9**, 2984 (2008).
4. H. B. Streeter, D. A. Rees, *J. Cell Biol* **105**, 507 (1987).
5. J. A. Hubbell, *Swiss Med. Wkly* **136**, 387 (2006).
6. D. J. Geer, D. D. Swartz, S. T. Andreadis, *Am. J. Pathol.* **167**, 1575 (2005).
7. G. H. Altman et al., *Biomaterials* **24**, 401 (2003).
8. K. Y. Lee, D. J. Mooney, *Chem. Rev.* **101**, 1869 (2001).

PLASMID MAPS

Plasmid map for aECM protein (FN910m):



Plasmid map for aECM protein (FN10m):



Plasmid map for aECM protein (RGDm):

